Bulletin of the Seismological Society of America
October 2018, Volume 108, Issue 5A, Pages 2650-2674
http://dx.doi.org/10.1785/0120170258
http://archimer.ifremer.fr/doc/00453/56416/

An Alternative View of the Microseismicity along the Western Main Marmara Fault

Batsi Evangelia [1, *], Lomax Anthony [2], Tary Jean-Baptiste [3], Klingelhoefer Frauke [1], Riboulot Vincent [1], Murphy Shane [1], Monna Stephen [4], Meral Ozel Nurcan [5], Kalafat Dogan [5], Saritas Hakan [6], Cifci Gunay [6], Cagatay Namik [7], Gasperini Luca [8], Geli Louis [1]

[1] Institut français de recherche pour l'exploitation de la mer (Ifremer), Laboratoire Aléas géologiques et Dynamique sédimentaire - LAD Marine Geosciences Research Unit, CS 70 20280 Plouzané, France
[2] ALomax Scientific ,320 Chemin des Indes 06370 Mouans Sartoux ,France
[3] Departamento de Geociencias Universidad de los Andes Carrera 1ª No 18-A-10 -Edificio M1 Tercer Piso Bogotá, Colombia
[4] Istituto Nazionale di Geofisica e Vulcanologia (INGV) Via di Vigna Murata, 605 Unit RU Integrated Systems for Marine Environmental Infrastructures 00143 Rome, Italy
[5] Boðaziçi University Kandilli Observatory and Earthquake Research Institute (KOERI) 34684 Cengelkoy Istanbul, Turkey
[6] Dokuz Eylül University (DEU) Cumhuriyet Bulvarý No. 144 35210 Alsancak Ýzmir, Turkey
[7] Faculty of Mines Department of Geology Istanbul Technical University (ITU) 34469 Maslak Istanbul, Turkey
[8] Institute of Marine Science National Research Council (ISMAR-CNR) Via Gobetti 101 40129 Bologna, Italy

* Corresponding author : Evangelia Batsi, email address : Evangelia.Batsi@ifremer.fr

Abstract :

A detailed study, based on ocean-bottom seismometers (OBSs) recordings from two recording periods (3.5 months in 2011 and 2 months in 2014) and on a high-resolution, 3D velocity model, is presented here, which provides an alternative view of the microseismicity along the submerged section of the North Anatolian fault (NAF) within the western Sea of Marmara (SoM). The nonlinear probabilistic software packages of NonLinLoc and NLDiffLoc were used for locating earthquakes. Only earthquakes that comply with the following location criteria (e.g., representing 20% of the total amount of events) were considered for analysis: (1) number of stations≥5; (2) number of phases≥6, including both P and S; (3) root mean square (rms) location error≤0.5 s; and (4) azimuthal gap≤180°. P and S travel times suggest that there are strong velocity anomalies along the Western High, with low Vp, low Vs, and ultra-high Vp/Vs in areas where mud volcanoes and gas-prone sediment layers are known to be present. The location results indicate that not all earthquakes occurred as strike-slip events at crustal depths (>8 km) along the axis of the Main Marmara fault (MMF). In contrast, the following features were observed: (1) a significant number of earthquakes occurred off-axis (e.g., 24%), with predominantly normal focal mechanisms, at depths between 2 and 6 km, along tectonically active, structural trends oriented east–west or southwest–northeast, and (2) a great number of earthquakes was also found to occur within the upper sediment layers (at depths<2 km), particularly in the areas where free gas is suspected to exist, based on high-resolution 3D seismics (e.g., 28%). Part of this ultra-shallow seismicity appears to occur

in response to deep earthquakes of intermediate (ML∼4–5) magnitude. Resolving the depth of the shallow seismicity requires adequate experimental design ensuring source–receiver distances of the same order as hypocentral depths. To reach this objective, deep-seafloor observatories with a sufficient number of geophone sensors near the fault trace are needed.

Introduction

The study and understanding of seismicity for large and devastating earthquakes as well as for background micro-seismicity is of fundamental importance for earthquake hazard assessment. Hence, considerable effort is spent world-wide for characterizing active faults through enhanced seismic monitoring. In submarine environments, however, the presence of the water column makes monitoring particularly complicated and difficult. Because deep-sea environments are remote, hostile and corrosive, there are to date only a few permanent deep sea-floor observatory networks funded at the national or international level, e.g., offshore Japan (DONET for Dense Oceanfloor Network system for Earthquakes and Tsunamis), Canada (NEPTUNE), USA (MARS) and at some sites of Europe (EMSO, for European Multidisciplinary Seafloor and water-column Observatory). Due to their elevated maintenance costs, offshore facilities require more detailed and more specific justification than onshore facilities. The case of the submerged section of the North Anatolian Fault (NAF), within the Sea of Marmara (SoM), is a strong motivator in that respect. In a recent review paper, (Aktar, 2017) underlines that the uncertainty for earthquake locations along the western part of the SOM, is higher in the vertical direction but this could be improved considerably by the application of double difference method using land-based seismological data, including data from seismometers installed in near-shore boreholes or from arrays installed on islets. The question of the value added by offshore data from seismometers installed on the sea bottom near the fault trace is addressed here.

The highly active, right lateral strike-slip NAF has produced devastating historical earthquakes along its 1600 km long trace (e.g., Ambraseys and Finkel, 1995). In 1912, the fault was ruptured by the Ganos earthquake, which ended at the Western extremity of SoM (e.g., Ambraseys and Finkel, 1987). To the east of SoM, the spatial progression of earthquakes along this fault system has a more or less westward progression since 1940, with a sixty year sequence of rupturing towards Istanbul (e.g., Stein *et al.*, 1997). The last destructive earthquake occurred at the eastern end of the SoM (1999 Izmit and Duzce earthquakes) and therefore the next large (Mw > 7) earthquake is now expected to nucleate beneath the SoM, putting at risk the 15 million inhabitants of the Istanbul megacity (e.g., Pondard *et al.*, 2007; Parsons *et al.*, 2004).

As a result, the SoM (see Figure 1a) was extensively surveyed since 1999, allowing a wealth of geological, geophysical and geochemical data to be collected. The Main Marmara Fault (MMF) system was identified as a major target for the implementation of seafloor observatories, and important preparatory work was done to address this long term challenge. In 2009 and 2010, five cabled sea-bottom seismometers were deployed on the Marmara seafloor by Kandilli Observatory and Earthquake Research Institute (KOERI), which collected broadband data until 2013. Site surveys and autonomous instrument deployments were conducted within European Union funded projects, respectively the ESONET/MARMARA-DM Project (2008-2011, e.g., (Géli, *et al.*, 2011) and the MARSITE Project (2012-2016). Here, we present a high-resolution seismological study of the Western SoM, based on all the geological knowledge acquired since 1999 and on the Ocean Bottom Seismometer (OBS) data collected within the latter two projects, in 2011 and 2014 respectively (see Figure 1b).

This work complements a previous study by (Géli *et al.*, 2018), of only a part of the 2011 dataset, that showed the existence of shallow, gas-related seismicity, based on the combination of seismological and geochemical arguments. Because there was no station at the center of the OBS network during the last month of the 2011 experiment, a new deployment was carried out in 2014, with a denser network closer to the fault (see Figure 1b). The results obtained with a high resolution 3D velocity model provide new insights on the nature of the micro-seismicity and on the behavior of the western segments of the MMF.

Geological background: specificities to take into account for precise earthquake location

According to (Şengör *et al.,* 2005), the NAF was formed by a progressive strain localization, mostly along an interface juxtaposing subduction-accretion material to its south and older and stiffer continental basement rocks to its north. The shear-related, post-Miocene deformation produced four separate basins within the Marmara shear zone, filled with Plio-Quaternary sediment sequences, respectively from west to east: the Tekirdag Basin, the Central Basin, the Kumburgaz Basin and the Cinarçik Basin (see Figure 1a). After the numerous bathymetric and seismic surveys that were conducted since 1999 (e.g., Le Pichon *et al.,* 2001; Imren *et al.,* 2001; Armijo *et al.,* 2002; Rangin *et al.,* 2004; Carton *et al.*, 2007; Shillington *et al.*, 2012), the currently active fault traces are now well known. So are the main trends of the basins and crustal structure, based on deep seismic soundings (e.g., Laigle *et al.*, 2008; Bécel *et al.*, 2006; Bayrakci *et al.*, 2013). From these surveys, it is clear that: i) the geological structure along the MMF is essentially 3D from the surface to the deep crust, both along and across the strike of the fault, and ii) the central part of the Marmara Trough is filled with “soft” Plio-Quaternary sediment sequences, more than 5 km thick. These features are key elements to take into account when deriving appropriate velocity models for high-resolution earthquake location near the fault zone.

Another aspect that should be considered is the existence of widespread gas emissions from the Marmara seafloor (e.g., Kuscu *et al.*, 2005; Géli *et al.*, 2008; Dupré *et al.*, 2015) and the realization that the NAF beneath the SoM cuts across hydrocarbon gas prone sediment layers (e.g., Bourry *et al.*, 2009). As stated in (Dupré *et al.*, 2015), the distribution of gas emissions in the SoM appears to be controlled by a number of factors, e.g.: the fault and fracture networks; the nature and thickness of sediments; the connectivity between the seafloor and the gas sources; and the microseismicity. Hence, the role of gas must be identified and discriminated from the tectonics. To reach this goal, it is necessary to improve the depth determination of shallow seismicity using nearby monitoring stations and detailed velocity models, that take into account the upper sedimentary layers.

3D velocity-structure of the Western Sea of Marmara

Given the considerations above, specific 3D velocity models are required to account for: i) the sharp seafloor topography; ii) the slow P-wave velocity of Plio-Quaternary sediments; and iii) the differences in the deep crustal structure between the northern and southern parts of the NAF. Published 3D-models do exist with grid spacing of 9 x 9 km and 10 × 10 km for the Marmara Region (e.g., Gürbüz *et al.*, 2013 and Yamamoto *et al.*, 2017), respectively and grid spacing of 6 × 6 km for the Marmara offshore domain (e.g., Bayrakci *et al.*, 2013). The horizontal grid-spacing (9, 10 and 6 km, respectively) of these models is too large, however, to account for both the velocity contrast at the seafloor interface and the sharp geometry of the basins, as well as the expected heterogeneties of the velocity structure across the strike of the MMF. Hence, here we rather use the high-resolution, 3D-velocity model (with a grid node spacing of 750 m × 750 m × 200 m) that was specifically tailored by the French Research Institute for Exploitation of the Sea (Ifremer, Institut français de recherche pour l' exploitation de la mer) for the 20 km × 60 km area covered by the submarine networks deployed in 2011 and 2014 in the Western SoM (see Figure 2a) and details reported in (Cros and Géli, 2013) and in (Gürbüz *et al.*, 2013). This model is based on all available geological and geophysical data from the SoM, including: i) the high-resolution (38 m) bathymetric grid from (Le Pichon *et al.*, 2001); ii) the 3D, P-wave velocity grid derived from seismic tomography by (Bayrakci *et al.*, 2013), with the S-wave velocity model being the P-wave model divided by the V_p/V_s ratio; iii) the deep crustal velocities inferred from wide-angle, 2D seismics by (Bécel, *et al.*, 2009) and iv) the fault mapping and basin geometry line-drawing, based on the interpretation of all existing seismic profiles (e.g., Şengör *et al.*, 2005; Şengör *et al.*, 2014).

Data

The two following seismological datasets were analyzed (see details in Tables 1 and 2 and Figure 1b):

- Dataset-1 was recorded from 15th of April to 31st of July, 2011, by 10 autonomous, 3 component (1 vertical and 2 non-oriented horizontal) short-period (4.5 Hz) OBSs from Ifremer and by 2 permanent, cabled broad-band, 3 components OBSs operated by KOERI. Unfortunately, the central station of the network, OBS2, stopped recording on July 1st, 2011.
- Dataset-2 was recorded from 19th of September to 14th of November, 2014, by 9 autonomous, 3 component (1 vertical, 2 non-oriented horizontal) short-period (4.5 Hz) OBSs from Ifremer and by 1 autonomous, broad-band OBS operated by the Istituto Nazionale Geofisica e Vulcanologia (INGV) (e.g. OBS13). Note that two autonomous, short-period OBS were also deployed by Ifremer, from the 1st until the 15th of November near gas emissions sites (e.g. close to the central station OBS4). The

recording period of 2014 of Ifremer's and INGV's OBSs overlaps with the recording period of the Japan Agency for Marine Earth Science and Technology (Jamstec) OBSs that were independently deployed by (Yamamoto *et al*., 2017) for a duration of 10 months, from September 2014 to June 2015, in the Western part of the SoM, from the Tekirdag Basin to the Central Basin.

- Additional geological and geophysical data sets were used to guide our analysis:
  - high-resolution 3D- and 2D-seismic data collected in 2009 with R/V Le Suroit and with R/V Piri Reis, respectively. The full description of the 3D-acquistion system and dataset is detailed in (Thomas *et al.,* 2012).
  - multi-channel, deep seismic lines collected in 2001 during the Seismara Cruise of R/V Le Nadir (e.g., Laigle *et al.*, 2008; Bécel *et al.*, 2009; Bécel *et al.*, 2010).
  - an unpublished bathymetric grid of the Central Basin and Western High, having a node spacing of 10 meters, based on multibeam echosounder system data collected in 2014 with *R/V Pourquoi Pas?* (see Data and Resources section). This 10 m grid (courtesy of Charline Guérin of Ifremer) is available on request to the authors.

Tools and Methodology

Location procedure

For both OBS datasets of 2011 and 2014 recording periods, the same methodological approach was used, based on the non-linear methods developed by (Lomax, 2014). The 3D-location process (fully described in (Lomax, 2014)) includes the 5 following steps (e.g., see Data and Resources section):

1) **Picking**: The picking was performed using respectively the FilterPicker routine (e.g., Lomax *et al.*, 2012) for the OBS dataset of 2014, and the Sytmis software package for the OBS dataset of 2011 (see Data and Resources Section). The 3 components of the geophone were used for this analysis. Specifically the vertical component was used for the detection of P-wave arrivals while the two non-oriented horizontal components were used for the S-wave onsets (e.g. strong velocity contrasts in areas with shallow sediments could generate converted phases, hence their identification on vertical channels could be misleading). All picks were visually checked. Uncertain picks were systematically removed. Manual corrections -when needed- were applied to the remaining picks.

2) **Phase association**: the Early-est routine of the Lomax Package was run to perform phase association and to determine the initial earthquake locations for step 3, using the 1D (V_p and V_s) model described in (Cros and Géli, 2013) (see also (Lomax, 2014) and Data and Resources section). In this initial phase, a non-constant V_p/V_s

ratio was used in the 1D velocity model.

3) **Initial 3D absolute locations**: NonLinLoc software was applied without station corrections using our high resolution, 3D P-velocity model (with a constant V_p/V_s ratio equal to 1.78), to compute a preliminary set of absolute locations and station corrections.

4) **Station corrections and final 3D absolute locations**: The accuracy of travel-time picks was successfully improved by applying station corrections for both P and S travel time grids by using their average phase residuals obtained from a run of NonLinLoc (see Tables of station corrections in Supplementary Information). The objective was to account for: (i) the near-surface deviations of seismic velocities from the applied model (e.g., Hausmann *et al.,* 2010), since all models (including 3D) do not take into account the real velocity variations (e.g. shallow, near-station, smaller scale and potentially low velocity structure cannot or are not modeled), (ii) algorithm instabilities, (iii) picking phases errors, etc. NonLinLoc was applied using the 3D, P-velocity model (with V_p/V_s=1.78), along with the station corrections and the absolute locations of all the detected earthquakes resulting from step 3, to compute the final absolute locations after 3 iterations. As described in (Lomax *et al.,* 2008), this procedure is expected to produce a tighter cluster of events relative to the large scatter of events of the initial absolute locations (e.g. see step 3).

5) **Relative locations**: NLDiffLoc was eventually run to compute the relative locations based on the final absolute locations. NLDiffLoc performs a differential earthquake location based on the double difference equation from (Waldhauser and Ellsworth,

2000). The double difference code is using as input the files of: (i) initial absolute locations (e.g. derived from NLLoc; see step 4) and (ii) differential travel times (e.g. derived from Loc2ddct tool) which are calculated for a specified maximum distance between event couples. The relative coordinates (e.g. x, y, z and t) are optimized for a set of hypocenters given a set of differential phase arrival time measures at each station for multiple hypocenters. This is achieved by using a non-linearized global search (e.g. a Metropolis random walk, (Lomax *et al.*, 2009)), which maximizes the probabilistic solution likelihood as the hypocenter coordinates are perturbed. A double-difference equation from (Waldhauser and Ellsworth, 2000) is then evaluated for determining the misfit and the solution likelihood by using an L1 norm which is more robust with outlier data (e.g. in contrast to L2 norm which is equivalent to what HypoDD is using).

For both final absolute and relative locations (e.g. steps 4 and 5) the following criteria were used for “well constrained events”: (i) Number of stations ≥ 5, (ii) RMS ≤ 0.5 s, (iii) azimuthal gap ≤ 180°, and (iv) number of phases ≥ 6 including both P and S phases. Consequently, only a small percentage (20 %) of the recorded seismicity was considered (e.g. 191 and 78 relocated earthquakes for the 2011 and 2014 recording periods, respectively).

Multiplet analysis

The GISMO collection of Matlab tool boxes for seismic waveform analysis, (see Data and Resources section) was used for multiplet analysis. The determination of cross-correlations and lag times was performed for all pairs of events (e.g. no "master" events) and the cross correlation was calculated for different time windows. More specifically, different tests were performed for the cross-correlations on all three components of the geophone. For each component (i) only P-waves were considered, (ii) only S -wave and (iii) a larger window was taken into account to consider the whole wave train of the earthquake (e.g. 1 s before P-wave arrival and 2 s after S-wave arrival). In practice we found that both P and S phases were easier to identify on the vertical components compared to the horizontals. The best correlation results were obtained in case (iii). Location tests were then performed on the selected multiplet events.

Computation of Focal mechanisms

HASH software (e.g., Hardebeck and Shearer, 2008) was used for computing focal mechanisms of single events of $M>3$. Due to the fact that the majority of the events were micro-earthquakes (e.g. $M<2$), composite focal mechanisms were also computed with HASH for the highly correlated events obtained from the multiplet analysis (see paragraph: Discussion on location results based on case studies). For both cases (e.g. single and composite), at least 8 P-wave first motion polarities (measured on the vertical component) were considered. In total 8 focal mechanisms have been computed (e.g. 4 single and 4 composite focal mechanisms of the events of magnitude $M>3$ and $M<2$ respectively (see

Supplementary Information).

Computation of synthetic tests

The programs of NonLinLoc package were used for calculating the synthetic tests. Given: (i) a hypocenter location and (b) a set of travel time grids (e.g. computed with Grid2Time), Time2Eq was used for calculating the predicted travel times which were then used as input for locating the specific event with NonLinLoc.

Comparing 1D-models, based on synthetics

Different tests were made to evaluate the effect of the different 1D-models on earthquake locations, with the following procedure: i) One arbitrary event was positioned below the Western High, at 40.80°N, 28°E and at 2 different depths, 2 km (Trial 1) and 12 km (Trial 2) respectively; ii) Synthetic travel times were computed using the 3D velocity model, for the stations of the 2011 network (data-set 1); iii) these synthetic travel times were used for relocating the corresponding synthetic epicenters with NonLinLoc, using the "1D-this study" and the 1D-model of (Karabulut *et al.*, 2011), respectively (see Figure 2b). The same test was repeated by using the 3D velocity model of this study (see Figure 2a). As expected, over-simplified 1D models (e.g. models that represent the velocity structure of the on-shore domain), produce very important effects on earthquake depth determination, particularly for shallow events below the deep, submerged basins in contrast with the 3D velocity model which succeeds in well locating the shallow earthquake of Trial 1 (see Table 3). In common practice, 1D-location results are significantly improved by using station corrections, and 1D-models are refined at each iteration. To be effective, however, station corrections require that rays propagate vertically below the station, a valid assumption only for deep-seated earthquakes and smoothly varying media. For shallow earthquakes generating oblique rays in slow, P-wave velocity sediments, 1D-locations with station corrections are less efficient than 3D-locations with station corrections. Therefore, when only OBS are included, it is strongly recommended to use "appropriate 1D-models" that take into account the velocity structure of the upper sediment layers in order to properly locate shallow, micro-seismicity.

Discussion on location results, based on case studies

To illustrate the importance of 3D effects, three representative case studies are discussed here below, with the purpose of comparing the relative location results obtained by NLDiffLoc using "appropriate 1D" models vs the 3D velocity-model. The "appropriate 1D model" used in this study is based on (Cros and Géli , 2013) and shown in Figure 2b. For each case study the 10 m bathymetric grid (see for instance Figure 3) and a selection of a highly correlated events (with a cross correlation coefficient ≥ 0.8, see for example Figure 4) that occurred as clusters or as triplets were considered for the analysis.

- Case study 1: seismicity from the bottom of the basin (~ 5 km):

The first case study includes a triplet of earthquakes of local average magnitude M_l 1.65, that occurred on the 25th of October, 2014, in the Western High area (see Figures 5, 6a, 6b, 7, 8 and Table 4). The seismograms plotted for earthquake 2 (Figure 7) indicate that the P-wave arrived first at OBS4, whilst t_s-t_p values are very large at OBS4. In addition, t_s-t_p are respectively greater at OBS7 and OBS3 (located on the northern side of the MMF) compared to those at OBS8 and OBS1 (located on the northern side). These observations underline the 3-dimensional structure of the medium. The travel-time data (t_s, t_p, t_s-t_p) clearly tell us that: i) the central part of the Western High (e.g. in the vicinity of OBS4) is characterized by extremely low V_P and V_s velocities (likely due to the known presence of mud volcanoes and by gas-prone, low velocity sediment layers); ii) seismic velocities are lower along than across the strike of the MMF.

Location results show that when using the 1D velocity model, hypocenters are located within less than 1 km to the south of the fault zone and at a depth of 10.3 km ± 0.3 km below seafloor. In contrast, with the 3D, high-resolution velocity model, the triplet is found to be located 3 km to the north of the fault zone, at a depth of 6.2 km below seafloor, e.g. at the base of the sedimentary basin. The computed composite focal mechanism (see Supplementary Information) obtained with the 3D locations indicates a predominantly normal fault motion, with a small strike-slip component. In contrast the composite focal mechanism obtained for the 1D locations indicates strike-slip motion while the composite focal mechanism for this triplet is not available in (Yamamoto *et al.*, 2017). Our location results differ from those obtained by (Yamamoto *et al.*, 2017), who found that the cluster was located underneath OBS4, at a hypocentral depth of 15 km (below sealevel), using a 3D-model (10 km × 10 km × 2 km) and OBSs only. The differences between our 3D results and Yamamoto’s are puzzling. Hence, they are further discussed in a subsequent section below (see paragraph: Comparison with (Yamamoto's *et al.*, 2017)).

- Case study 2: shallow seismicity within the upper sediment layers (< 2 km):

The second case study regards a triplet of events (with correlation > 0.8) that occurred on 19th of May 2011 and 23rd of June 2011 (see Figures 9a and 9b and Table 5) of local average magnitude M_l 0.9. With the 1D velocity model, the computed epicenters are spread out over an area of more than ~ 20 km^2 within the eastern part of the Central Basin and the depth distribution of the individual hypocenters is dispersed, at 3 km, 15 km, and 20 km, respectively. In contrast, with the 3D velocity model, the computed epicenters are clustered over an area of ~ 2 km^2 at the base of the escarpment bordering the south-eastern part of the Central Basin, while the hypocenters are located within the first two kilometers of sediments, in an area where numerous gas emission sites have been found and where reverse faulting is present (e.g., Armijo *et al.*, 2002; Bécel *et al.*, 2010). In both cases, the computed composite focal mechanism indicates reverse faulting (see Supplementary Information). It is interesting to note that the 1D locations are unstable, with 3 very different depths (3, 15 and 20 km) found for 3 highly correlated events (see seismograms of the triplet in Supplementary Information), while the 3D-locations yield comparable depths for the 3 events and smaller confidence ellipsoids. The cluster being more or less near the center of the OBS network, small variations in the velocity model are expected to generate large variations in depth determination, resulting in important location instabilities. The seismograms for earthquake 3 (see Figure 10) indicate equivalent

P-wave arrival times at OBS8 and at OBS10, but differences in t_s-t_p greater than 0.4 s. Also, the P-wave arrives 0.2 s earlier, but t_s-t_p is slightly greater (4.0 s) at OBS7 compared to OBS9. These observations suggest large 3D-heterogeneities in the seismic velocity structure, notably with faster velocities across than along strike. In addition, the computed reverse composite focal mechanism is consistent with the presence of a positive (e.g. compressive) flower structure, based on the multi-channel seismic profile SM47 collected during the Seismarmara cruise in 2001 across the NE corner of the Central Basin (Figure 11, after (Bécel *et al.*, 2010)). Gas emissions have been detected near the epicentral area, confirming that the faults rooted in the upper sediment layers are tectonically active, allowing gas to migrate up to the seafloor. The results obtained from the synthetic records for the earthquakes of case study 2 (see Figure 12), indicate that: (i) the P and S arrival times and (ii) the synthetic locations were found to be relatively close to the real data for the 3D model and not for the 1D, which clearly supports our preference for use of a 3D model (see Tables 6 and 7).

- Case study 3: deep, crustal seismicity:

Finally the third case study concerns a cluster of 10 earthquakes of local average magnitude M_l 1.6, that occurred in 2011, below the western part of the Central Basin (see Figure 13 and Table 8). Regardless the model used (1D vs 3D), the computed epicenters are relatively well clustered over areas of less than 10 km^2, and hypocenters are at crustal depths, within the 12-15 km depth range. The composite focal mechanism indicates strike-slip faulting (see Supplementary Information) which is consistent with strike-slip at crustal depth; comparable to the repeaters from the same area reported in (Schmittbuhl *et al.*, 2016). The major difference between 1D vs 3D hypocenters is that the events located with a 1D model are to the south of the fault trace, while those located with the 3D-model are within the shear zone to the north of the MMF. Based on the deep, multi-channel seismic soundings collected during the Seismarmara cruise in 2001, the 3D locations (within the inner basin) appear to be consistent with geology (e.g., Laigle *et al.*, 2008).

1D versus 3D relative locations

As expected, for all case studies, differences in relative location results appear to be significant for shallow (< 6 km) seismicity (case studies 1 and 2), but relatively minor for deep seismicity (e.g. > 10 km, case study 3). In all cases, both our 1D and 3D relative location results are seismologically "well-constrained" based on the criteria that we had set up (see paragraph: Tools and Methodology). Nevertheless, the computed probability density functions (pdf) indicate that the 3D locations have smaller confidence ellipsoids for each event (see Figures 6b, 9b, 13). RMS errors in travel time differences (|measured - calculated|) are displayed in Figure 14.

For each case study, our 3D location results are consistent with the geological knowledge that was acquired during the numerous cruises that were conducted in the SoM since 1999. Although our focal mechanisms have been constrained by a limited number of polarities, the systematic geological consistency of our results cannot be due only to pure coincidence: the deep events (d>10 km) from the case studies have dominantly strike-slip focal mechanisms, while the majority of shallow events (d<5-6 km), have dominantly normal focal mechanisms, except case study 2 where events located near a compressive, flower structure exhibit a reverse focal mechanism.

Discussion

Comparison with (Yamamoto's *et al.,* 2017)

Figure 15 displays the location of the events (14 in total) that were detected in common in this work and in Yamamoto's, during the overlapping period from 19th of September to 14th of November , 2014 (Table 9). The location results provide very different results. West of 27°50'E, (Yamamoto *et al*., 2017) find systematically deep, strike-slip events occurring along the MMF and along EW striking associated structures. These locations are consistent with pure strike-slip motion along the MMF. In contrast our locations suggest normal faulting along SW-NE striking features north of the MMF.

Our locations and Yamamoto's are both internally consistent. The differences, though, are due to differences in:

i) The location method: linear versus non linear (see discussion in (Husen and Hardebeck, 2010)).

ii) The network geometry: we used a network of more than 9 OBSs evenly distributed within a circle of less than 10 km centered on the Western High; (Yamamoto *et al.*, 2017), used an elongated network of 10 OBS stations distributed all along the MMF, with a sparse coverage of only 4 OBSs in our study area (see Figures 6a and 6b).

iii) The 3D velocity model (see paragraph on: 3D velocity structure of the Western Sea of Marmara) of (Yamamoto *et al.*, 2017) used a large mesh grid (10 km × 10 km × 2 km). This naturally induces large effects, particularly due to bathymetry and to lateral variations in surface sediment heterogeneties.

In addition to the above-described case study 1, a new case was considered for comparing the results of Figure 15, by taking as reference earthquake 11, of Table 9. This event was found to be located almost beneath OBS4 in both computations but at a hypocentral depth of ~ 5 km in this study and of ~ 18 km in (Yamamoto's, *et al.*, 2017) respectively (see Figures 15 and 16). The P-wave arrives first at OBS4 (see Figure 17), compared to all other OBSs, which is consistent with location results, that both propose that earthquake 11 is close to OBS4. In contrast, t_P-t_S was found to be:

- maximum at OBS6 (~ 5 s) located ~ 14 km to the east of OBS4.
- minimum at OBS3 (~ 2.78 s) and at OBS1 (~ 3.1 s), respectively located ~11 km to the north and to the south of the MMF.

From the above we conclude that:

- There is a very strong velocity anisotropy within the fault zone, with slower velocities along the strike of the MMF.
- There are very strong velocity anomalies near the central station OBS4, with low V_P, low V_S and ultra-high V_p/V_s in areas near OBS4 where mud volcanoes and gas-prone sediment layers are known to be present.

An alternative view of micro-seismicity within the Sea of Marmara

Our 3D location results provide an alternative view of the micro-seismicity within the Western SoM (Figures 18 and 19) compared to the most recent studies by (Yamamoto *et al.*, 2017) and (Schmittbul *et al.*, 2015). Single (e.g. S1 to S4) and composite focal mechanisms (e.g. C1 to C4) calculated within this study are summarized in Table 10 (see also Supplementary Information).

In the present study, earthquakes are found to occur not only along the axis of the MMF, but also off-axis, along secondary faults from the NAF System (see Figure 20). The deep events (d> 8-10 km) occurring along the MMF have a dominantly strike-slip focal mechanism. In contrast, the majority of shallow events (d<5-6 km) occur off-axis and have a dominantly normal focal mechanism, except at some specific places characterized by compressive deformation. The diversity of the focal mechanisms is consistent with previous results (e.g., Pinar *et al.*, 2003; Sato *et al.*, 2004; Örgülü *et al.*, 2017).

Our results also reveal that there are two categories of shallow (< 6 km) seismicity.

- The first category consists of events located within or at the base of the "post-kinematic", Plio-Quaternary basins (e.g., Bayrakci *et al.*, 2013), at depths of ~ 2 to 6 km and along tectonically active, structural trends oriented E-W or SW-NE.
- The second category includes "ultra-shallow" events, occurring at depths shallower than ~1-2 km (see for instance Figure 21). Focal focal mechanisms may indicate either normal faulting, either reverse (e.g. earthquakes occurring along the Western High and the Central Basin, respectively), depending on the local context . Based on 3D high-resolution seismics (e.g., Thomas *et al.*, 2012) the hypocenters are located within gas prone sediment layers. Such seismicity must be discriminated from the tectonic-related seismicity that occurs at crustal levels.

Implication in terms of triggered "ultra-shallow" (< 2 km) seismicity

Of particular interest is the swarm of aftershocks triggered by the M_l 5.1 strike-slip earthquake (see Table 10) that occurred below the Western High on the 25^{th} of July, 2011. (Géli *et al.*, 2018) proposed that part of these aftershocks occurred within gas-prone sediment layers located shallower than ~ 6 km depth below seafloor, with a predominantly normal focal mechanism (see Table 10). In addition, most of the ultra-shallow (< 2 km) aftershocks occurred along normal (or reverse) faults within sediment layers.

Interestingly, almost all ultra-shallow earthquakes that occurred during the two recording periods of 2011 and 2014 belong to this aftershock sequence, that followed the M_l 5.1 earthquake of July, 25th, 2011. In "normal periods" (e.g. in between two successive earthquakes of moderate magnitude) there is hardly any "ultra-shallow" seismicity. This would suggest that the 'ultra-shallow', soft sediments generally considered to behave aseismically can also respond seismically to stress changes caused by nearby deeper earthquakes, which are at least intermediate in size (i.e. $M_l > 4.5$). This may be explained by observations in rock physics experiments on wet clay-rich sediment where there is a change from velocity strengthening (i.e. an aseismic regime) at slow slip-rates to velocity weakening (i.e. seismic) at high slip-rate (Faulkner *et al.*, 2011; Aretusini *et al.*, 2017). (Faulkner *et al.*, 2011) have postulated that this switch is due to thermal pressurization of pore fluid in the clay. Therefore a possible explanation for the ultra-shallow events are that abrupt stress changes caused by the deeper main shocks may have been large enough to switch the normally aseismic response of the sediment to a seismic one.

This could also explain why (Yamamoto *et al.*, 2017) did not detect any "ultra-shallow" seismicity, as no earthquake of magnitude $M_l > 4$ occurred during the 10 months of recording, from September 2014 to July 2015. (Yamamoto *et al.*, 2017) conclude on page 2080 that: "*Because we recorded no earthquakes of $M_L > 4$, and no events within the sediment layer of the Western High, we consider that microearthquakes identified in the sedimentary layer by other researchers may be aftershocks triggered by moderate earthquakes in upper crust beneath the Western High, as suggested by (Cros and Géli, 2013)*".

Implications in terms of seismic hazards (creeping versus locked)

Our work underlines the difficulties that prevent the accurate depth determination of low magnitude earthquakes, in absence of numerous, near-fault, sea-bottom stations. Consequently, caution is required for interpreting micro-seismicity maps based on low-magnitude threshold. As an example, the micro-seismicity within the SoM reported by (Schmittbuhl *et al.,* 2015) for the period from 2007 to 2012 is plotted in Figure 22 for different threshold levels. For low magnitude thresholds, the maps of micro-seismicity exhibit swarms of vertically distributed events that could be related to the large uncertainties in depth determinations. These vertical swarms entirely disappear for threshold magnitudes above M_l ~ 3 (see Figure 22), suggesting that depth determinations for earthquakes of magnitude above M_l ~ 3 may be used. Between 2007 and 2012, almost all earthquakes of M_l > 3 have occurred at a depth greater than ~ 8 km, along the western segments of the MMF, where most of the gas emissions from the seafloor are found. In contrast only a few earthquakes of magnitude > 3 have occurred along the eastern segments of the MMF, from the Gulf of Izmit to the west of Istanbul.

Previous studies (e.g., Schmittbuhl *et al.,* 2015; Schmittbuhl *et al.,* 2016; Yamamoto *et al.,* 2017 and Bohnhoff *et al.,* 2017) have proposed that the western part of the MMF could be subject to deep crustal creeping, while the segment crossing the Central High, from the Kumburgas basin to the entrance of the Bosphorus, could be locked. This latter result is based on 6 months of acoustic ranging, which did not reveal any significant steady-state surface creep along the MMF offshore Istanbul (e.g., Sakic *et al.,* 2016).

Our results do not contradict this view. Creeping at crustal levels likely induces deformation within the upper sediment layers, which in turn contribute to maintain high permeability within the damage zone, which successively may enhance gas migration up to the surface. In addition the repeated earthquakes of intermediate magnitude may trigger aftershocks within the uppermost, gas-prone sediment layers, which may result in gas emission from the seafloor.

Limitations of our work and perspectives for future research

The conflicting depth estimates certainly pose several questions on the accuracy of the locations, regarding the different methods and velocity models, used here versus the ones of previous studies. Finding the correct earthquake locations in submarine environments is quite a challenge, that mostly depends on (i) the methodology used (e.g. linear versus non-linear techniques), (ii) the velocity model and iii) the network geometry.

By any means, our approach like any other approach has its limitations and advantages. The assumption of a constant V_p/V_s ratio during the location procedure, due to the absence of an S wave velocity model, might have led to a location bias (e.g., Maurer and Kradolfer, 1996). Also, the 3D velocity model of this study does not account for the across-fault variability within the upper sediment structure, which is clearly visible in the seismic sections crossing the Western High (e.g. Figure 8). Specifically, due to technical difficulties, the short scale variability due to the presence of gas below the Western High and the variability between the northern flank and of the southern flank were not considered when building the 3D model of this study.

Yet, despite the limitations of the current approach, here we do think that two different types of seismicity (e.g. deep versus shallow seismicity < 6km) occur in the western part of the SoM. The plausible reasons why the previous studies did not find shallow events in their catalogs are the following: (i) a different geometry of the seafloor seismic network and a consideration of only OBS data were considered for this analysis, (ii) our use of a

3D high resolution velocity model, which was build up with all the available geological and geophysical information from the SoM (see paragraph on: 3D velocity-structure of the Western SoM), (iii) only a limited number of earthquakes was used for the analysis (e.g. 20 %), complying the criteria discussed in Tools and Methodology paragraph catalog, (iv) the use of non-linear methods improved the accuracy of the location solution and (v) additional information based on independent observations (e.g. multi-channel seismics, high-resolution 3D seismics, high-resolution bathymetry) is used for the interpretation of event locations and focal mechanisms.

The perspectives for future work are:

(i) Merge OBS datasets of (Yamamoto's *et al.*, 2017) and of this study for the overlapping observing periods.

(ii) Use a variable V_p/V_s at every single step of the location procedure by independently solving for a V_s model.

(iii) Implement an OBS network with an appropriate layout allowing the depth determination of shallow earthquakes.

(iv) Use land stations for improving the quality of focal mechanisms determinations.

Conclusions

Our results indicate that during the two recording periods (3.5 months in 2011 and 2 months in 2014), not all earthquakes occurred as strike-slip events at crustal depths (> 8 km) along the axis of the MMF. In contrast, a significant number of earthquakes occurred with a predominantly normal focal mechanism, at depths between 2 and 6 km, along tectonically active, structural trends oriented E-W or SW-NE.

The P and S arrivals, suggest that there are strong velocity anomalies along the Western High, with low V_P, low V_S and ultra-high V_P/V_S in areas where mud volcanoes and gas-prone sediment layers are known to be present. Finally, we find that a number of earthquakes having a normal-fault focal mechanism occurred within the upper sediment layers (at depths < 2 km), particularly in the areas where free gas is suspected to exist, based on high-resolution 3D seismics. Most of this ultra-shallow seismicity appears to be related to the presence of gas in shallow sediments and occurs in response to deep intermediate magnitude (M L ~ 4 – 5) earthquakes.

The difficulties to resolve the depth of earthquakes within the SoM, particularly for the shallow seismicity, strongly advocate for the implementation of permanent, seafloor observatories in the close vicinity of the MMF, which represent the only way to conduct high-resolution studies towards a better understanding of the fault behavior.

Data and Resources

- An unpublished bathymetric grid of the Central Basin and Western High, having a node spacing of 10 m, based on multibeam echosounder system data collected in 2014 with *R/V Pourquoi Pas?* This 10 m grid (courtesy of Charline Guérin of Ifremer) is available on request to the authors.
- The two following seismological datasets were analyzed (see details Tables 1 and 2 and in Figure 1b) and are available on request to the authors:
    - Dataset-1 was recorded from 15th of April to 31st of July, 2011, by 10 autonomous, short-period (4.5 Hz) OBSs from Ifremer and by 2 permanent, cabled broad-band OBSs operated by KOERI. Unfortunately, the station in the center of the network stopped recording on 1st of July, 2011.
    - Dataset-2 was recorded from 19th of September to 14th of November, 2014, by 9 autonomous, short-period (4.5 Hz) from Ifremer and by 1 autonomous, broad-band OBS operated by INGV. Note that two autonomous, short-period OBS were also deployed by Ifremer, from the 1st until the 15th of November near the gas emissions site.

The links to the datasets recorded with the OBSs of Ifremer are indicated below:

- Geli Louis, Pelleau Pascal, Batsi Evangelia, Namik Çagatay (2017). Ocean Bottom (OBS) data of the two the temporary seismic networks of Ifremer in 2011 (4 months). SEANOE. http://doi.org/10.17882/49764
- Geli Louis, Pelleau Pascal, Batsi Evangelia, Nurcan Meral Özel (2017). Ocean Bottom (OBS) data of the two the temporary seismic networks of Ifremer in 2014 (2 months). SEANOE. http://doi.org/10.17882/49656

- High-resolution 3D- and 2D-seismic data collected in 2009 with R/V Le Suroit and with R/V Piri Reis, respectively. The full description of the 3D-acquistion system and dataset is detailed in (Thomas *et al.,* 2012). Multi-channel, deep seismic lines collected in 2001 during the Seismara Cruise of R/V Le Nadir were also used (e.g., Laigle *et al.*, 2008; Bécel *et al.*, 2009; Bécel *et al.*, 2010).
- The Gismo collection of Matlab tool boxes was used for seismic waveform analysis, that could be found in https://geoscience-community-codes.github.io/GISMO/ (last acceded February 2017).
- The Sytmis software package for used for the 2011 OBS dataset: (http://www.ineris.fr/centredoc/3202-fp-sytmisauto-0804-an.pdf)

- The non-linear methods developed by Anthony Lomax were used: (*http://alomax.free.fr/alss/)*
- The following scientific reports and articles available on-line were used:

Aktar, M., (2017). Fault Structures in Marmara Sea (Turkey) and Their Connection to Earthquake Generation Processes. In: Active Global Seismology. doi:10.1002/9781118944998.ch8 https://agupubs.onlinelibrary.wiley.com/doi/10.1002/9781118944998.ch8

Cros, E., and L. Géli, (2013). Caracterization of microseimicity in the Western Sea of Marmara: implications in terms of seismic monitoring, Project Report, Institut Carnot Ifremer-Edrome, Abondement 2011, N°06/11/2013, 29 pages, http://dx.doi.org/10.13155/38916

Géli L., N. Çağatay, L. Gasperini, P. Favali, P. Henry and G. Çifçi, (2011). ESONET WP4 – Demonstration Missions. Marmara-DM final report, http://archimer.ifremer.fr/doc/00032/14324/

Gürbüz C., S.E. Isik , L. Géli, E. Cross, (2013). High Resolution Micro Earthquake Characterization, Deliverable D8_2, EU MARSITE PROJECT (New Directions in Seismic Hazard Assessment through Focused Earth Observation in the Marmara Supersite), http://archimer.ifremer.fr/doc/00278/38915/.

Lomax, A., and A. Michelini, (2013). Users Guide for Early-est, Earthquake Rapid Location Sytem with Estimation of Tsunamigenesis, http://early-est.rm.ingv.it/early-est_users_guide.pdf

Lomax, A., (2014). Mise en oeuvre et support pour logiciels de traitement automatisé de données sismologiques acquises dans le cadre du projet Européen FP7 Marsite, Contract report, Reference CNRS, MA201301A, http://alomax.net/projects/marsite/MA201301A_report_v0.2.pdf.

Husen, S., and J.L. Hardebeck (2010) Earthquake location accuracy, Community Online Re source for Statistical Seismicity Analysis, *doi:10.5078/corssa-55815573.* Available at *http://www.corssa.org*.

Acknowledgments

This paper is part of the PhD of Evangelia Batsi, supported by Ifremer and by Région Bretagne ("bourse ARED"). The OBS data were collected with the ESONET Network of Excellence (contract N° 036851) and the MARSITE Integrated Project (contract N° 308417). Jean-François Rolin and Roland Person, coordinators of ESONET as well as Meral Agualdis project manager of MARSITE are warmly acknowledged. Acknowledgments are also addressed to the Turkish Navy and to the Turkish Hydrographic Service (SHOD) for supporting the operations at sea, particularly our correspondent, Captain Erhan Gezgin; to the personnel of the French Embassy in Ankara, specially Mrs Bonnafous-Boucher; to CNR (Comité National Routier) and to Ifremer for funding operations at sea of R/V Le Suroit, R/V Pourquoi pas? and R/V Urania, respectively; to Giuseppe D'Anna, Giuseppe Passafiume and Stefano Speciale of the Istituto Nazionale di Geofisica e Vulcanologia (INGV) of Italy for assisting in the OBS deployment; to the Institute of Marine Science and Technology of the University of Izmir for support with R/V Piri Reis; to Mireille Laigle of Géoazur of Sophia Antipolis University for providing us the seismic profile SM47 (e.g. Figure 4, by (Bécel, *et al.*, 2010)); to Louis Géli for providing us Figure 2a (e.g. Figure A1-3, by (Géli *et al.*, 2018)); to COST_FLOWS (Action ES1301) for supporting a Short Term Scientific Mission (STSM) for E.B.; to Bruno Marsset for his advices and encouragement; to Pascal Pelleau, Mikaël Roudaut and Ronan Apprioual for their technical support; to Sylvain Bermell and Laetitia Morvan, for drafting some of the figures; to Charline Guerin for providing us the grid of high resolution bathymetry at 10 m; to professor Oguz Özel, for his support for using R/V Yunuz of Istanbul University; to Jean Schmittbuhl, Hayrullah Karabulut and Jean-Robert Grasso for their participation to the PhD Thesis committee. Intense use was made of Global Mapping Tools (GMT) and ArcGIS. All the data used in

this paper are available on request to the authors.

References

Aktar, M., (2017). Fault Structures in Marmara Sea (Turkey) and Their Connection to Earthquake Generation Processes. In: Active Global Seismology. doi:10.1002/9781118944998.ch8.

Ambraseys, N.N. and C. Finkel, (1987). The Saros-Marmara earthquake of 9 August 1912, *J. Earthq. Eng. Struct. Dyn.*, **15**, 189-211.

Ambraseys, N.N and C. Finkel, (1995). The Seismicity of Turkey and adjacent areas. A historical review, 1500-1800, *Istanbul: Eren Yayincilik*, 240 pp.

Aretusini, S., S., Mittempergher, O. Plümper, E. Spagnuolo, A. F. Gualtieri, and G. Di Toro (2017), Production of nanoparticles during experimental deformation of smectite and implications for seismic slip, *Earth and Planet. Sci. Lett.*, *463*, 221–231, doi:10.1016/j.epsl.2017.01.048.

Armijo, R., B. Meyer S. Navarro, G. King, and A. Barka, (2002). Asymetric slip partitioning in the Sea of Marmara pull-apart: a clue to propagation process of the North Anatolian Fault? *Terra Nova*, **14**, 80-86.

Armijo, R., N. Pondard, B. Meyer, G.Ucarkus, B. de Lepinay, M., Malavieille, J. Dominguez, S. Gustcher, M. A. Schmidt, S. Beck, C. *et al.*, (2005). Submarine fault scarps in the Sea of Marmara pull-apart (North Anatolian Fault): implications for seismic hazard in Istanbul, *Geochem. Geophys. Geosyst.*, **6**, Q06009, doi:10.1029/2004GC000896.

Bayrakci G., M. Laigle, A. Bécel, A. Hirn, T. Taymaz, S. Yolsal-Çevikbilen,, and SEISMARAMARA team (2013). 3-D sediment-basement tomography of the NorthernMarmara trough by a dense OBS network at the nodes of a grid of controlled source profiles along the North Anatolian fault, *Geophys. J. Int*., doi: 10.1093/gji/ggt211.

Bécel, A., (2006). Structure Sismique de la Faille Nord Anatolienne en Mer de Marmara, Phd Thesis, Institut de Physique du Globe de Paris.

Bécel, A., M. Laigle, B.De Voogd, A. Hirn, T. Taymaz, A. Galvé, H. Shimamura, Y. Murai, JC Lépine, M. Sapin, andS. Özalaybey, (2009). Moho, crustal architecture and deep deformation under the North Marmara Trough, from the SEISMARMARA Leg 1 offshore-onshore reflection-refraction survey, *Tectonophysics* **467**: 1-21.

Bécel, A., M. Laigle, B. De Voogd, A. Hirn, T. Taymaz,, S. Yolsal-Cevikbilen, H. Shimamura, (2010): North Marmara Trough architecture of basin infill, basement and faults, from PDSM reflection and OBS refractions seismics, *Tectonophysics* **490: 1-14.**

Bourry, C., B. Chazallon, JL Charlou, JP Donval, L. Ruffine, P. Henry, L. Géli, M. Çagatay, S. İnane, and M. Moreau, (2009). Free gas and gas hydrates from the Sea of Marmara, Turkey: Chemical and structural characterization. *Chem. Geol*., doi:10.1016/j.chemgeo.2009.03.007.

Carton, H., S.C. Singh, A. Hirn, B. Bazin, B. de Voogd, A. Vigner, A. Ricolleau, S. Cetin, N. Oçakoglu, F. Karakoç, V. Sevligen, (2007). Seismic imaging of the three-dimensional architecture of the Çınarcık Basin along the North Anatolian Fault, *J. Geophys. Res.*, **112**, B06101, doi: 10.1029/2006JB004548.

Cros, E., and L. Géli, (2013). Caracterization of microseimicity in the Western Sea of Marmara: implications in terms of seismic monitoring, Project Report, Institut Carnot Ifremer-Edrome, Abondement 2011, N°06/11/2013, 29 pages.

De Landro, G., O. Amoroso, TA Stabile, E. Martullo, A. Lomax and A. Zollo, (2015). High precision Differential Earthquake Location in 3D models: Evidence for a rheological barrier controlling the microseismicity at the Irpinia fault zone in southern Apennines, *Geophys. J. Int.*, 203 (3): 1821-1831, doi:10.1093/gji/ggv397

Dupré S., C. Scalabrin C., C. Grall, J-M Augustin, P. Henry, A. M. C Sengor, N. Görür, M. N. Cagatay andL. Géli (2015). Tectonic and sedimentary controls for widespread gas emissions in the Sea of Marmara, Results from systematic, ship-borne multibeam echosounder water column imageries, *J. Geophys. Res.*, doi: 10.1002/2014JB011617.

Faulkner, D. R., T. M. Mitchell, J. Behnsen, T. Hirose, and T. Shimamoto (2011). Stuck in the mud? Earthquake nucleation and propagation through accretionary forearcs, *Geophys. Res. Lett*, *38* (18), doi:10.1029/2011GL048552.

Géli, L., P. Henry, T. Zitter, S. Dupré, M. Tryon, M.N. Çağatay, B. Mercier de Lépinay,,

X. Le Pichon, A.M.C. Şengör, N. Görür , *et al.*, (2008). Gas emissions and active tectonics within the submerged section of the North Anatolian Fault zone in the Sea of Marmara. *Earth Planet. Sci. Lett*., **274(1-2):** 34-39.

Géli L., N. Çağatay, L. Gasperini, P. Favali, P. Henry and G. Çifçi, (2011). ESONET WP4 Demonstration Missions. Marmara-DM final report.

Géli, L., J. Piau, M., Dziak, R., Maury, V., Fitzenz, D., Coutellier, Q., and P. Henry, (2014), Seismic Precursors linked to Highly Compressible Fluids at Oceanic Transform Faults, *Nature Geoscience*, doi:10.1038/NGEO2244

Géli, L., P. Henry, C. Grall, J.B. Tary, A. Lomax, E. Batsi, C. Cros, C. Gürbüz, S.E. Isik, A.M.C. Şengör *et al.*, (2018). Gas related seismicity within the Istanbul seismic gap, *Nature Scientific Reports.*

Grall, C., P. Henry, D. Tezcan, B. Mercier de Lepinay, A. Bécel, L. Géli, J-L. Rudkiewicz, T. Zitter, F. Harmegnies, (2012). Heat flow in the Sea of Marmara Central Basin, possible implications for the tectonic evolution of the North Anatolian Fault, *Geology*, **40:3-6**, doi:10.1130/G32192.32191.

Grall, C., P. Henry, Y. Thomas, G.K. Westbrook, .M. N. Çağatay, B. Marsset, H. Saritas, G. Çifçi, and L. Géli, (2013). Slip rate estimation along the western segment of the Main Marmara Fault over the last 330 ka by correlating Mass Transport Deposits, *Tectonics*, 10.1002/2012TC003255.

Gürbüz C., M. Aktar, H. Eyidogan, A. Cisternas, H. Haessler, A. Barka, M. Ergin, N. Türkelli, O. Polat, S.B Üçer, S. Kuleli, *et al.*, (2000). The seismotectonics of the Marmara region (Turkey): results from a micro-seismic experiment. *Tectonophysics* 316, 1–17.

Gürbüz C.,S.E. Isik L. Géli, E. Cross, (2013). High Resolution Micro Earthquake Characterization, Deliverable D8_2, EU MARSITE PROJECT (New Directions in Seismic Hazard Assessment through Focused Earth Observation in the Marmara Supersite).

Hausmann, H., S. Hoyer, B. Schurr , E. Brückl, G. Houseman, and G. Stuart, (2010). New seismic data improve earthquake location in the Vienna Basin area, Austria, *Austrian Journal of Earth Sciences*, **103**, 2-14, Vienna.

Hardebeck, J.L. and Shearer, P.M., (2002). A new method for determining first- motion focal mechanisms, *Bull. Seism. Soc. Am.*, **92**, 2264-2276.

Hardebeck, J.L. and P.M. Shearer, (2003). Using S/P Amplitude Ratios to Constrain the Focal Mechanisms of Small Earthquakes, *Bull. Seism. Soc. Am*, **93**, 2434-2444.

Hardebeck, J.L. and P.M Shearer, (2008). HASH : A Fortran program for computing Earthquake First-Motion Focal Mechanisms -v1.2 – January 31

Helmstetter A., (2002). Is Earthquake Triggering Driven by Small Earthquakes, *Phys. Rev. Lett.* **91**, 058501.

Husen, S., and J.L. Hardebeck (2010). Earthquake location accuracy, Community Online Resource for Statistical Seismicity Analysis, doi:10.5078/corssa-55815573.

Imren, C., *X.* Le Pichon, C. Rangin, E. Demirbağ, B. Ecevitoğlu,, N. Görür, (2001). The North Anatolian Fault within the Sea of Marmara: a new interpretation based on multichannel seismic and multi-beam bathymetry data, *Earth Plan. Sci. Lett*., **186**,143–158, doi:10.1016/S0012-821X(01)00241-2.

Karabulut, H., J. Schmittbuhl, S. Özalaybey, O. Lengliné, A. Kömeç-Mutlu, V. Durand, M. Bouchon, G. Daniel, M.P Bouin,. (2011). Evolution of the seismicity in the eastern Marmara Sea a decade before and after the 17 August 1999 Izmit earthquake, *Tectonophysics*, **510**, 17–27.

King G.C.P., S. Ross, J. Lin, (1994). Static stress changes and the triggering of earthquakes, *Bull. Seism. Soc. Am.* **84**, 3, 935-953.

Kuscu, I.,M. Okamura, H. Matsuoka, E. Gökaşan, Y. Awata, H. Tur, Şimşek and M. Keçer, (2005). Seafloor gas seeps and sediment failures triggered by the August 17, 1999 earthquake in the Eastern part of the Gulf of Izmit, Sea of Marmara, NW Turkey. *Mar. Geol.* **215**, 193–214.

Laigle M., A. Becel, B. De Voogd, A. Hirn, T. Taymaz, S. Ozalaybey, and Members of SEISMARA Leg1 Team (2008). A first seismic survey in the Sea of Marmara: Deep basins and whole crust architecture and evolution, *Earth Planet. Sci. Lett*, **270**, 168-179.

Le Pichon, X., A.M.C. Şengör , E. Demirbağ , C. Rangin, C. Imren, R. Armijo, Görür, N. Çağatay, B. Mercier de Lepinay, *et al.*, (2001). The active Main Marmara Fault, *Earth Planet. Sci. Lett*., **192**, 595–616.

Lomax, A. (2008), Location and Tectonics of the Focal Region of the California Earthquake of 18 April 1906, Bull. Seism. Soc. Am., 98, 846-860.

Lomax, A., A. Michelini, and A. Curtis,, (2009). Earthquake Location, Direct, Global-Search Methods, in Complexity In *Encyclopedia of Complexity and System Science, Part 5*, Springer, New York, pp. 2449-2473, doi:10.1007/978-0-387-30440-3.

Lomax, A., C. Satriano, and M. Vassallo, (2012). Automatic picker developements and optimazation: FilterPicker - a robust broadband picker for real - time seismic monitoring and earthquake early - warning, Seism. Res. Lett., **83**, 531-540, doi : 10.1785/gssrl.83.3.531.

Lomax, A., and A. Michelini, (2013). Users Guide for Early-est, Earthquake Rapid Location Sytem with Estimation of Tsunamigenesis, see link in « Data and Resources » section.

Lomax, A., (2014). Mise en oeuvre et support pour logiciels de traitement automatisé de données sismologiques acquises dans le cadre du projet Européen FP7 Marsite, Contract report, Reference CNRS, MA201301A.

Maurer, H., and U. Kradolfer (1996). Hypocentral parameters and velocity estimation in the western Swiss Alps by simultaneous inversion of P- and S-wave data, *Bull. Seism. Soc. Am.*, 86, 32-42.

Örgülü, G., (2011). Seismicity and source parameters for small-scale earthquakes along the splays of the North Anatolian Fault (NAF) in the Marmara Sea, *Geophys. J. Int.* **184**, 385–404 doi:10.1111/j.1365-246X.2010.04844.x

Parsons T., (2004). Recalculated probability of M>7 earthquakes beneath the Sea of Marmara. *J. Geophys. Res*., **109**, doi:10.1029/2003JB002667.

Pinar A., K. Kuge, and Y. Honkura,. (2003). Moment tensor inversion of recent small to moderate sized earthquakes: implications for seismic hazard and active tectonics beneath the Sea of Marmara, *Geophys. J. Int.*, **153**, 133–145.

Pondard N., R. Armijjo, G.C.P. King, and B. Meyer, (2007). Fault interactions in the Sea of Marmara pull-apart (North Anatolian Fault): earthquake clustering and propagating earthquake sequences, *Geophys. J. Int.* (2007), **171**, 1185-1197, doi: 10.1111/j.1365-246X.2007.03580.x.

Rangin, C., E. Demirbag, C. Imren., A. Crusson,, E. Le Drezen, A. Le Bot, (2001). Marine Atlas of the Sea of Marmara (Turkey). Data collected on board R.V Le Suroît, September 2000.

Rangin, C., X. Le Pichon, E. Demirbag, and C. Imren, (2004). Strain localization in the Sea of Marmara: Propagation of the North Anatolian Fault in a now inactive pull-apart, *Tectonics*, 23, TC2014, doi:10.1029/2002TC001437.

Ruffine, L., Y. Germain, A. Polonia, A. De Prunelé, C. Croguennec, J-P Donval., M. Pitel-Roudaut, E. Ponzevera, J-C. Caprais, C. Brandily, (2015). Pore water geochemistry at two seismogenic areas in the Sea of Marmara, *Geochem. Geophys. Geosyst.*, **16**, 2038–2057, doi:10.1002/2015GC005798.

Ruffine, L., O. Fandino, J. Etoubleau, S. Chéron,, J-P. Donval, Y. Germain, E. Ponzevera, V. Guyader, B. Dennielou, Etiope, *et al.*, (2012). Geochemical dynamics of the natural-gas hydrate system in the Sea of Marmara, offshore Turkey, *Advances in Natural Gas Technology*, *ISBN 978-953-51-0507-7*, pp. 29-56.

Sakic, P., H. Piété, V. Ballu, J.-Y. Royer, H. Kopp, D. Lange, F. Petersen, S. Özeren, S. Ergintav, L. Géli, P. Henry, A. Deschamps (2016). No significant steady state surface creep along the North Anatolian Fault offshore Istanbul: Results of 6 months of sea floor acoustic ranging,
Geophys. Res. Lett., **43**, 6817–6825, doi:10.1002/2016GL069600.

Sato, T., J. Kasahara, T. Taymaz, M. Ito, A. Kamimura, T. Hayakawa, andO. Tan, (2004). A study of microearthquake seismicity and focal mechanisms within the Sea of Marmara (NW Turkey) using ocean bottom seismometers (OBSs), *Tectonophysics*, **391:303**, 314. doi:10.1016/j.tecto.2004.07.018.

Schmittbuhl, J.,H. Karabulut, O. Lengliné, and M. Bouchon, (2015). Seismicity distribution and locking depth along the Main Marmara Fault, Turkey, *Geochemistry*, *Geophysics*, *Geosystems*, DOI 10.1002/2015GC006120.

Schmittbuhl, J., H. Karabulut, O. Lengliné, and M. Bouchon, (2016). Long-lasting seismic repeaters in the Central Basin of the Main Marmara Fault, *Geophys. Res. Lett.,* **43**, 9527–9534, doi:10.1002/2016GL070505.

Shillington, D. J., L., Seeber, C. C. Sorlien, M. S. Steckler, H. Kurt, D. Dondurur, G. Çifçi, C. İmren, M.-H. Cormier, C.M.G. McHugh, S. Gürçay, D. Poyraz, S. Okay, O. Atgın , J.B. Diebold (2012). Evidence for widespread creep on the flanks of the Sea of Marmara transform basin from marine geophysical data. *Geology*; **40 (5)**: 439–442.

Şengör, A. M. C.,O. Tüysüz, C.· İmren, M. Sakınç, H. Eyidoğan, N. Görür, X. Le Pichon, and C. Rangin, (2005). The North Anatolian Fault: A new look, *Annu. Rev. Earth Planet. Sci*., **33**, 37–112, doi:10.1146/annurev.earth.32.101802.120415.

Şengör, A.M.C., C. Grall, C. Imren, X. Le Pichon, Görür, P. Henry, H. Karabulut, and M. Siyako (2014). The geometry of the North Anatolian transform fault in the Sea of Marmara and its temporal evolution: Implications for the development of intra-continental transform faults, *Can. J. Earth Sci*., **51(3)**, 222–242, doi:10.1139/cjes-2013-0160.

Steacy, S., J. Gomberg, and M. Cocco, (2005). Introduction to special section: Stress transfer, earthquake triggering, and time-dependent seismic hazard, *J. Geophys. Res*., **110**, B05S01, doi:10.1029/2005JB003692.

Stein, R. S., A.A. Barka, and H. Dieterich, (1997). Progressive failure on the North Anatolian fault since 1939 by earthquake stress triggering, *Geophys. J. Int.*, **128**, 594-604.

Tary, J.-B, L. Géli, P. Henry, B. Natalin, L. Gasperini, M. Çomoğlu, N. Çağatay, and T. Bardainne, (2011). Sea-Bottom Observations from the Western Escarpment of the Sea of Marmara, *Bull. Seism. Soc. Am.*,

101 (2), 101, 775–791, doi: 10.1785/0120100014

Thomas, Y., B. Marsset, G. Westbrook, C. Grall, L. Géli, G.Cifci, A. Rochat and H. Sartas, (2012). Contribution of high-resolution 3D seismic near-seafloor imaging to reservoir scale studies: application to the active north Anatolian Fault, Sea of Marmara, *Near Surface Geophysics*, **10**, 291-301, doi:10.3997/1873-0604.2012019

Waldhauser, F., and W.L. Ellsworth, (2000). A double-difference earthquake location algorithm: Method and application to the northern Hayward fault, Bull. Seismol. Soc. Am., 90, 1353-1368.

Yamamoto, Y., N. Takahashi, A. Pinar, D. Kalafat, S. Citak, M. Comoglu, R. Polata, and Y. Kaneda, (2017). Geometry and segmentation of the North Anatolian Fault beneath the Marmara Sea, Turkey, deduced from long-term ocean bottom seismographic observations, JGR, doi:10.1002/2016JB013608

MAILING LIST OF AUTHORS

Order of Authors:

Corresponding Author Dr. Evangelia Batsi (E-Mail: Evangelia.Batsi@ifremer.fr)

Dr. Anthony Lomax (E-Mail: alomax@free.fr)

Dr. Jean-Baptiste Tary (E-Mail: jb.tary@uniandes.edu.co)

Dr. Frauke Klingelhoefer (E-Mail: Frauke.Klingelhoefer@ifremer.fr)

Dr. Vincent Riboulot (E-Mail: Vincent.Riboulot@ifremer.fr)

Dr. Shane Murphy (E-Mail: Shane.Murphy@ifremer.fr)

Dr. Stephen Monna (E-Mail: stephen.monna@ingv.it)

Dr. Nurcan Meral Özel (E-Mail: Nurcan.Meral.Ozel@ctbto.org)

Dr. Dogan Kalafat (E-Mail: kalafato@boun.edu.tr)

Dr. Hakan Saritas (E-Mail: hakan.saritas@mta.gov.tr)

Dr. Günay Cifçi (E-Mail: gunay.cifci@deu.edu.tr)

Dr. Namik Çagatay (E-Mail: cagatay@itu.edu.tr)

Dr. Luca Gasperini (E-Mail: luca.gasperini@ismar.cnr.it)

Dr. Louis Géli (E-Mail: Louis.Geli@ifremer.fr)

LIST OF FIGURE CAPTIONS (1 to 22)

Figure 1: (1a) General view of the SoM between the Black Sea and the Aegean Sea. Black lines indicate the main structural features of the MMF (e.g., Şengör *et al.*, 2005). Black box correspond to Fig. 1b. Abbreviations: TB: Tekirdag basin; WH: Western High; CB: Central Basin; KB: Kumburgaz basin; CH: Central High; ÇB: Çinarcik Basin.

(1b) Bathymetric map of the study area within the Western SoM, displaying the position of the OBSs used for this study, along with the delimitation of the boxes shown in Figures 3, 6b, 9b, and 13. Temporary seismic networks of Ifremer in 2011 and 2014 are shown with yellow and red triangles, respectively, while the one of INGV (in 2014) is represented by a purple triangle. The permanent OBS stations of KOERI (green triangles) were operating in 2011 but not in 2014. Black lines are for active faults (e.g., Şengör *et al.*, 2005). Green dots indicate acoustically detected gas emission sites, after (Dupré *et al.*, 2015). White circles show the center of the clusters of case study 1 (CS1), 2 (CS2) and 3 (CS3), respectively.

Figure 2: (2a) From (Cros and Géli, 2013). See also Appendix 1 in (Géli *et al.*, 2018). Contours of the pre-kinematic basement depth, from Figure 13a of (Bayrakci *et al.*, 2013), are here super-imposed on the bathymetric map of the Western SoM, based on the high resolution, 38 m grid from (Le Pichon *et al.*, 2001). Red dots indicate grid nodes from the low-resolution (6 km × 6 km × 2 km) grid of (Bayrakci *et al.*, 2013). Black dots indicate

the nodes of the high-resolution grid (0.75 km × 0.75 km × 0.2 km) used in this study. Labels from 1 to 9 on the basement iso-depth contours indicate 9 different velocity domains: red dots within iso-contour 1 share the same 1D-velocity profile within the pre-kinematic basement; so do all red dots located between iso-contours 2 and 3, etc. The velocity profile below the pre-kinematic basement is based on (Bécel *et al.*, 2009), as described in (Cros and Géli, 2013). Finally, the 1D velocity profile below each black dot is obtained by interpolating the velocity profile from the surrounding red nodes.

(2b) 1D-velocity models used in previous studies of seismicity within the SoM (where dash-dot line, plus sign, circle and solid line correspond to the models by ((Tary *et al.*, 2011); (Gürbüz *et al.*, 2000) and (Karabulut *et al.*, 2011)) respectively, along with the 1D-model used in this study (solid line) and described in (Cros and Géli, 2013).

Figure 3: Detailed bathymetric map of the Western High having a node spacing of 10 m (contour interval: 100 m, see Data and Resource section). The bathymetric grid is still unpublished and available on request to the authors (Courtesy of Charline Guérin, Ifremer). Dashed black line A2-08 is the 2D-high resolution seismic line displayed in Figure 8. Black boxes correspond to Figures 6b, 20 and 21. Continuous black lines indicate the main structural features of the MMF. Temporary seismic networks of Ifremer in 2011 and 2014 are shown with yellow and red triangles, respectively, while the one of INGV (in 2014) is represented by a purple triangle. The permanent OBS stations of KOERI (green triangles) were operating in 2011 but not in 2014.

Figure 4: Matrix of cross correlation for all events recorded during the 2014 deployment, by the central station OBS4, on the vertical component. White arrows indicate highly correlated events, e.g: the triplet (cc > 0.9) of 25th of October 2014, selected for Case

Study 1 (Figure 5).

Figure 5: Case study 1. Seismograms from the vertical (left panel) and horizontal 1 (right panel) components corresponding to the triplet (with cc>0.9) recorded by the central OBS4 station of the 2014 network on the 25th of October 2014.

Figure 6: Case study 1. 6a) Distribution of OBSs (shown by black triangles) used in this study for the location of earthquake 2 of case study 1 (see seismograms in Figure 7). White star, circle and diamond indicate the 1D (this study), the 3D (this study) and the (Yamamoto *et al.*, 2017) locations, respectively. The distances (in kilometers) from the 3D location of earthquake 2 to each OBS are indicated in black. Note that OBS10 (e.g. shown with a black cross) stopped working 3 days before the occurrence of the events of case study 1. Note that paths to OBS4 necessarily cross mud volcanoes and gas-prone sediment layers. Black box corresponds to Fig. 6b. Black lines indicate the main structural features of the MMF (e.g., Şengör *et al.,* 2005).

6b) Left panel indicates the relocated epicenters for the triplet shown in Figure 5, obtained using respectively the 1D (stars), the 3D (circles) velocity models of this study and the 3D velocity model by (Yamamoto *et al.,* 2017) (white diamonds). The right panel indicates the N-S cross-section with the relocated hypocenters. The probabilistic, relative location uncertainties obtained by NLDiffLoc are displayed by black ellipsoids showing the projection of the 68% confidence ellipsoid for each earthquake with their pdf (probability density functions) indicated by blue and red dots, for the 1D and 3D velocity models respectively. Red beachballs show the composite focal mechanism solution calculated for the triplet events. Numbers 1 to 3 correspond to the number of each individual event listed in Table 4. Line A2-08 is the 2D-high resolution seismic line displayed in Figure 8. Green dots correspond to gas emissions sites, after (Dupré *et al.*, 2015). Note that OBS10 (e.g. shown with a yellow cross) stopped working 3 days before the occurrence of the events of case study 1. See polarities and characteristics of composite focal mechanisms of 3D locations in Supplementary Information.

Figure 7: Seismograms from earthquake 2 (25th of October, 2014) of case study 1 recorded at seafloor stations 1, 8, 4, 7, 5 and 3 of the 2014 OBS network. Dotted lines indicate t_p and t_s arrivals at each different OBS. The upper panel displays the vertical component (e.g. Z) and the bottom panel is for Horizontal-1 (e.g. H1).

Figure 8: (a) Upper panel: 2D-high resolution seismic section along line A2-08 (see track line location in Figure 3) collected in 2009 with Piri Reis. (b) Bottom panel: Interpretation of seismic profile A2-08 (this study).

Figure 9: Case Study 2, presented for a triplet of highly correlated events (cc > 0.8) that occurred on the 19th of May 2011 and on the 23rd of June 2011. 9a) Distribution of OBSs (shown by black triangles) used in this study for the location of earthquake 3 of case study 2 (see seismograms in Figure 10). White star and white circle indicate the 1D (this study) and the 3D (this study) locations, respectively. Black lines indicate the distance of 3D location to each OBS station. Dashed black line indicated the profile SM47 shot during the Seismarmara cruise in 2001 across the eastern side of the Central Basin. Black box corresponds to figure Fig. 9b. Black lines indicate the main structural features of the MMF (e.g., Şengör *et al.*, 2005).

9b) Left panel indicates the relocated epicenters obtained using respectively the 1D (stars), the 3D (circles) velocity models of this study. Upper right panels indicate N-S cross-section with the relocated hypocenters. The probabilistic, relative location uncertainties obtained by NLDiffLoc are displayed by black ellipsoids showing the projection of the 68% confidence ellipsoid for each earthquake with their pdf (probability density functions) indicated by blue and red dots, for the “this study 1D” and 3D velocity models respectively. Numbers 1 to 3 correspond to the number of each individual event listed in Table 5. Red beachball shows the composite focal mechanism solution calculated for the triplet. Green dots correspond to gas emissions sites, after (Dupré *et al.*, 2015). See polarities and characteristics of composite focal mechanisms of 3D locations in Supplementary Information.

Figure 10: Seismograms for event 3 of case study 2, recorded at OBSs 7, 8, 9 and 10 on the 23rd of June 2011. Horizontal arrows indicate the t_s-t_p arrival at each different OBS. The upper panel displays the vertical component (e.g. Z) and the bottom panel is for Horizontal-1 (e.g. H1).

Figure 11: (after Figure 4, of (Bécel *et al.*, 2010)): Relocated hypocenters (orange circles) of 2011 recording period, projected along the pre-stack depth migrated section (Line SM47) shot during the Seismarmara cruise in 2001 across the eastern side of the Central Basin. Line track is indicated in Figure 9a. Interpretations (yellow, red and brown lines) are from (Bécel *et al.*, 2010). Note that the most shallow (at depths < 3 km) hypocenters are near or within to the positive flower structure underlined by the black box (see case study 2, Figure 9b).

Figure 12: Schematic diagram showing the steps that were followed for the synthetic test of case study 2.

Figure 13: Case study 3. Left panel indicates the relocated epicenters of the cluster of events that occurred from the 26^{th} of April 2011 until the 18^{th} of May 2011, obtained using respectively the 1D (stars), the 3D (circles) velocity models of this study. The right panel indicates the N-S cross-section with the relocated hypocenters. The probabilistic, relative location uncertainties obtained by NLDiffLoc are displayed by black ellipsoids showing the projection of the 68% confidence ellipsoid for each earthquake with their pdf (probability density functions) indicated by blue and red dots, for the "this study 1D" and 3D velocity models respectively. Red beachball shows the composite focal mechanism solution calculated for the cluster events. Numbers 1 to 10 correspond to the number of each individual event listed in Table 8. Green dots correspond to gas emissions sites, after (Dupré *et al.*, 2015). See polarities and characteristics of composite focal mechanisms of 3D locations in Supplementary Information.

Figure 14: Comparison of RMS errors of absolute location (e.g. use of NonLinLoc) obtained for the case studies 1 to 3, for the velocity models 1D (black bins) and 3D (gray bins) of this study. Event number for each case study is indicated (see Tables 4, 5 and 8).

Figure 15: Comparison of location results for the common events, listed both in (Yamamoto *et al.*, 2017) (light green diamonds) and in this work (salmon circles), that occurred during the overlapping period, from 19^{th} of September to 14^{th} of November, 2014. Labels (from 1 to 14) correspond to the number of each individual event listed in Table 9 and are connected with yellow lines. Red beachball shows the focal mechanism solution of the triplet of case study 1 (see Table 10). Green dots correspond to gas emissions sites, after (Dupré *et al.*, 2015). Bathymetric map of upper left panel with a node spacing of 10 m and contour interval of 20 m (see Data and Resource section). Black lines indicate main

structural features, after (Şengör *et al.*, 2005).

Figure 16: Distribution of OBSs (shown by black triangles) used in this study for the location of earthquake 11 of Figure 15 (see seismograms in Figure 17). White circle and diamond indicate the 3D (this study) and the (Yamamoto *et al.*, 2017) locations, respectively. The distances (in kilometers) from the 3D location of earthquake 11 to each OBS are indicated in black. Note that OBS10 (e.g. shown with a black cross) stopped working 3 days before the occurrence of the earthquake 11. Note that paths to OBS4 necessarily cross-mud volcanoes and gas-prone sediment layers. Black lines indicate the main structural features of the MMF (e.g., Şengör *et al.*, 2005).

Figure 17: Seismograms from earthquake 11 (25th of October, 2014) of Figure 17, recorded at seafloor stations 1, 3, 4, 5, 6, 7 and 8 of the 2014 OBS network. Dotted lines indicate tp and ts arrivals at each different OBS. The upper panel displays the vertical component (e.g. Z) and the bottom panel is for Horizontal-1 (e.g. H1).

Figure 18: Upper left panel indicates the relocated epicenters (obtained using the 3D velocity model) for the 2011 recording period, including also the mainshock of the 25th of July and its sequence of aftershocks (e.g. 15th of April until the 31st of July 2011). The lower left and upper right panels indicate E-W and N-S cross-sections of the relocated hypocenters. Red beachballs show the focal mechanisms solutions, with white labels indicating the name, local magnitude and depth for each case (see Table 10). Yellow triangles show the temporary OBS stations of Ifremer during the 2011 recording. Green dots correspond to gas emissions sites, after (Dupré *et al.*, 2015). Black lines are for active faults (e.g., Şengör *et al.*, 2005). The size of the orange circles is proportional to their

local magnitude (e.g. 0.5 <M< 5.1). Bathymetric map in upper left panel is with node spacing of 10 m (see Data and Resource section). See polarities and characteristics of composite focal mechanisms of 3D locations in Supplementary Information.

Figure 19: Upper left panel indicates the relocated epicenters (obtained using the 3D velocity model) for the recording period from September 19th to November 14th, 2014. The lower left and upper right panels indicate E-W and N-S cross-sections of the relocated hypocenters. Red beachballs show the focal mechanisms solutions with white labels indicating the name, local magnitude and depth for each case (see Table 10). Red and orange (OLD-OBS) triangles show the temporary OBS stations of Ifremer during the 2014 recording, while the purple triangle show the temporary OBS station of INGV. Green dots correspond to gas emissions sites, after (Dupré *et al.*, 2015). Black lines are for active faults (e.g., Şengör *et al.*, 2005). The size of the salmon circles is proportional to their local magnitude (e.g. 0.5 <M< 3.3). Bathymetric map (upper left panel) with node spacing of 10 m (see Data and Resource section). See polarities and characteristics of composite focal mechanisms of 3D locations in Supplementary Information.

Figure 20: A synthesis map of the relocated epicenters (using our 3D velocity model) during the 2011 (orange circles) and 2014 (salmon circles) recording periods. Red triangles show the temporary OBS stations of Ifremer during the 2014 recording period. Green dots correspond to gas emissions sites, after (Dupré *et al.*, 2015). The bathymetric map of the Western High is with a node spacing of 10 m (see Data and Resource section). Black dashed line indicates seismic line A2-08 (see Figure 8).

Figure 21: Map presenting the shallower (depth < 4 km), well constrained, relocated

aftershocks (using our 3D velocity model) that followed the M5.1 earthquake of the 25^{th} of July, 2011. Green dots correspond to gas emissions sites, after (Dupré *et al.*, 2015). The bathymetric map of the Western High is with a node spacing of 10 m and contour interval of 20 m (see Data and Resource section). Red beachball shows the composite focal mechanism solution of the aftershocks (see Table 10). See polarities and characteristics of composite focal mechanisms of 3D locations in Supplementary Information.

Figure 22: Thresholded" seismicity maps between 2007 and 2012, after (Schmittbuhl *et al.*, 2015) displaying events of magnitude (M_l) above 3.0 (top); 2.6 (middle) and 2.0 (bottom), respectively. The "vertical" swarms of seismicity disappear for a threshold magnitude of M_l ~ 3.

Table 1

Table 1: Table of coordinates and operation period of the temporary and permanent OBS stations of data-set 1.

OBS code	Latitude (°N)	Longitude (°E)	Depth (m)	Recording period
OBS1	40.8848	27.6996017	1024	15 Apr. - 31 July
OBS2	40.817055	27.7804433	652	15 Apr. - 30 June
OBS3	40.750405	27.700185	516	15 Apr. - 31 July
OBS4	40.8611483	28.580295	328	15 Apr. - 31 July
OBS5	40.733415	27.920655	775	15 Apr. - 31 July
OBS6	40.84155	27.9155833	906	15 Apr. - 31 July
OBS7	40.786225	28.040535	1100	15 Apr. - 31 July
OBS8	40.88608	28.0778767	1181	15 Apr. - 31 July
OBS9	40.7344117	28.143615	634	15 Apr. - 31 July
OBS10	40.8343517	28.2122183	720	15 Apr. - 31 July
KOERI03	40.884783	27.975100	1204	permanent
KOERI04	40.828184	27.535460	1144	permanent

Where: OBS1 to OBS10 are the temporary OBS stations of Ifremer, during the 2011 recording period and KOERI-03 and KOERI-04:are the permanent OBS stations of KOERI used here

Table 2

Table 2: Table of coordinates and operation period of the temporary OBS stations of data-set 2.

OBS code	Latitude (°N)	Longitude (°E)	Depth (m)	Recording period
OBS1	40.91677	27.764366	443	19 Sep. - 14 Nov.
OBS2	40.81528	27.7769	661	19 Sep. - 21 Sep.
OBS3	40.71292	27.787066	481	19 Sep. - 14 Nov.
OBS4	40.81267	27.7717	665	19 Sep. - 14 Nov.
OBS5	40.77940	27.848133	918	19 Sep. - 14 Nov.
OBS6	40.83143	27.947	1191	19 Sep. - 14 Nov.
OBS7	40.77620	27.708516	598	19 Sep. - 14 Nov.
OBS8	40.85125	27.708	1024	19 Sep. - 14 Nov.
OBS9	40.81977	27.60506	1106	19 Sep. - 14 Nov.
OBS10	40.84997	27.845516	401	19 Sep. - 23 Oct.
OBS11	40.812946	27.768004	658	01 Nov. -14 Nov.
OBS12	40.813015	27.768516	657	01 Nov. -14 Nov.
OBS13	40.795116	27.83906	1016	06 Oct. 2013- 14 Nov. 2014

Where: OBS1 to OBS12 are the temporary OBS stations of Ifremer, and OBS13 is the temporary OBS station of INGV, during the 2014 recording period

Table 3

Table 3: Results for synthetic tests on the 1D-models and the 3D velocity model of this study, for Trials 1 and 2.

Velocity models	Trial 1			Trial 2		
	Latitude 1 (°)	**Longitude 1 (°)**	**Depth 1 (km)**	**Latitude 2 (°)**	**Longitude 2 (°)**	**Depth 2 (km)**
Initial location	40.80	28.00	12	40.80	28.00	2
1D – this study	40.7677	28.0008	15.2	40.7627	27.996	11.2
1D – (Karabulut *et al.*, 2011)	40.7674	27.995	21.5	40.7611	27.9918	17.4
3D-this study	40.7985	27.9956	10.75	40.7965	27.9997	2.09

Table 4

Table 4: Location results for triplet of case study 1.

Case study 1				Velocity Models								
				1D – this study			3D – this study			3D – (Yamamoto, *et al.*, 2017)		
No	**Date-Time**	**OBS used**	**Ml**	**Lat (°)**	**Long (°)**	**Depth bsf (km)**	**Lat (°)**	**Long (°)**	**Depth bsf (km)**	**Lat (°)**	**Long (°)**	**Depth bsl (km)**
1	25 October 2014 01:46:52	01, 04, 05, 07, 13	1.50	40.8080	27.8032	10.77	40.8452	27.8120	6.21	40.8174	27.7668	18.62
2	25 October 2014 03:05:00	03, 04, 05, 06, 07, 08, 13	1.93	40.8036	27.7999	9.61	40.8484	27.8104	6.29	40.8171	27.7691	18.38
3	25 October 2014 04:21:38	01, 03, 04, 05, 07	1.54	40.8035	27.8039	10.52	40.8421	27.8096	6.59	40.8152	27.7667	18.61

Table 5

Table 5: Location results for triplet of case study 2.

Case study 2				Velocity Models					
				1D – this study			3D – this study		
No	**Date-Time**	**OBS used**	**Ml**	**Lat (°)**	**Long (°)**	**Depth bsf (km)**	**Lat (°)**	**Long (°)**	**Depth bsf (km)**
1	19 May 2011 04:44:05	01, 02, 05, 06, 07, 08, 09, 10	1.15	40.8159	28.0985	2.71	40.8277	28.1154	0.003
2	19 May 2011 05:05:38	07, 08,10, 09	0.54	40.8377	28.0958	15.65	40.8340	28.1246	1.46
3	23 June 2011 20:25:11	07, 08,10, 09	0.93	40.8558	28.1189	19.64	40.8361	28.1303	0.7

Where the relocation was obtained by the two velocity models (1D versus 3D).

Table 6

Table 6: Comparison of the synthetic P and S arrivals for triplet of case study 2 with the real data.

Case study 2				
Station	**Synthetic ts-tp (s)**			**Real data ts-tp (s)**
	Earthquake 1	**Earthquake 2**	**Earthquake 3**	
OBS07	3.5	3.2	3.6	4.0
OBS08	3.2	2.6	2.9	3.0
OBS09	4.1	3.7	4.0	3.9
OBS10	3.8	3.0	3.1	3.4

Table 7: Comparison of the 3D location results for triplet of case study 2 with the synthetic test.

Case study 2						
No	**Synthetic Location**			**Real data location with 3D model**		
	Lat (°)	**Long (°)**	**Depth bsf (km)**	**Lat (°)**	**Long (°)**	**Depth bsf (km)**
1	40.8327	28.1152	0.057	40.8277	28.1154	0.003
2	40.838	28.1258	0.96	40.8340	28.1246	1.46
3	40.84	28.1318	0.34	40.8361	28.1303	0.7

Table 8

Table 8: Location results for the 10-events cluster of case study 3.

Case study 3				Velocity Models					
				1D – this study			3D – this study		
No	**Date-Time**	**OBS used**	**Ml**	**Lat (°)**	**Long (°)**	**Depth bsf (km)**	**Lat (°)**	**Long (°)**	**Depth bsf (km)**
1	26 April 2011 16:12:09	02, 05, 06, 07, 08, 09, 10	0.98	40.7998	27.9829	12.09	40.8197	27.9867	11.89
2	07 May 2011 04:14:26	01, 02, 03, 05, 06, 07, 08, 09, 10	1.40	40.8042	27.9827	14.49	40.8256	27.9889	14.77
3	07 May 2011 17:27:49	01, 02, 03, 05, 06, 07, 08, 09, 10	2.16	40.8092	27.9763	14.05	40.8299	27.9819	13.89
4	07 May 2011 17:46:15	02, 05, 06, 07, 08, 09, 10	1.51	40.8021	27.9860	12.55	40.8220	27.9903	12.36
5	09 May 2011 14:00:02	02, 03, 05, 06, 07, 08, 09	1.51	40.7971	27.9895	12.60	40.8173	27.9945	12.48
6	09 May 2011 23:08:07	01, 02, 03, 04, 05, 06, 07, 08, 09, 10	1.71	40.7946	27.9797	13.25	40.8165	27.9851	13.37
7	12 May 2011 14:32:44	01, 02, 03, 05, 06, 07, 08, 09, 10	1.71	40.7995	27.9797	13.49	40.8207	27.9854	13.63
8	13 May 2011 10:40:02	01, 02, 03, 05, 06, 07, 08, 09, 10	2.00	40.8020	27.9830	13.26	40.8226	27.9890	13.19
9	17 May 2011 20:40:14	02, 05, 06, 07, 08, 09, 10	1.18	40.7999	27.9795	12.23	40.8202	27.9837	12.08
10	18 May 2011 03:17:00	01, 02, 03, 05, 06, 07, 08, 09, 10	1.77	40.8093	27.9796	13.76	40.8294	27.9857	13.60

Where the relocation was obtained by the two velocity models (1D versus 3D).

Table 9

Table 9: Common events used for comparison of locations from for this study (2014 period) and from (*Yamamoto's et al.*, 2017) and displayed in Figure 15.

		This study				(Yamamoto *et al.*, 2017)			
No	**Date-Time (2014)**	**Latitude (°)**	**Longitude (°)**	**Depth (km)**	**Mag**	**Latitude (°)**	**Longitude (°)**	**Depth (km)**	**Mag**
1	26 September 06:02:55	40.8309	27.7308	5.25	0.9	40.8091	27.6466	15.46	1.7
2	01 October 14:44:49	40.8509	27.8905	3.55	0.7	40.8710	27.9218	10.00	1.3
3	03 October 21:40:22	40.8340	27.8769	5.59	0.7	40.8497	27.9223	18.2	1.7
4	04 October 11:58:34	40.8243	27.7265	7.00	1.9	40.8247	27.6696	14.54	2.2
5	17 October 19:52:52	40.8295	27.8642	4.90	0.8	40.8041	27.8832	13.54	1.4
6	18 October 10:17:43	40.8471	27.8087	6.61	1.1	40.8310	27.8056	21.07	1.9
7	24 October 14:18:24	40.8356	27.7383	5.41	0.7	40.8241	27.6531	14.89	1.4
8	25 October 01:46:52	40.8452	27.812	6.21	0.9	40.8174	27.7668	18.62	1.5
09	25 October 03:05:00	40.8484	27.8104	6.29	1.7	40.8171	27.7691	18.38	1.9
10	25 October 04:21:38	40.8421	27.8096	6.59	0.9	40.8152	27.7667	18.61	1.5
11	25 October 09:28:57	40.8242	27.7754	5.22	0.5	40.8165	27.7706	18.19	1.6
12	26 October 03:21:34	40.8303	27.7331	5.19	0.9	40.8089	27.6489	15.46	1.6
13	26 October 07:41:51	40.8463	27.7379	6.68	0.7	40.8236	27.6907	20.28	2.0
14	27 October 21:22:10	40.8240	27.8023	4.59	0.7	40.8134	27.6734	20.52	1.4

Table 10: Single (for M>3) and composite (for M<2) focal mechanisms solutions for selected earthquakes from the two data-sets.

No	**Number of events used**	**Date-Time**	**Lat (°N)**	**Long (°E)**	**Depth (km) below seafloor**	**M_l**	**Strike(°)**	**Dip (°)**	**Rake (°)**
S1	1	01 May 2011 08:36	40.8266	28.1355	14.2	3.3	312	63	135
S2	1	19 May 2011 04:38	40.8340	28.1442	4.3	3.1	70	20	-125
S3	1	25 July 2011 17:57	40.82	27.741	11.5	5.1	113	83	-148
S4	1	19 Sept 2014 10:52	40.837	27.8722	4.4	3.3	97	20	-86
C1	10	Aftershock Sequence See supplementary Information	40.82	27.75	2.5	1.2	300	34	-145
C2	10	See Case Study 3	40.82	27.98	13.1	1.5	78	58	151
C3	3	See Case Study 2	40.83	28.12	0.7	1.5	233	67	101
C4	3	See Case Study 1	40.84	27.81	6.4	1.65	190	59	-80

Where S1 to S4 and C1 to C4 correspond to single and composite focal mechanisms respectively.

Figure 1a

Click here to download Figure Figure1a.jpg

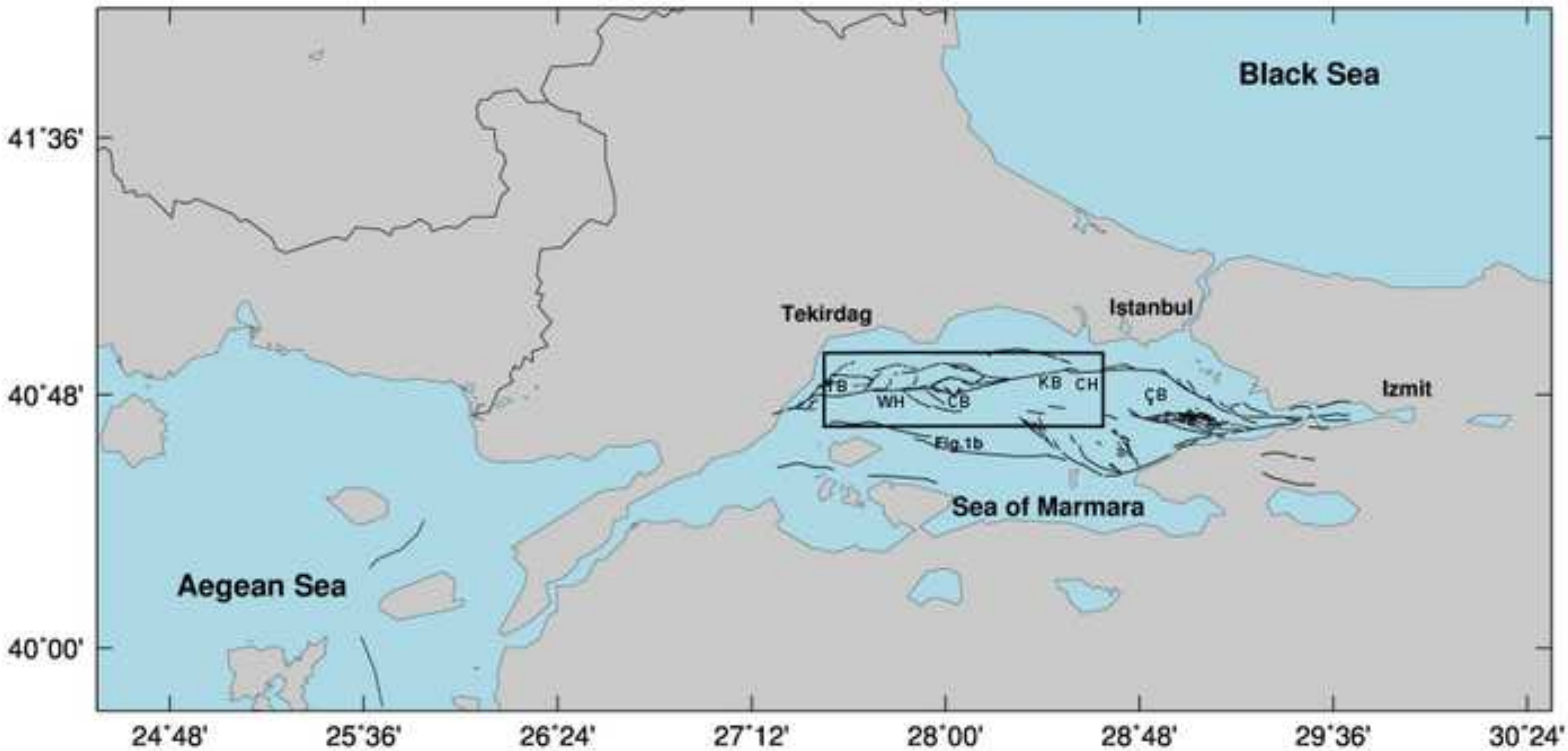

Figure 1b

Click here to download Figure Figure1b.jpg

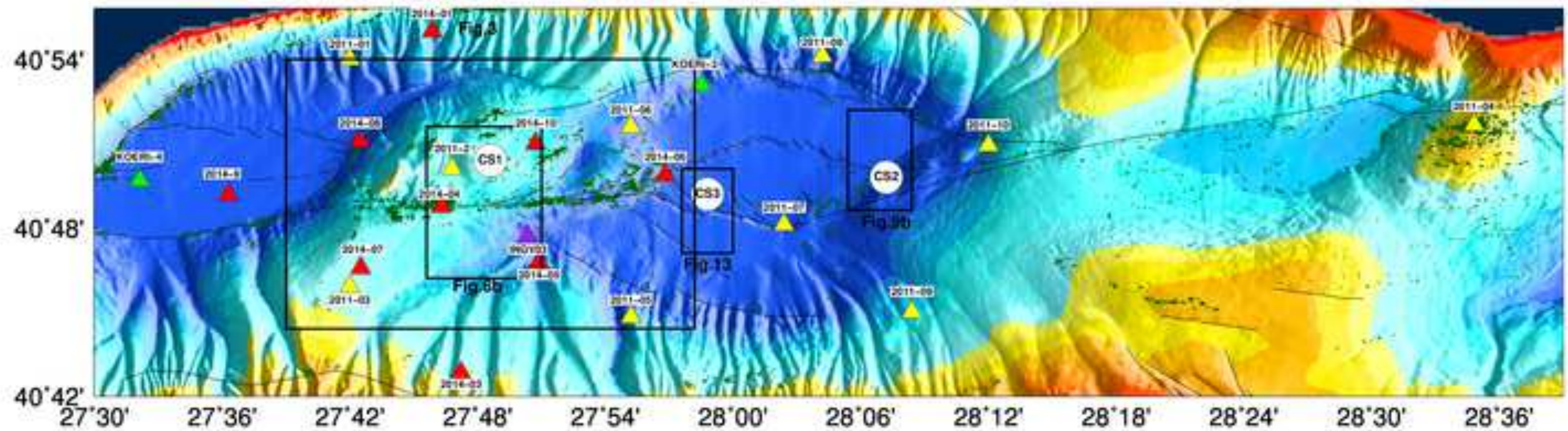

Figure 2a

Click here to download Figure Figure2a.jpg

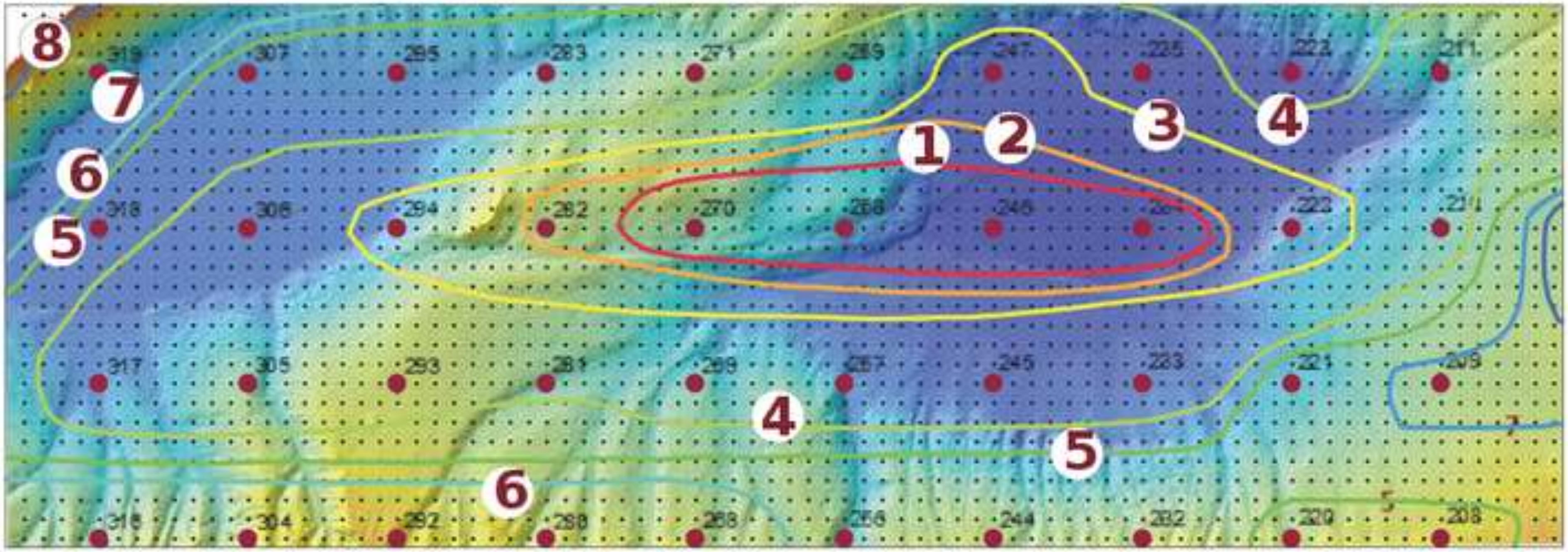

Figure 2b

Click here to download Figure Figure2b.jpeg

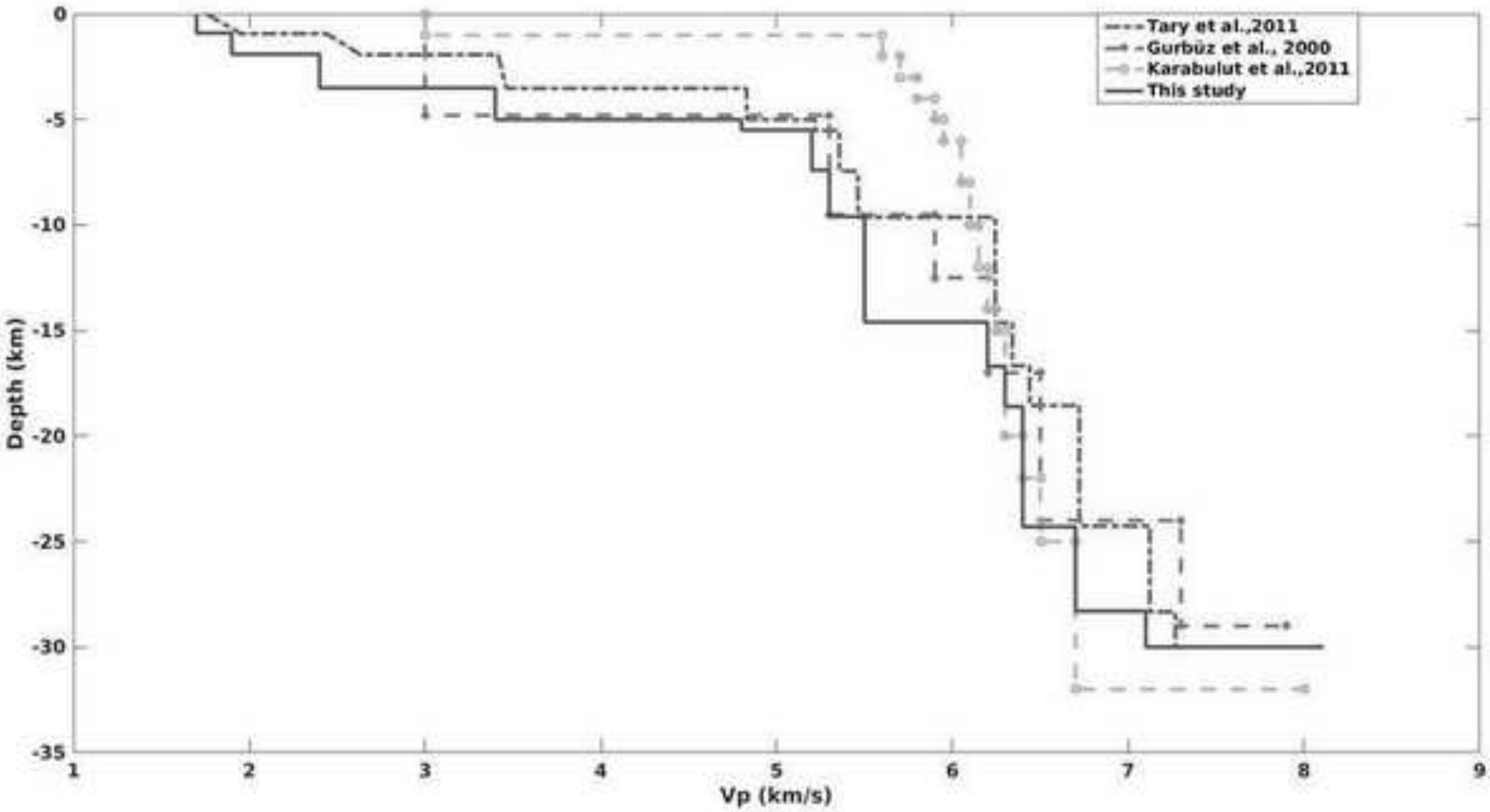

Figure 3

Click here to download Figure Figure3.jpg

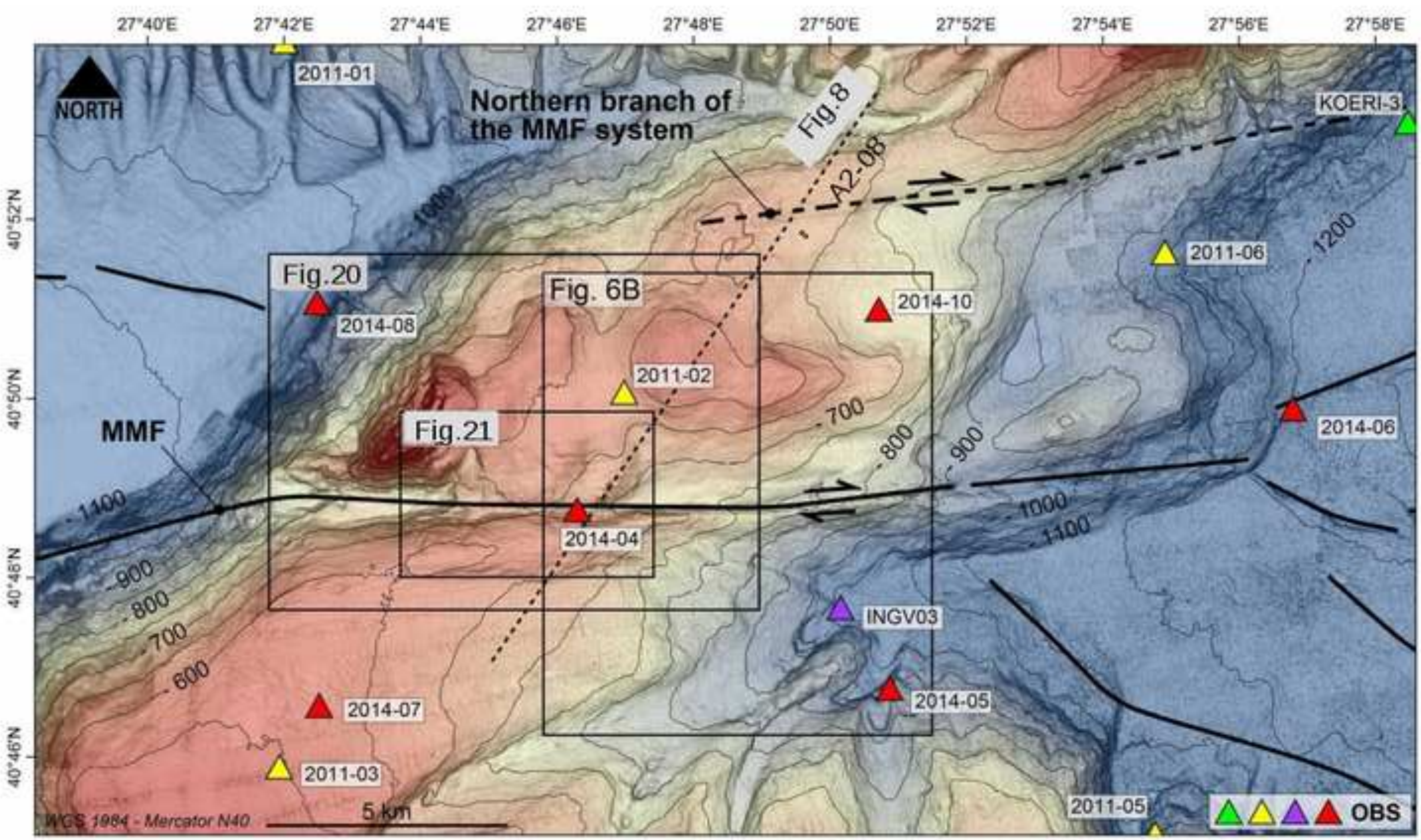

Figure 4

Click here to download Figure Figure4.jpeg

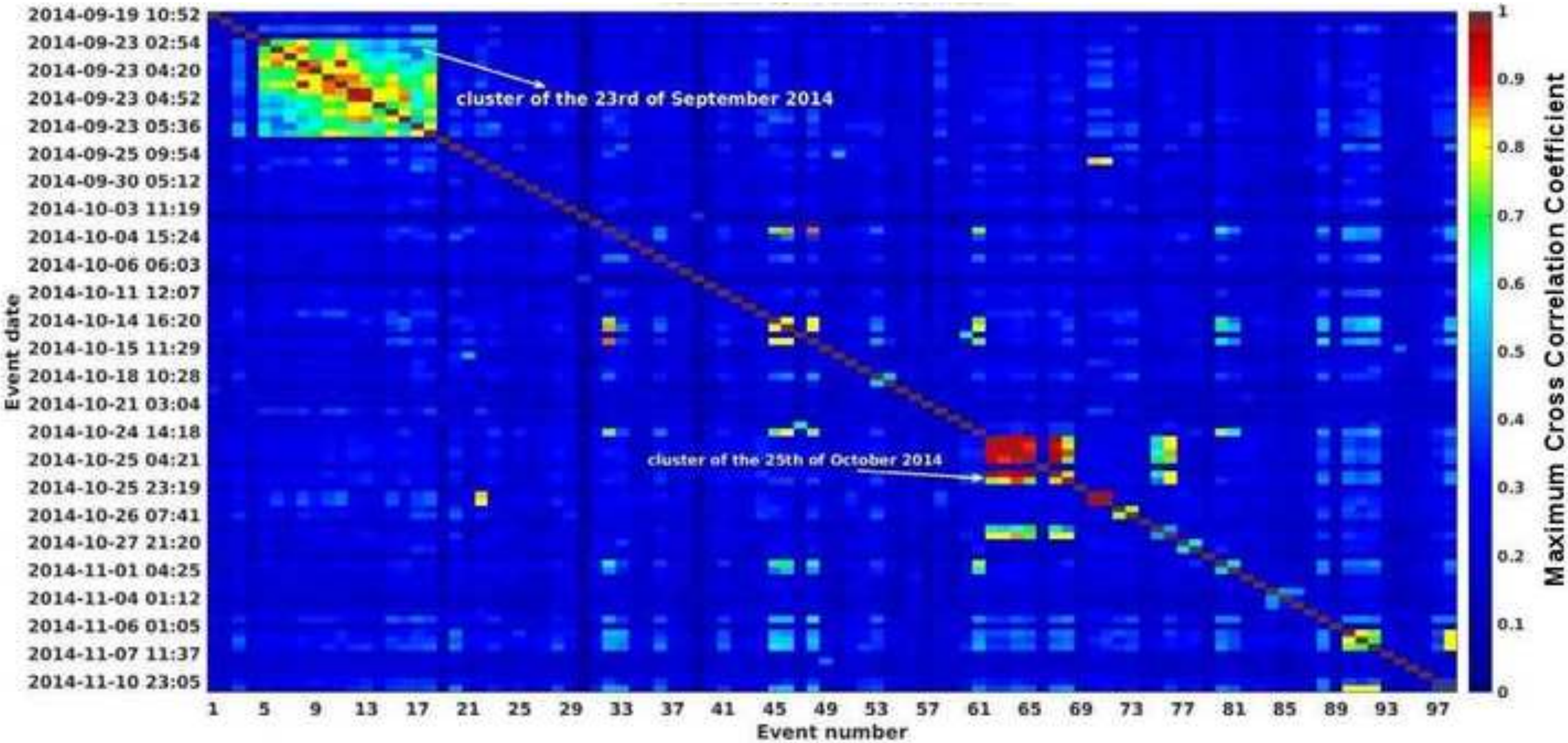

Figure 5

Click here to download Figure Figure5.jpg

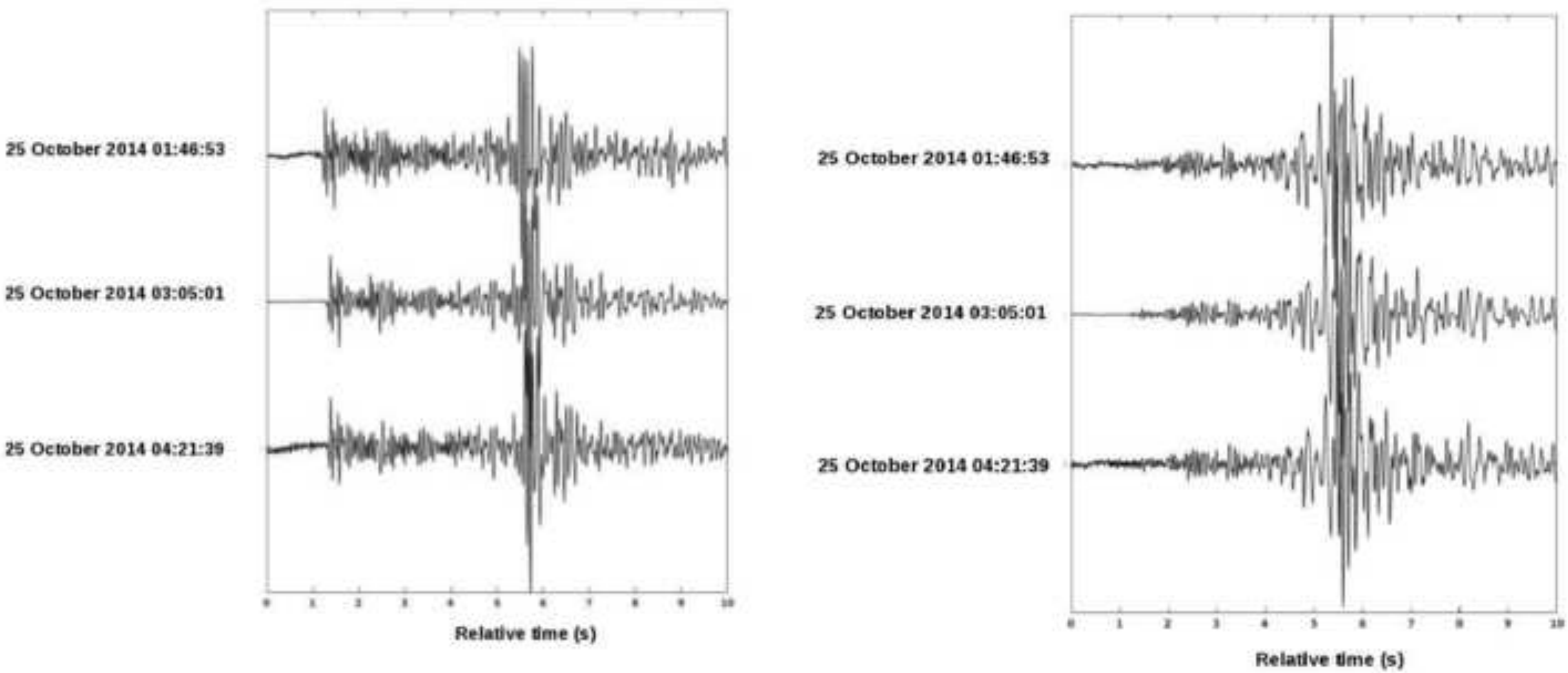

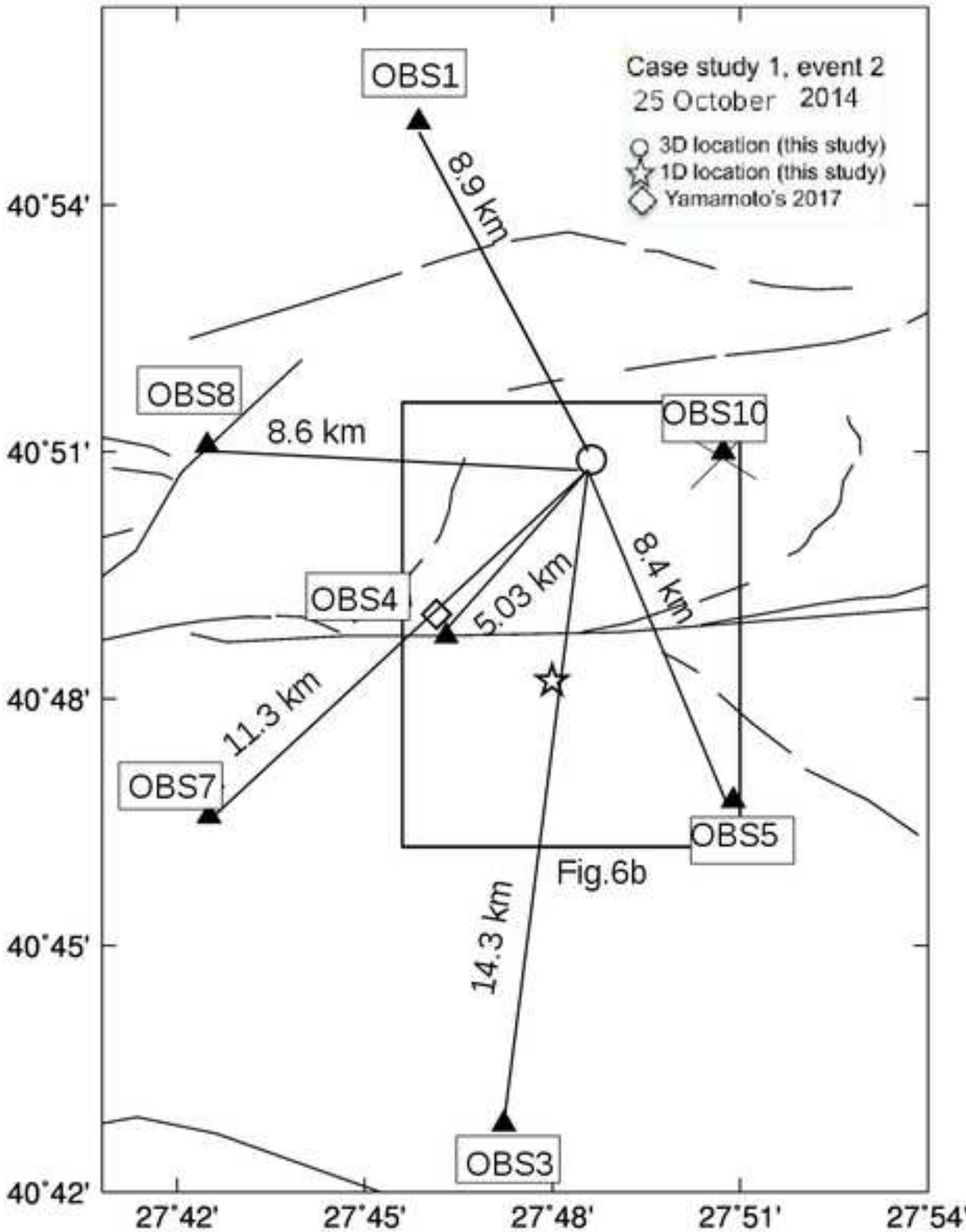

Case study 1, event 2
25 October 2014
3D location (this study)
1D location (this study)
Yamamoto's 2017
OBS1
OBS8
OBS10
OBS4
OBS7
OBS5
OBS3
8.9 km
8.6 km
5.03 km
8.4 km
11.3 km
14.3 km
Fig.6b
40°54'
40°51'
40°48'
40°45'
40°42'
27°42'
27°45'
27°48'
27°51'
27°54'

Figure 6b

Click here to download Figure Figure6b.jpg

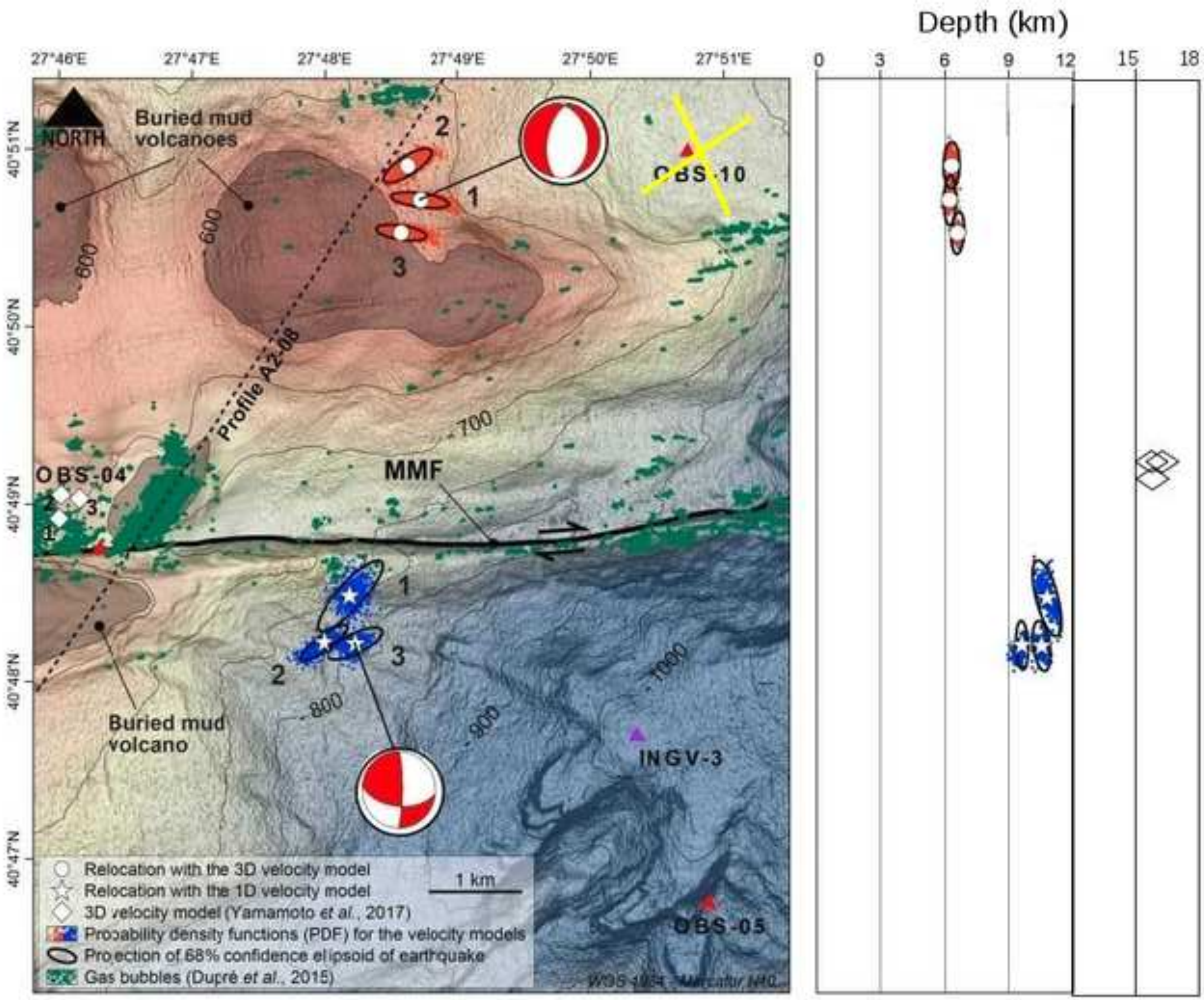

Figure 7

Click here to download Figure Figure7.jpg

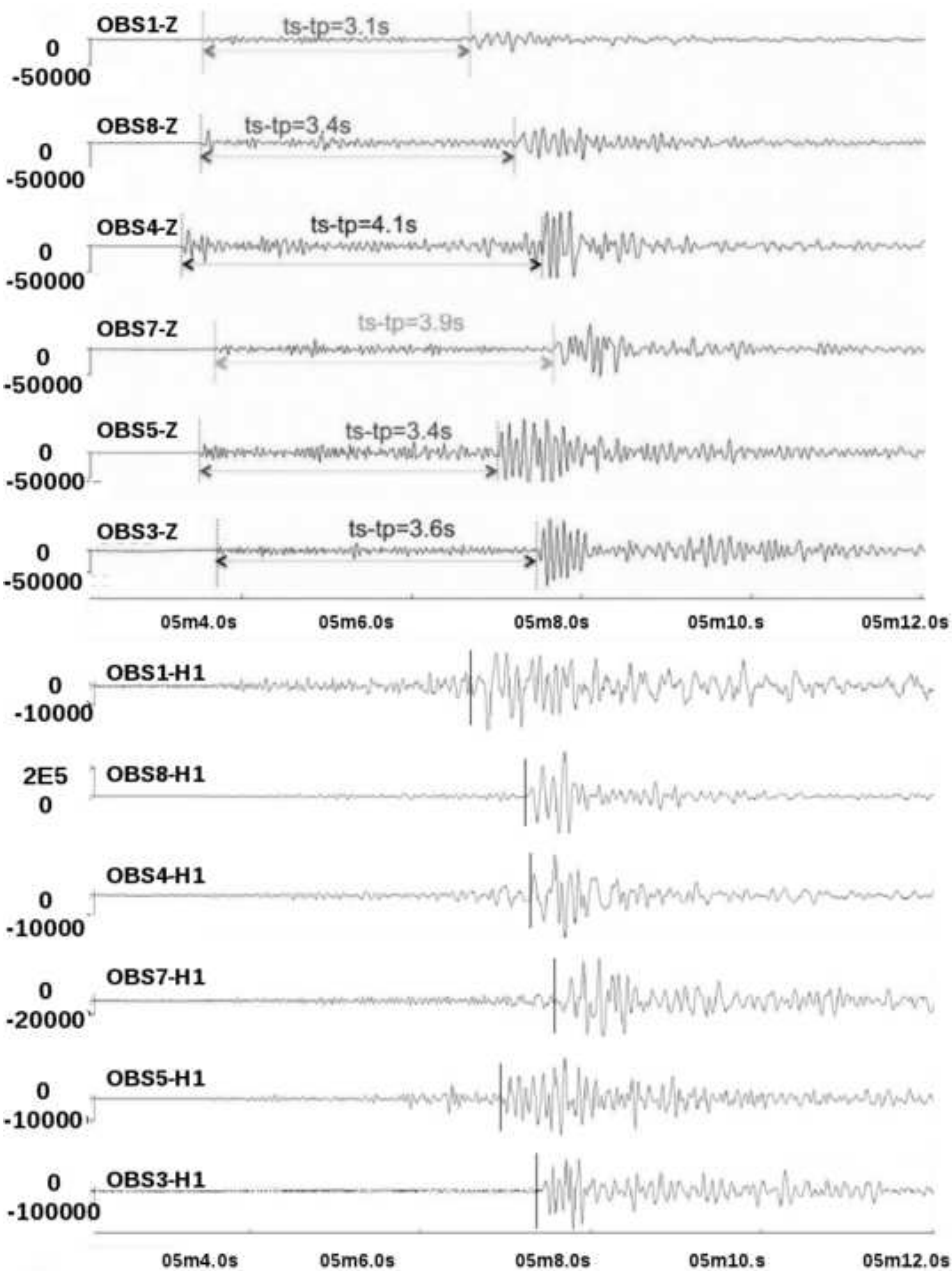

Figure 8

Click here to download Figure Figure8.jpg

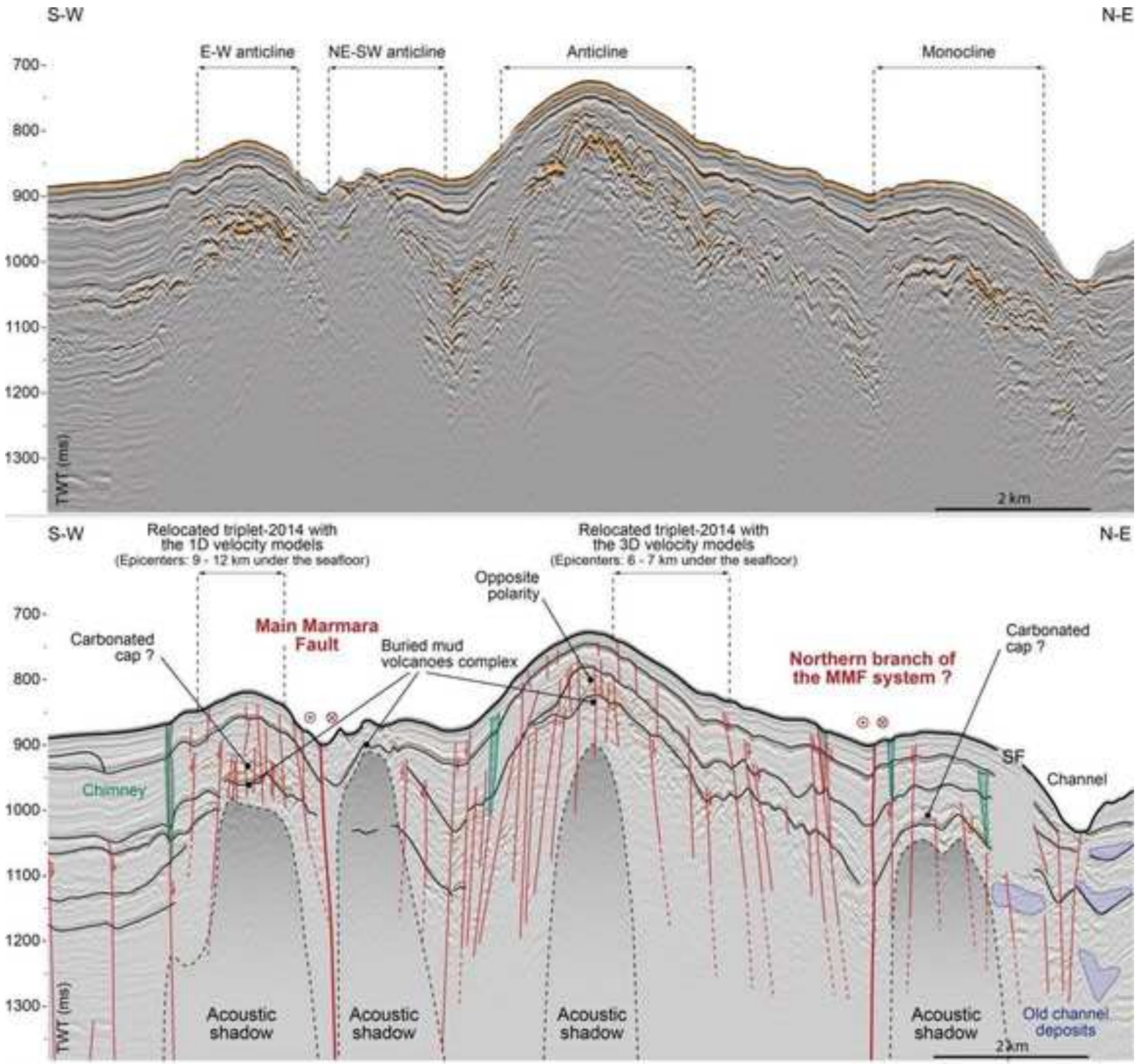

Figure 9a

Click here to download Figure Figure9a.jpg

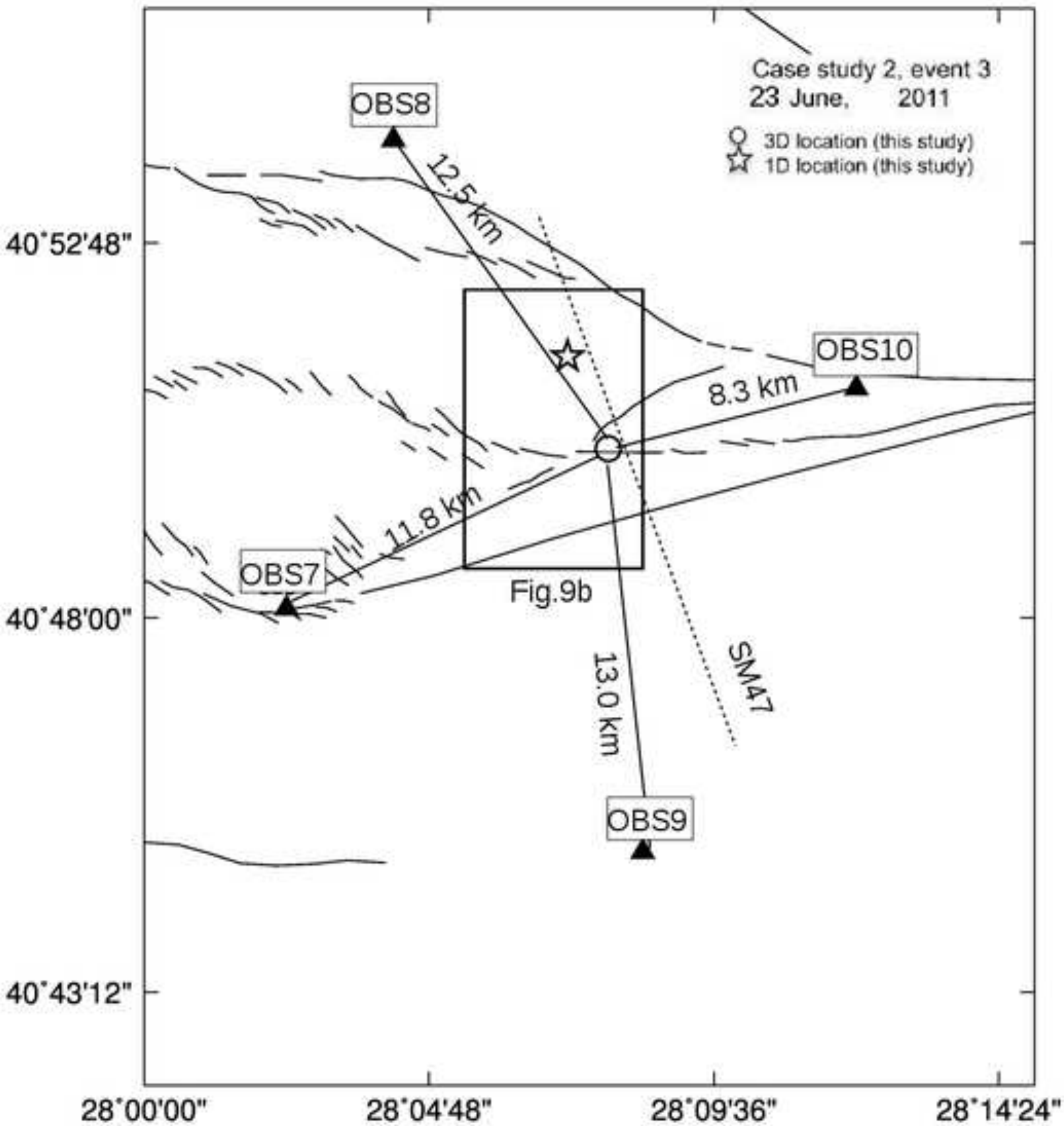

Figure 9b

Click here to download Figure Figure9b.jpg

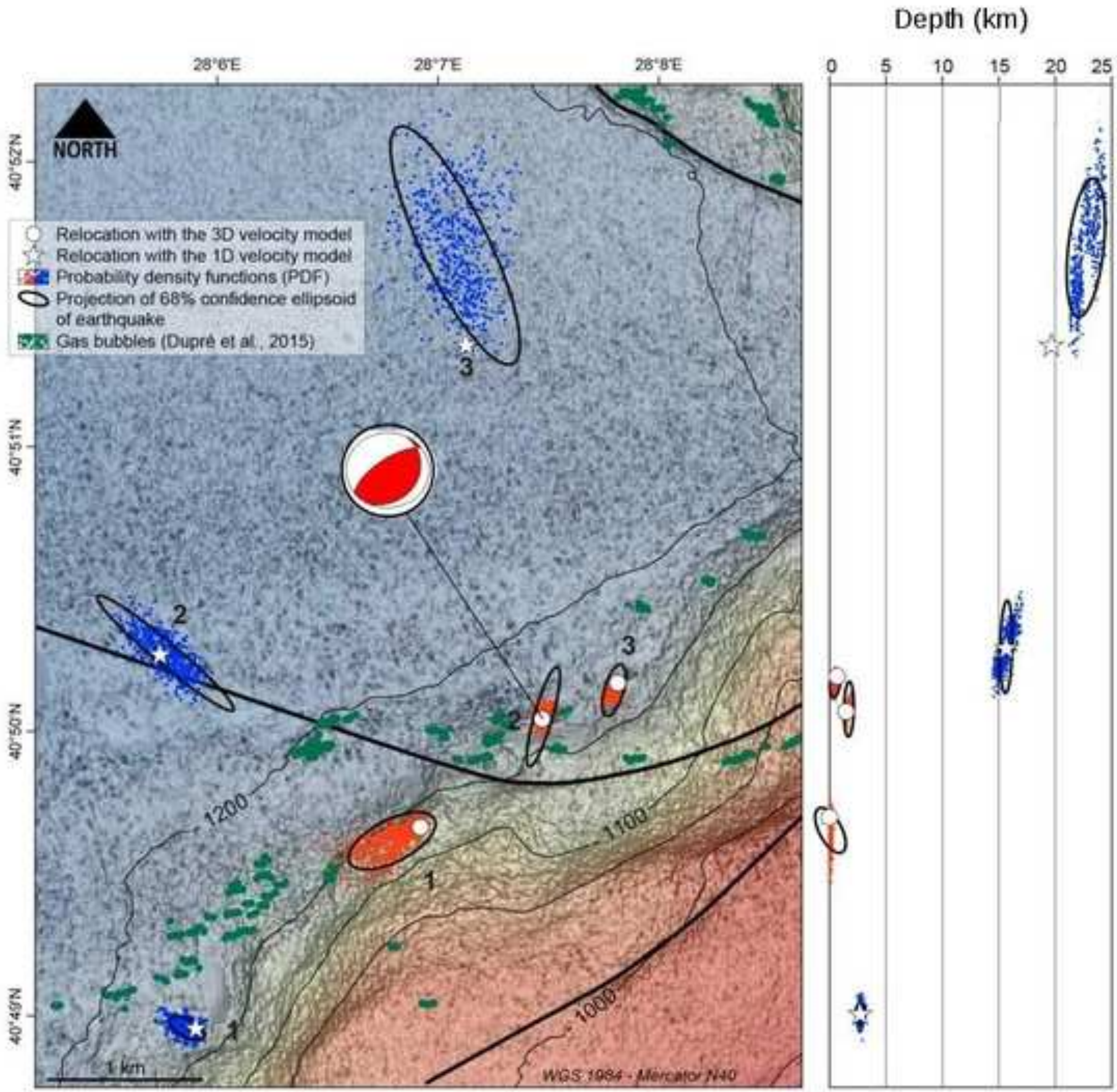

Figure 10

Click here to download Figure Figure10.jpg

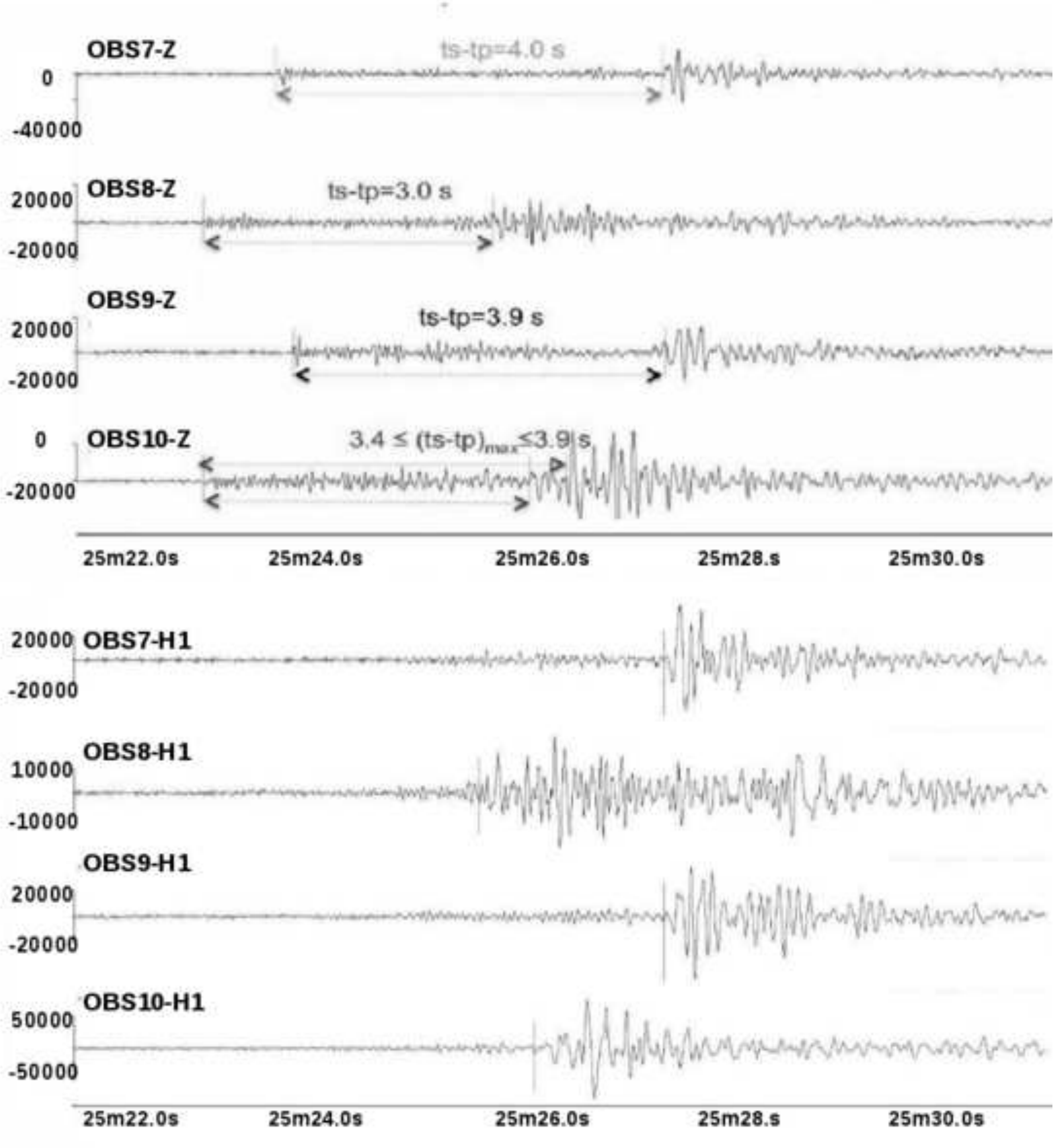

Figure 11

Click here to download Figure Figure11.jpg

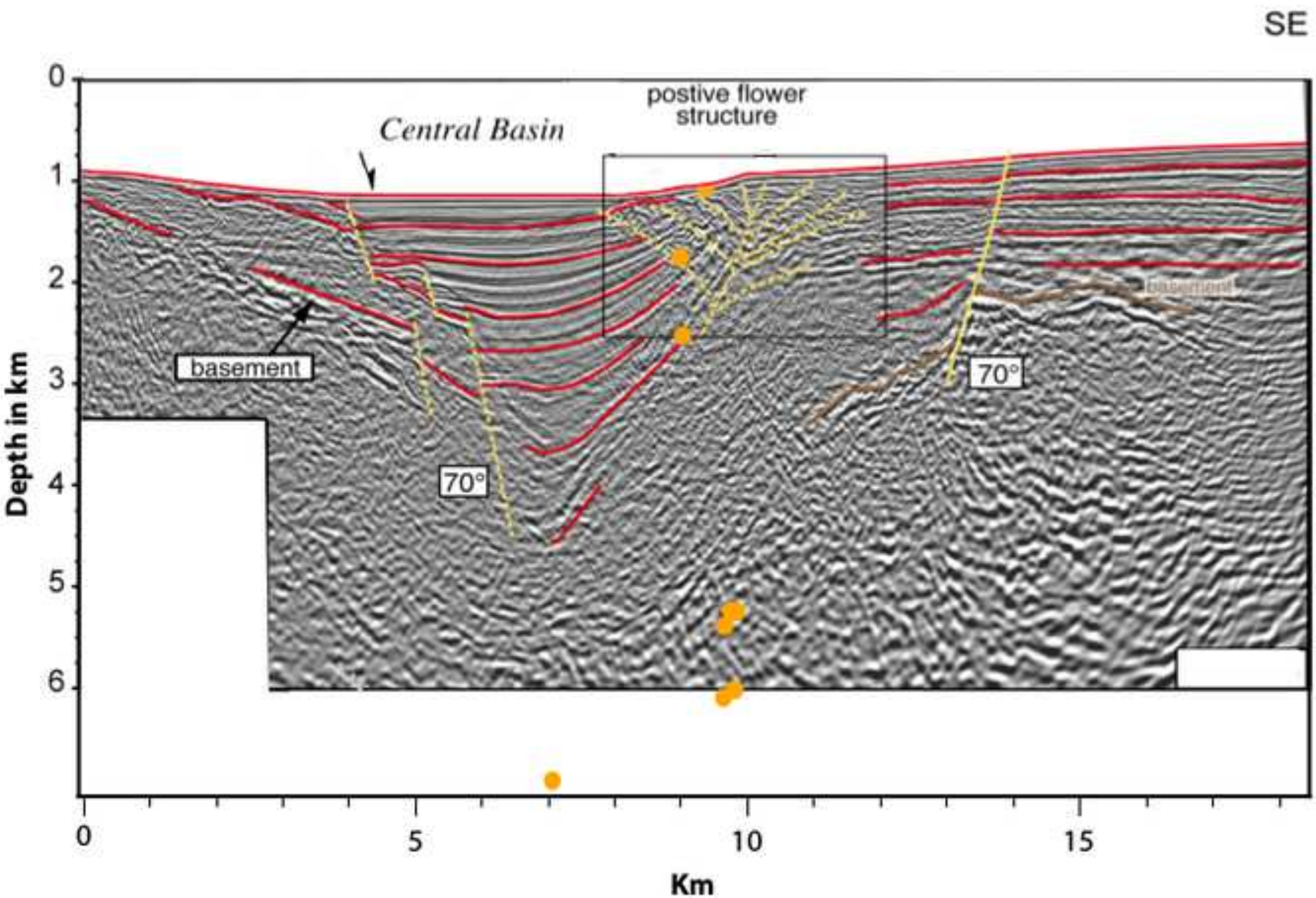

Figure 12

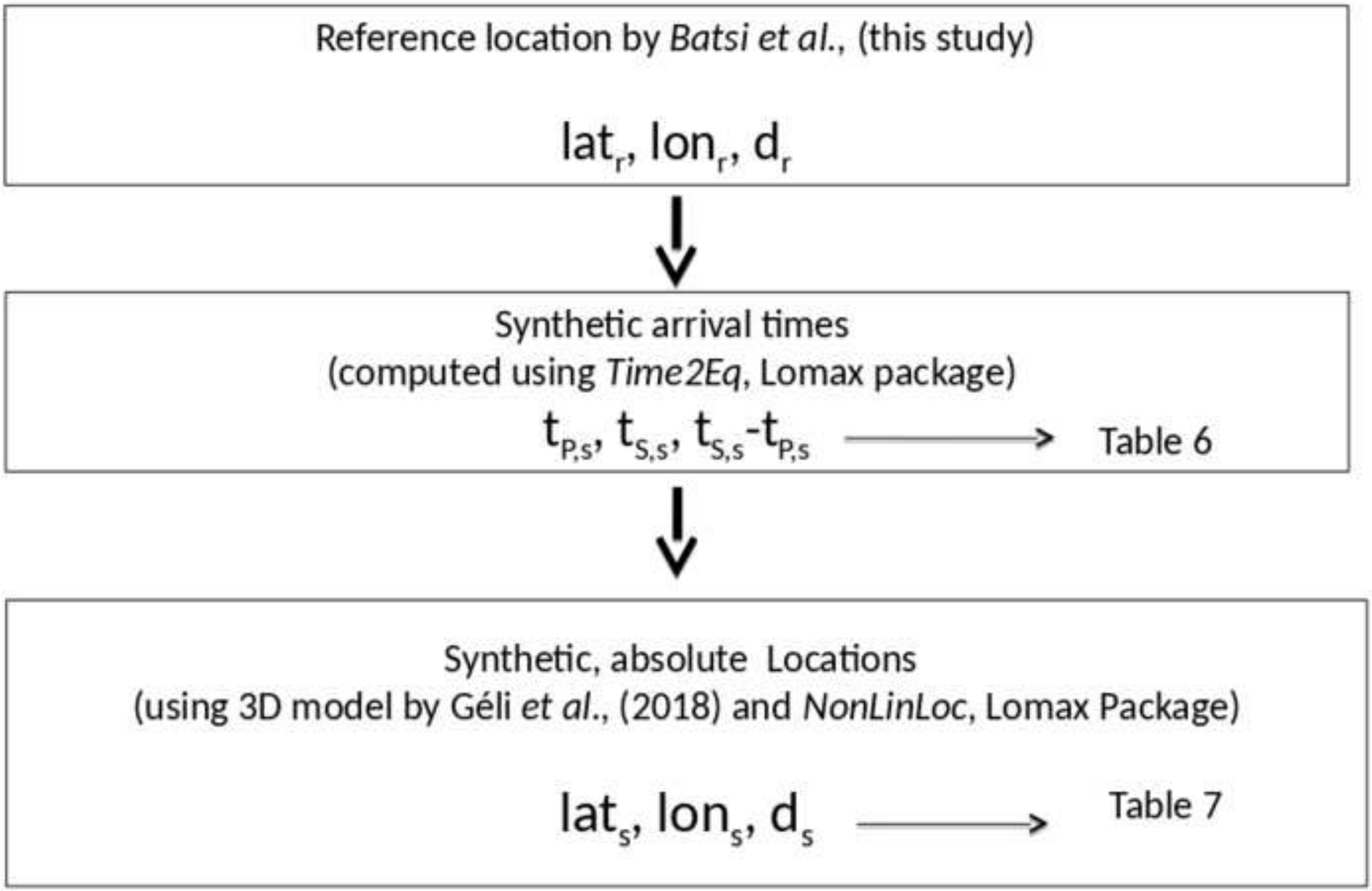
Reference location by *Batsi et al.*, (this study)
lat_r, lon_r, d_r
Synthetic arrival times
(computed using *Time2Eq*, Lomax package)
$t_{P,s}$, $t_{S,s}$, $t_{S,s}$-$t_{P,s}$
Table 6
Synthetic, absolute Locations
(using 3D model by Géli *et al*., (2018) and *NonLinLoc*, Lomax Package)
lat_s, lon_s, d_s
Table 7

Figure 13

Click here to download Figure Figure13.jpg

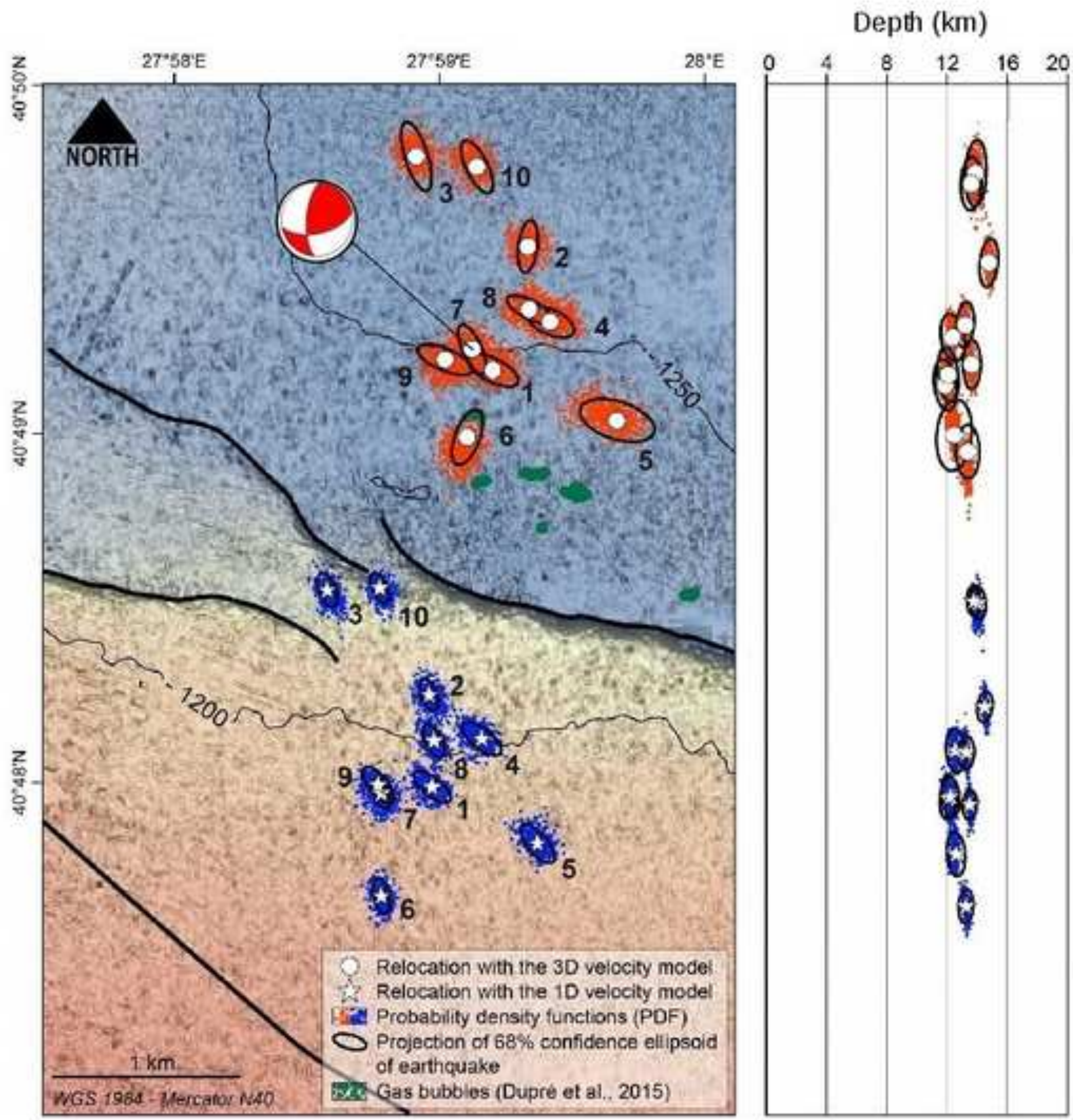

Figure 14

Click here to download Figure Figure14.jpg

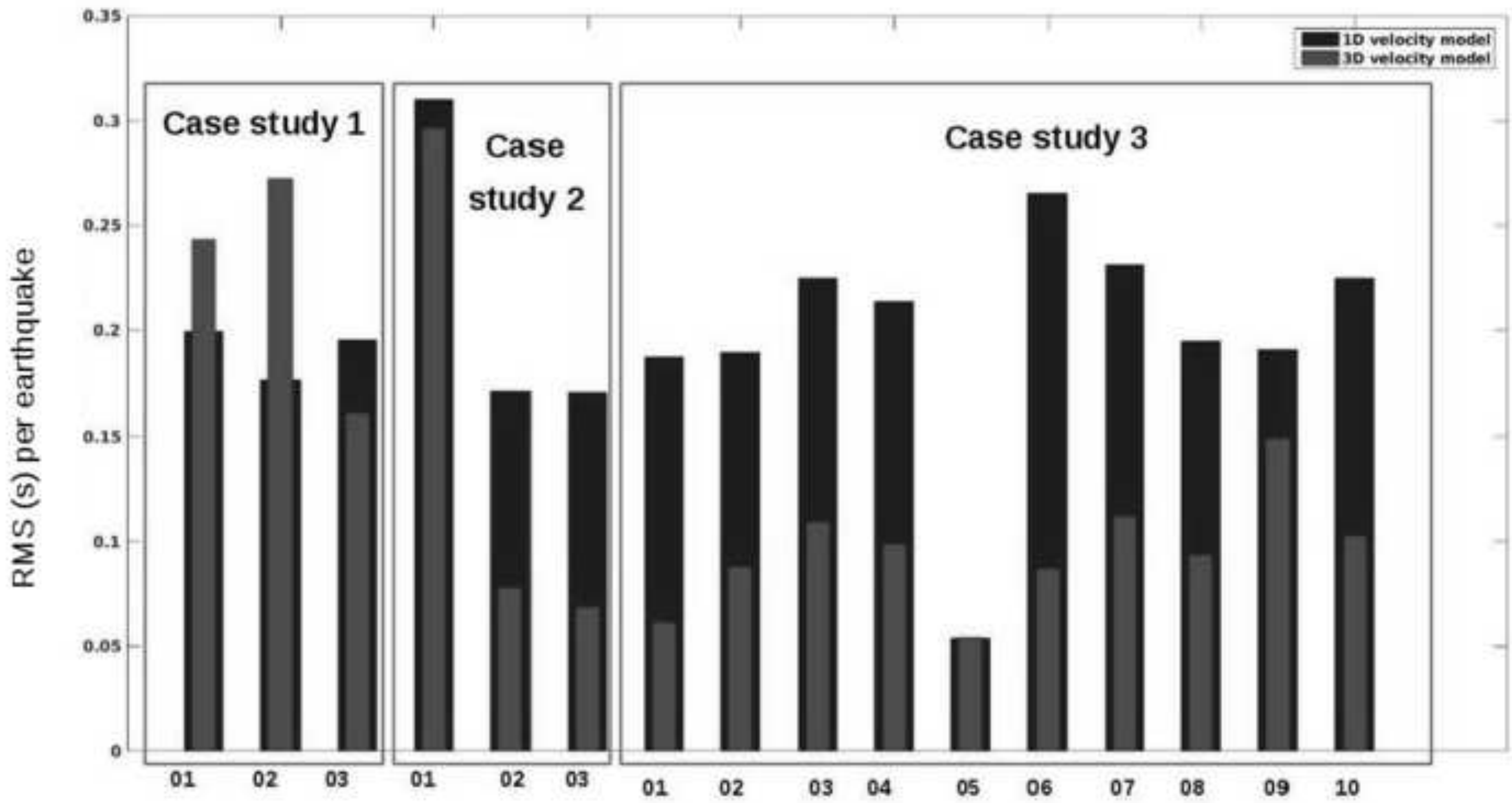

Figure 15

Click here to download Figure Figure15.jpg

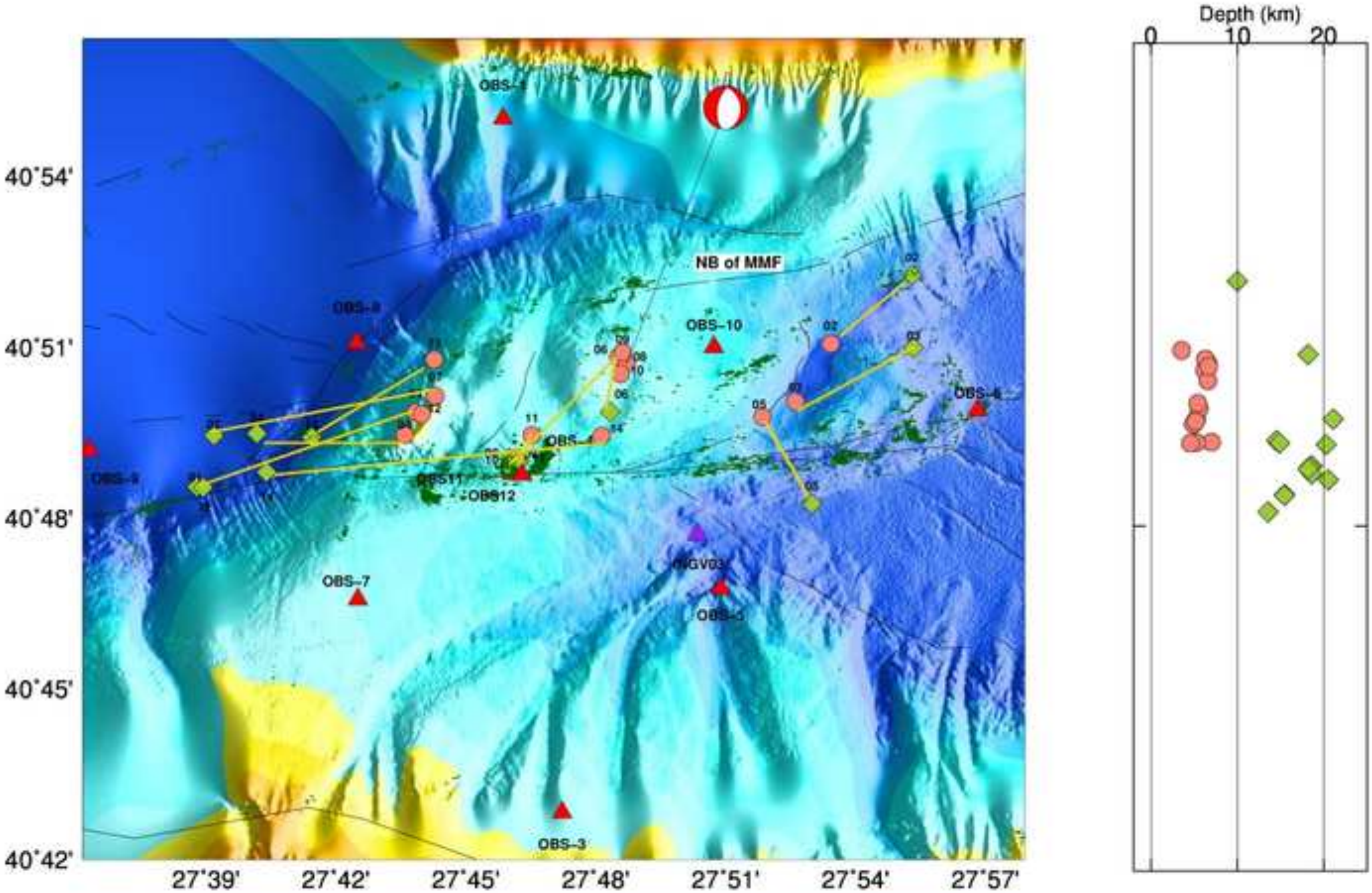

Figure 16 Click here to download Figure Figure16.jpeg

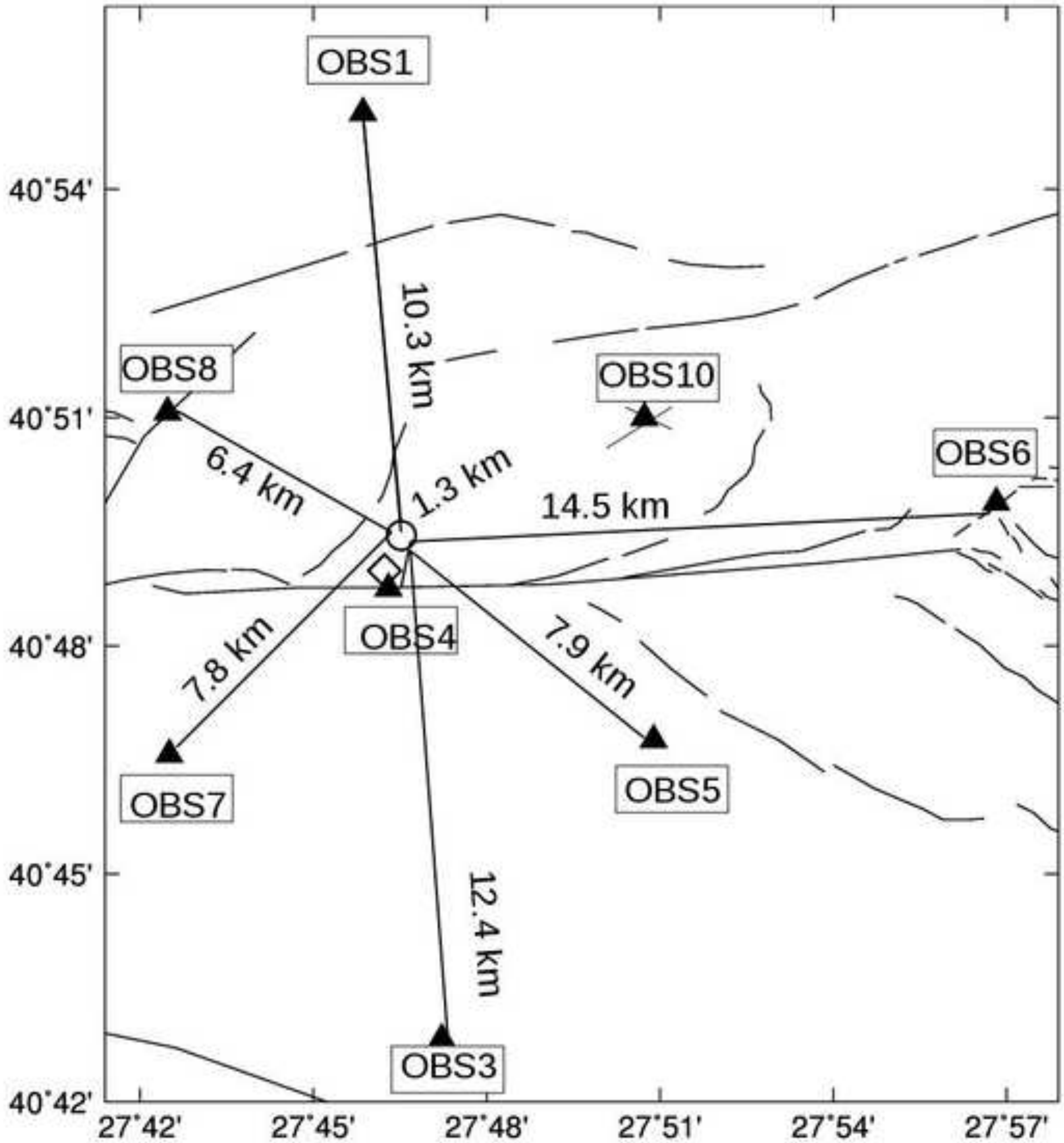

Figure 17

Click here to download Figure Figure17.jpg

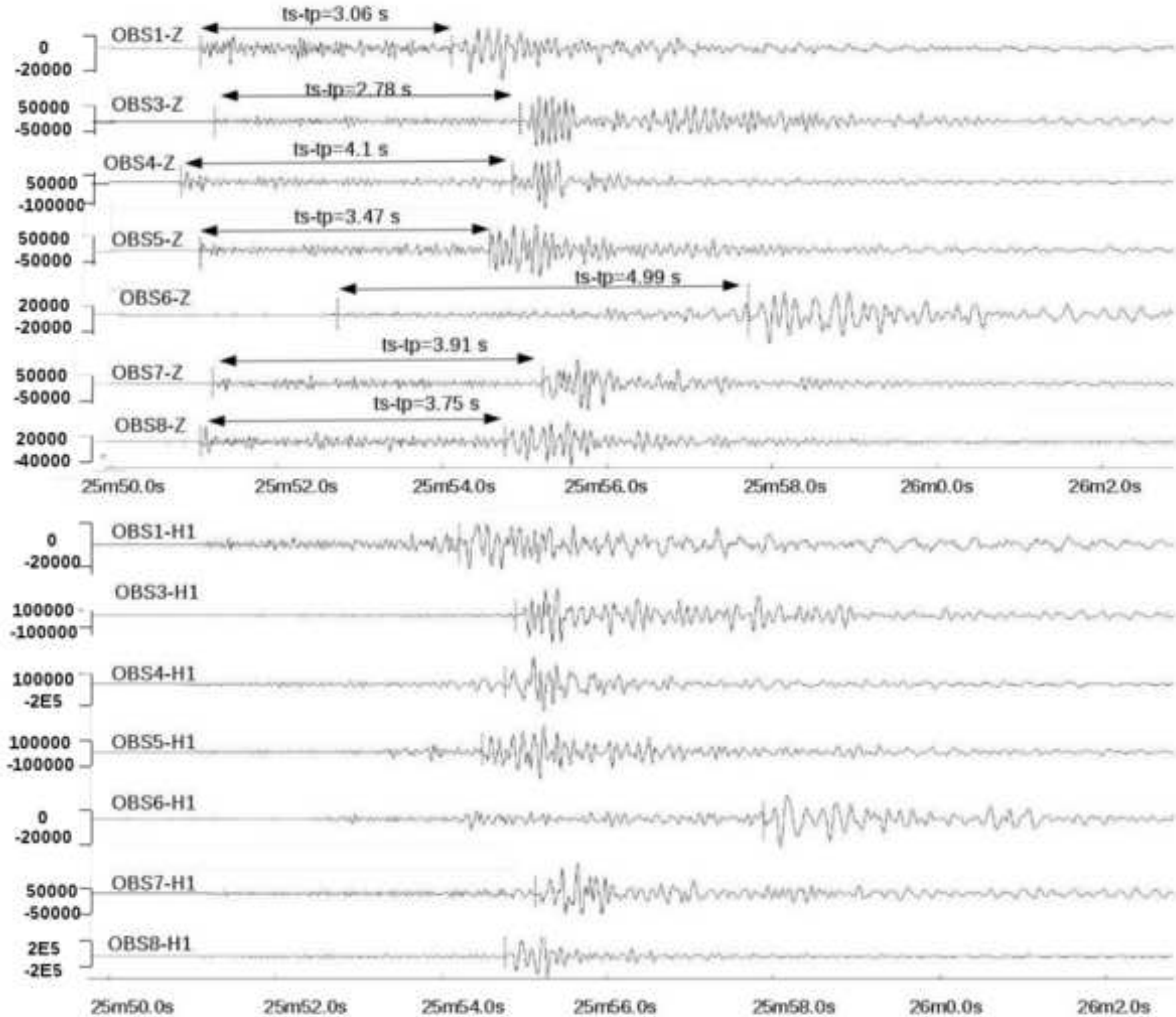

Figure 18 Click here to download Figure Figure18.jpg

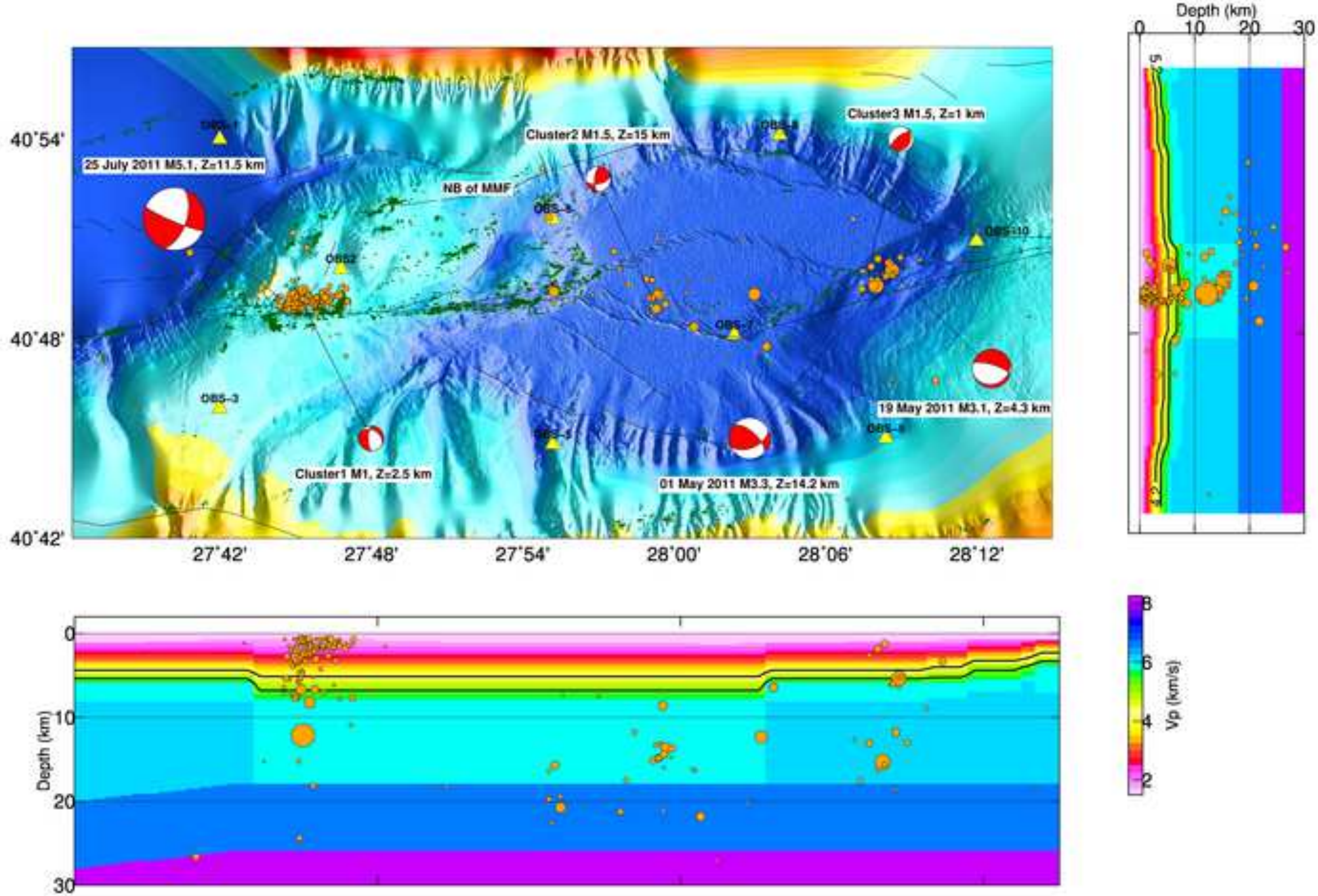

Figure 19

Click here to download Figure Figure19.jpg

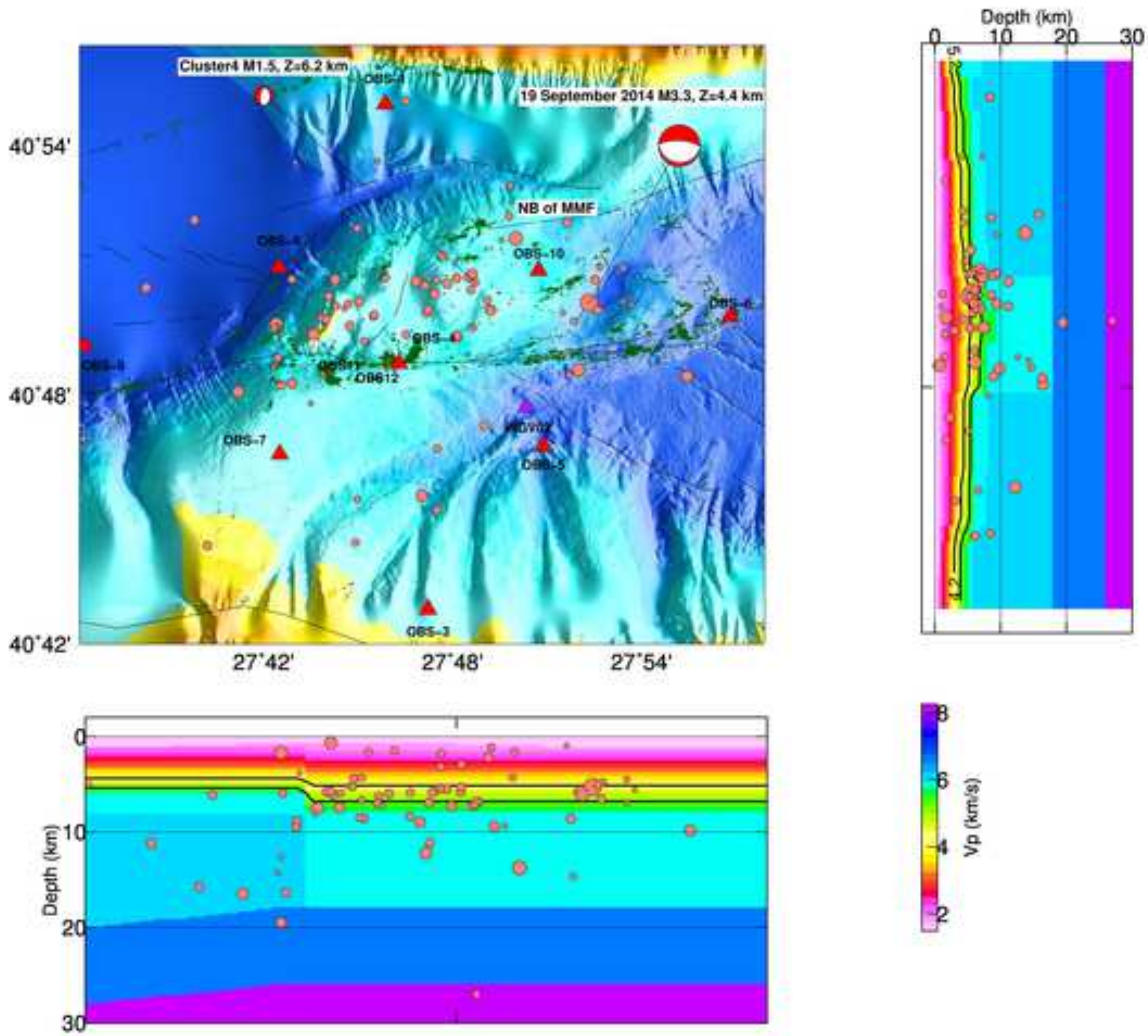

Figure 20 Click here to download Figure Figure20.jpeg

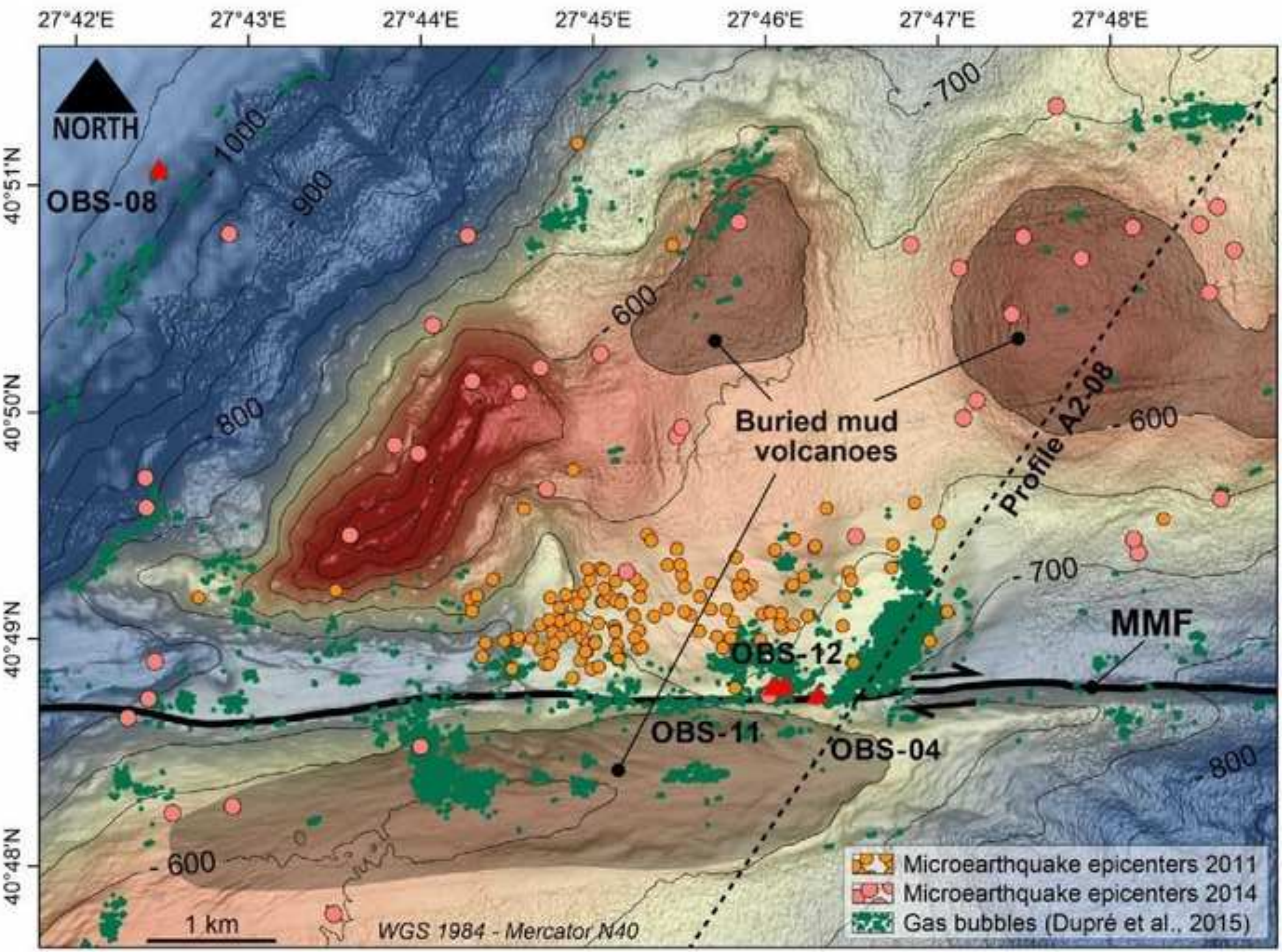

Figure 21

Click here to download Figure Figure21.jpeg

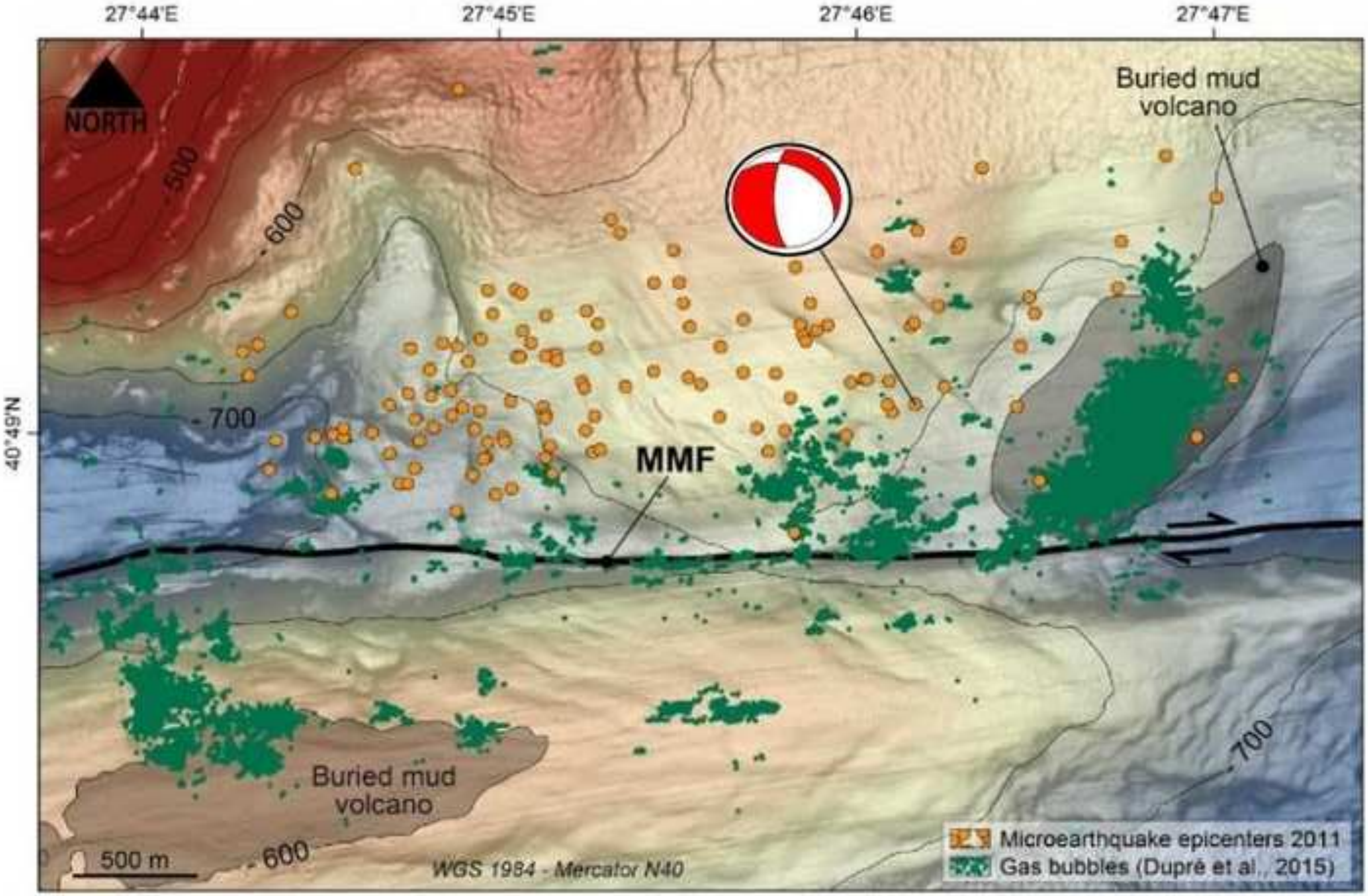

Figure 22

Click here to download Figure Figure22.jpg

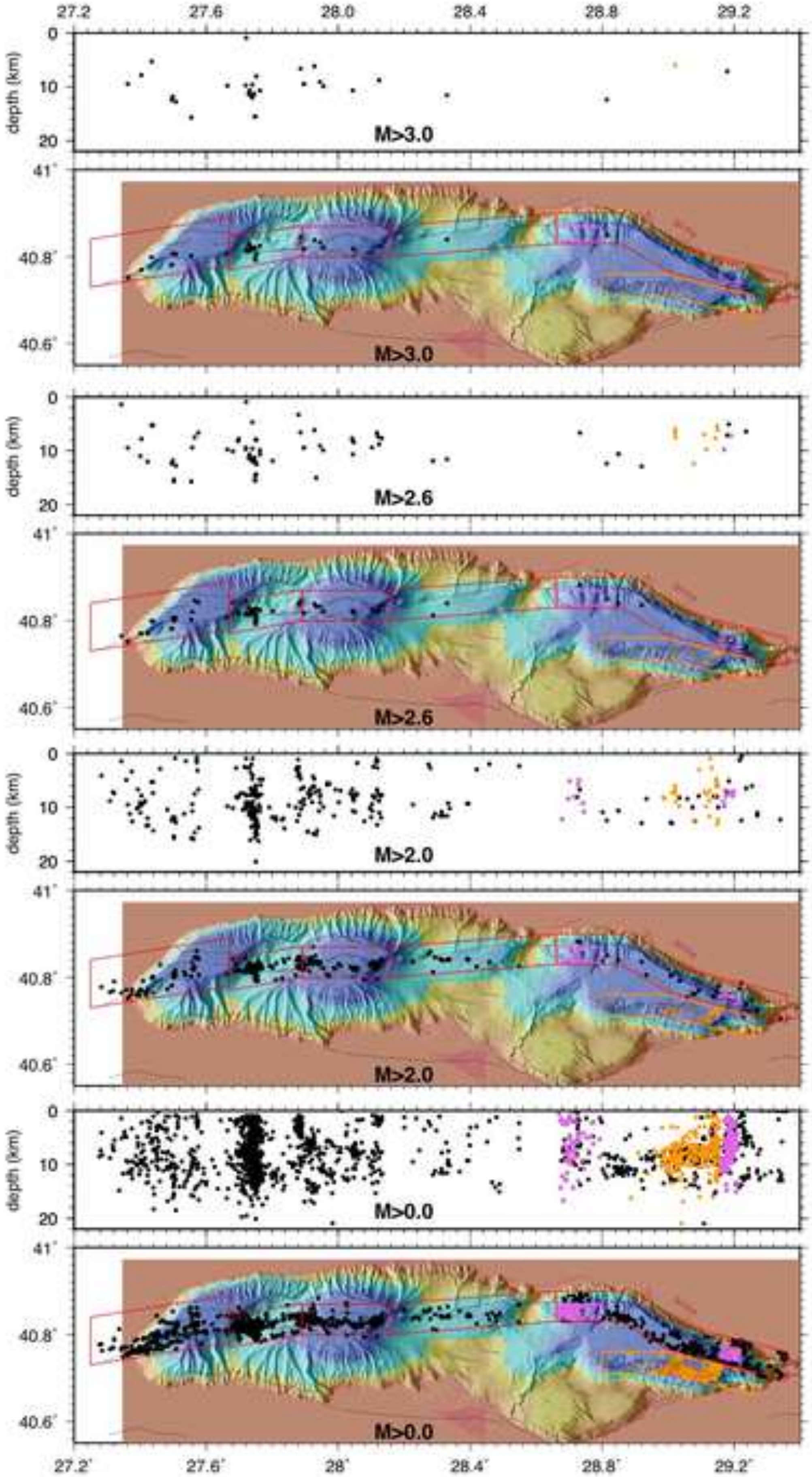

Supplementary information for «An alternative view of the micro-seismicity along the Western Main Marmara Fault»

Evangelia Batsi, Anthony Lomax, Jean-Baptiste Tary, Frauke Klingelhoefer, Vincent Riboulot, Shane Murphy, Stephen Monna, Nurcan Meral Özel, Dogan Kalafat, Hakan Saritas, Günay Cifçi, Namik Çagatay, Luca Gasperini, Louis Géli

This electronic supplement contains: (i) Earthquake Catalogs of relative locations, including the station correction values and the time delays obtained by the 1D and 3D velocity models of this study; (ii) Characteristics of the calculated composite focal mechanisms and (iii) Seismograms of the triplet of case study 2, recorded on the vertical and horizontal components of different OBS stations.

Catalogs of relocated events (Tables S1 to S4)

Station correction values for P and S phases (Tables S5 to S8)

Station corrections were applied by considering all the detected earthquakes of 2011 and 2014 as described (Lomax *et al.*, 2008). Events that were not meeting the criteria of well-constrained earthquakes were eliminated from our catalogue (see paragraph on: Location procedure).

Comparison of 1D vs 3D time delays for selected events (Figure S1 and Table S9)

Characteristics of Focal Mechanisms (Figures S2 to S5 and Table S10)

Case Study 1: composite focal mechanism derived from the 3D-locations (Figure S2)

Case study 2: composite focal mechanism derived from the 3D-locations (Figure S3)

Case study 3: composite focal mechanism derived from the 3D-locations (Figure S4)

Composite focal mechanism computed for 10 events triggered by the

M 5.1 earthquake of the 25th of July, 2011 (Figure S5 and Table S10).

Seismograms of the triplet of case study 2 (Figures S6 to S9).

List of Table Captions

Table S1: Catalogue of relocated events (Step 5: see main text) with statistics obtained with the NLDiffLoc, using the 1D velocity model of this study (2011 data set).

Table S2: Catalogue of relocated events (Step 5: see main text) with statistics obtained with the NLDiffLoc, using the 3D velocity model of this study after applying station corrections (2011 data set).

Table S3: Catalogue of relocated events (Step 5: see main text) with statistics obtained with the NLDiffLoc, using the 1D velocity model of this study (2014 data set).

Table S4: Catalogue of relocated events (Step 5: see main text) with statistics obtained with the NLDiffLoc, using the 3D velocity model of this study after applying station corrections (2014 data set).

Table S5: Station correction values for P and S phases for the 1D-velocity model of this study for the 2011 data-set 1.

Table S6: Station correction values for P and S phases for the 3D-velocity model of this study for the 2011 data-set 1.

Table S7: Station correction values for P and S phases for the 1D-velocity model of this study for the 2014 data-set 2.

Table S8: Station correction values for P and S phases for the 3D-velocity model of this study for the 2014 data-set 2.

Table S9: List of selected events detected by all 10 OBSs (2011 dataset), displayed in Figure S1.

Table S10: Table of the 10 events triggered by the M 5.1 earthquake of the 25th of July, 2011 used for calculating the composite focal mechanism of Figure S5.

List of Figures Captions

Figure S1: P-wave travel-time residuals (observed-predicted) in seconds at 10 OBS (of 2011) for 1D (blue) and 3D (red) locations of 10 selected events (see Table S9).

Figure S2: Composite focal mechanism of case study 1, computed with HASH software (Hardebeck and Shearer, 2008), with the measured polarities represented with red and black circles, down and up motions respectively, calculated with the 3D velocity model of this study. Resulting focal mechanism: Strike/Dip/rake=190°/59°/-80°.

Figure S3: Composite focal mechanism of case study 2, computed with HASH software (Hardebeck and Shearer, 2008), with the measured polarities represented with red and black circles, down and up motions respectively, calculated with the 3D velocity model of this study. Resulting focal mechanism: Strike/Dip/rake=233°/67°/101°.

Figure S4: Composite focal mechanism of case study 3, computed with HASH software (Hardebeck and Shearer, 2008), with the measured polarities represented with red and black circles, down and up motions respectively, calculated with the 3D velocity model of this study. Resulting focal mechanism: Strike/Dip/rake=78°/58°/151°.

Figure S5: Composite focal mechanism computed for 10 events triggered by the M 5.1 earthquake of the 25th of July, 2011 (see Table S10). Computation with HASH software (Hardebeck and Shearer, 2008), with the measured polarities represented with red and black circles, down and up motions respectively, calculated with the 3D velocity model of this study. Resulting focal mechanism: Strike/Dip/rake=300°/34°/-145°.

Figure S6: Seismograms of the triplet of case study 2, recorded on the vertical and horizontal components of OBS07.

Figure S7: Seismograms of the triplet of case study 2, recorded on the vertical and horizontal components of OBS08.

Figure S8: Seismograms of the triplet of case study 2, recorded on the vertical and horizontal components of OBS09.

Figure S9: Seismograms of the triplet of case study 2, recorded on the vertical and horizontal components of OBS10.

References

Hardebeck, J.L. and Shearer, P.M., (2008). HASH : A Fortran program for computing Earthquake First-Motion Focal Mechanisms -v1.2 – January 31.

Lomax, A. (2008), Location and Tectonics of the Focal Region of the California Earthquake of 18 April 1906, Bull. Seism. Soc. Am., 98, 846-860.

Table S1. Catalogue of relocated events (Step 5: see main text) with statistics obtained with the NLDiffLoc, using the 1D velocity model of this study (2011 data set).

No	yy	mo	dd	hh	mm	ss	Lat (°)	Long (°)	Depth (km)	Ml	Exx (km)	Eyy (km)	Ezz (km)	RMS (s)	Nph	Gap (°)
1	2011	4	16	16	30	25	40.7995	28.0017	15.47	0.9	0.165	0.16	0.368	0.039	90	119
2	2011	4	20	5	4	49	40.8091	28.0051	14.82	0.6	0.08	0.075	0.155	0.046	127	107
3	2011	4	26	16	12	10	40.7998	27.9829	12.09	1	0.047	0.046	0.126	0.028	141	93
4	2011	4	29	4	58	40	40.7990	27.9446	3.74	0.8	0.049	0.056	0.081	0.076	130	78
5	2011	4	30	15	21	53	40.8112	27.9600	15.89	1.1	0.05	0.07	0.154	0.037	164	96
6	2011	5	1	8	36	17	40.8266	28.1355	13.69	3.3	0.057	0.064	0.093	0.027	187	115
7	2011	5	2	15	31	6	40.7147	28.1004	10.22	0.8	0.274	0.283	0.445	0.034	19	177
8	2011	5	4	5	3	19	40.8030	27.9136	19.28	0.7	0.143	0.326	0.771	0.072	97	78
9	2011	5	7	4	14	26	40.8042	27.9827	14.49	1.4	0.04	0.048	0.089	0.027	170	95
10	2011	5	7	17	27	50	40.8092	27.9763	14.05	2.2	0.036	0.049	0.097	0.029	182	97
11	2011	5	7	17	46	15	40.8021	27.9860	12.55	1.5	0.051	0.047	0.133	0.033	149	100
12	2011	5	9	14	0	3	40.7971	27.9895	12.6	0.9	0.046	0.05	0.134	0.035	140	98
13	2011	5	9	23	8	7	40.7946	27.9797	13.25	1.7	0.031	0.048	0.102	0.027	167	101
14	2011	5	12	14	32	44	40.7995	27.9797	13.49	1.7	0.034	0.045	0.088	0.028	176	93
15	2011	5	13	10	40	3	40.8020	27.9830	13.26	2	0.034	0.048	0.101	0.025	168	93
16	2011	5	14	15	23	24	40.7892	27.9927	8.74	0.5	0.048	0.055	0.112	0.058	124	103
17	2011	5	14	18	38	4	40.7927	27.9216	7.06	0.8	0.09	0.104	0.733	0.033	59	104
18	2011	5	15	3	39	1	40.8305	28.0294	18.48	1.1	0.273	0.209	0.372	0.076	45	111
19	2011	5	17	20	40	15	40.7999	27.9795	12.23	1.2	0.045	0.05	0.125	0.032	143	94
20	2011	5	18	3	17	0	40.8093	27.9796	13.76	1.8	0.033	0.042	0.089	0.029	180	104
21	2011	5	19	4	38	37	40.8251	28.1330	11.64	3.1	0.056	0.057	0.19	0.026	191	110
22	2011	5	19	4	44	7	40.8159	28.0985	2.71	1.1	0.061	0.045	0.129	0.075	168	95
23	2011	5	19	5	5	38	40.8377	28.0958	15.65	0.5	0.124	0.124	0.586	0.014	86	145
24	2011	5	22	22	39	26	40.8229	28.1370	11.12	2.3	0.067	0.061	0.198	0.024	174	106
25	2011	5	25	23	43	19	40.7918	27.9235	18.56	0.9	0.252	0.426	0.426	0.045	37	110
26	2011	5	29	7	24	20	40.8265	28.1468	13.62	1.1	0.066	0.076	0.106	0.022	170	108
27	2011	5	30	19	53	12	40.7872	27.9203	16.84	1.4	0.201	0.344	0.369	0.033	30	84
28	2011	6	9	20	43	27	40.8179	28.1227	10.65	1.8	0.039	0.043	0.123	0.021	185	96
29	2011	6	9	20	53	41	40.8194	28.1125	12.74	1.1	0.045	0.063	0.159	0.018	142	95
30	2011	6	10	3	54	24	40.8336	28.0822	15.22	0.6	0.12	0.13	0.281	0.023	65	135
31	2011	6	10	4	28	29	40.8202	28.1196	10.58	1.9	0.037	0.043	0.131	0.02	176	97
32	2011	6	10	5	52	19	40.7763	28.0507	4.94	1.4	0.127	0.147	0.115	0.139	61	109
33	2011	6	10	17	43	13	40.8205	28.1181	14.38	1.4	0.052	0.066	0.108	0.021	169	102
34	2011	6	12	6	9	29	40.8181	27.9563	18.93	0.9	0.081	0.105	0.29	0.044	168	101
35	2011	6	14	5	37	33	40.8229	28.1316	10.82	1.5	0.053	0.05	0.166	0.022	181	105
36	2011	6	23	20	25	11	40.8558	28.1189	19.64	0.9	0.181	0.324	0.87	0.018	71	137
37	2011	6	24	12	37	45	40.8439	27.9134	16.17	1.2	0.19	0.249	0.542	0.027	29	146
38	2011	6	24	12	58	48	40.8557	27.9150	19.48	1.7	0.192	0.292	0.807	0.014	22	152
39	2011	6	24	13	20	26	40.8369	27.9171	15.7	1	0.105	0.188	0.393	0.041	56	98
40	2011	7	2	3	30	53	40.8256	27.8485	12.45	1	0.198	0.298	0.894	0.021	19	143
41	2011	7	6	12	45	53	40.8254	27.9805	19.28	0.7	0.071	0.071	0.153	0.029	130	115
42	2011	7	7	9	42	35	40.8021	28.0094	22.49	0.7	0.093	0.075	0.387	0.033	109	95
43	2011	7	10	10	11	39	40.7531	28.1297	10.56	0.6	0.184	0.321	0.564	0.058	59	136
44	2011	7	14	9	15	41	40.7771	28.0119	18.43	1.6	0.124	0.103	0.335	0.036	100	118
45	2011	7	22	15	16	12	40.8062	28.0953	15.28	1.1	0.07	0.09	0.145	0.032	148	87
46	2011	7	23	5	14	59	40.8050	28.0950	12.68	1.5	0.087	0.102	0.475	0.029	126	91

Where: yy, mo, dd, hh, mm,ss, lat, lon stand for year, month, day, hour, minute, second, latitude, longitude
Exx, eyy, ezz, Nph for horizontal1, horizontal2, vertical location errors, respectively, and number of phases used

Table S2

Click here to download Supplemental Material (Main Page, Tables, Figures) TableS2.docx

Table S2. Catalogue of relocated events (Step 5: see main text) with statistics obtained with the NLDiffLoc, using the 3D velocity model of this study after applying station corrections (2011 data set).

No	year	month	day	hh	mm	ss	Lat	Long	Depth	Ml	Exx	Eyy	Ezz	RMS	Nphs	Gap
							(°)	(°)	(km)		(km)	(km)	(km)	(sec)		(°)
1	2011	4	16	16	30	26	40.8231	28.0082	14.99	0.9	0.061	0.091	0.146	0.051	103	120
2	2011	4	20	5	4	50	40.8293	28.0100	15.07	0.6	0.12	0.079	0.294	0.052	122	122
3	2011	4	26	16	12	10	40.8197	27.9867	11.89	1	0.163	0.081	0.307	0.035	132	118
4	2011	4	29	4	58	40	40.8220	27.9461	6.19	0.8	0.065	0.053	0.156	0.118	53	81
5	2011	4	30	15	21	54	40.8349	27.9641	16.26	1.1	0.166	0.134	0.166	0.055	165	131
6	2011	5	1	15	18	41	40.8656	28.1636	5.85	3.3	0.063	0.086	0.271	0.086	62	146
7	2011	5	2	15	31	6	40.7194	28.1148	11.96	0.8	0.359	0.505	0.747	0.075	11	130
8	2011	5	4	5	3	20	40.8330	27.9150	21.69	0.7	0.935	0.446	0.685	0.047	58	95
9	2011	5	7	4	14	26	40.8256	27.9889	14.77	1.4	0.14	0.195	0.541	0.034	157	125
10	2011	5	7	17	27	50	40.8299	27.9819	13.89	2.2	0.048	0.055	0.147	0.033	143	130
11	2011	5	7	17	46	16	40.8220	27.9903	12.36	1.5	0.054	0.066	0.202	0.035	138	122
12	2011	5	9	14	0	3	40.8173	27.9945	12.48	0.9	0.072	0.053	0.143	0.049	126	113
13	2011	5	9	23	8	8	40.8165	27.9851	13.37	1.7	0.103	0.066	0.216	0.031	143	113
14	2011	5	12	14	32	45	40.8207	27.9854	13.63	1.7	0.056	0.069	0.165	0.036	149	123
15	2011	5	13	10	40	3	40.8226	27.9890	13.19	2	0.052	0.056	0.149	0.035	157	122
16	2011	5	14	15	23	25	40.8150	27.9884	7.37	0.5	0.053	0.052	0.138	0.075	118	110
17	2011	5	14	18	38	4	40.8047	27.9225	6.21	0.8	0.111	0.173	0.392	0.024	19	105
18	2011	5	15	3	39	1	40.8505	28.0441	18.92	1.1	0.181	0.361	0.513	0.063	72	128
19	2011	5	17	20	40	15	40.8202	27.9837	12.08	1.2	0.284	0.173	0.463	0.041	136	115
20	2011	5	18	3	17	1	40.8294	27.9857	13.6	1.8	0.065	0.054	0.165	0.039	157	129
21	2011	5	19	4	38	37	40.8340	28.1442	4.33	3.1	0.054	0.062	0.16	0.048	117	130
22	2011	5	19	4	44	6	40.8277	28.1154	0	1.1	0.072	0.063	0.265	0.15	96	107
23	2011	5	19	5	5	38	40.8340	28.1246	1.46	0.5	0.145	0.099	0.072	0.017	63	120
24	2011	5	22	22	39	26	40.8330	28.1463	4.19	2.3	0.027	0.038	0.177	0.041	110	149
25	2011	5	25	23	43	20	40.8236	27.9208	19.68	0.9	0.17	0.08	0.477	0.039	40	125
26	2011	5	29	7	24	21	40.8396	28.1628	7.96	1.1	0.211	0.381	0.87	0.034	98	151
27	2011	5	30	19	53	12	40.8174	27.9206	18.33	1.4	0.187	0.126	0.469	0.051	52	70
28	2011	6	9	20	43	28	40.8312	28.1399	4.95	1.8	0.121	0.19	0.306	0.034	108	122
29	2011	6	9	20	53	41	40.8380	28.1421	10.75	1.1	0.096	0.054	0.411	0.028	89	119
30	2011	6	10	3	54	24	40.8599	28.1184	16.32	0.6	0.087	0.1	0.346	0.024	72	173
31	2011	6	10	4	28	30	40.8323	28.1381	5.03	1.9	0.123	0.169	0.344	0.036	108	125
32	2011	6	10	5	52	19	40.7961	28.0613	5.28	1.4	0.102	0.074	0.499	0.206	84	120
33	2011	6	10	17	43	13	40.8407	28.1496	11.99	1.4	0.204	0.15	0.19	0.034	91	167
34	2011	6	12	6	9	29	40.8436	27.9604	20.02	0.9	0.138	0.128	0.536	0.062	165	137
35	2011	6	14	5	37	33	40.8330	28.1436	4.18	1.5	0.078	0.12	0.258	0.042	110	143
36	2011	6	23	20	25	11	40.8361	28.1303	0.7	0.9	0.082	0.056	0.282	0.019	63	131
37	2011	6	24	12	37	45	40.8685	27.9132	15.47	1.2	0.027	0.034	0.091	0.033	25	167
38	2011	6	24	12	58	49	40.8855	27.9133	18.97	1.7	0.193	0.284	0.798	0.016	13	179
39	2011	6	24	13	20	26	40.8610	27.9173	14.68	1	0.373	0.553	1.12	0.02	39	160
40	2011	7	2	3	30	53	40.8521	27.8458	17.53	1	0.124	0.181	0.338	0.072	15	172
41	2011	7	6	12	45	53	40.8501	27.9888	19.94	0.7	0.494	0.537	0.521	0.044	127	145
42	2011	7	7	9	42	35	40.8297	28.0240	25.81	0.7	0.555	0.789	1.221	0.046	108	128
43	2011	7	10	10	11	40	40.7798	28.1440	5.57	0.6	0.202	0.103	0.46	0.088	79	127
44	2011	7	14	9	15	41	40.8060	28.0134	20.56	1.6	0.192	0.288	0.633	0.069	116	102
45	2011	7	22	15	16	13	40.8298	28.1305	15.2	1.1	0.206	0.182	0.831	0.053	111	135
46	2011	7	23	5	14	59	40.8250	28.1243	11.96	1.5	0.127	0.102	0.393	0.038	89	112

Where: yy, mo, dd, hh, mm,ss, lat, lon stand for year, month, day, hour, minute, second, latitude, longitude
Exx, eyy, ezz, Nph for horizontal1, horizontal2, vertical location errors, respectively, and number of phases used

Table S3. Catalogue of relocated events (Step 5: see main text) with statistics obtained with the NLDiffLoc, using the 1D velocity model of this study (2014 data set).

No	yy	mo	dd	hh	mm	ss	Lat (°)	Long (°)	Depth (km)	Ml	Exx (km)	Eyy (km)	Ezz (km)	RMS (s)	Nph	Gap (°)
1	2014	9	21	4	35	29	40.8279	27.8751	3.7	1.7				0.081	42	133
2	2014	9	23	4	15	39	40.8054	27.7898	10.0	1.8	0.091	0.063	0.148	0.044	147	86
3	2014	9	23	4	43	18	40.7996	27.7948	11.4	1.7	0.148	0.531	0.646	0.02	97	90
4	2014	9	23	5	6	21	40.8067	27.7975	9.5	2	0.07	0.038	0.086	0.015	124	68
5	2014	9	23	5	34	36	40.8055	27.7925	10.2	1.9	0.088	0.051	0.24	0.043	141	73
6	2014	9	25	6	54	60	40.8000	27.7356	7.9	1.7	0.129	0.151	0.477	0.026	39	167
7	2014	9	26	6	2	54	40.7888	27.7165	9.4	1.7	0.2	0.301	0.229	0.04	126	99
8	2014	9	27	8	50	14	40.8107	27.9007	3.3	1	0.212	0.22	0.515	0.05	21	174
9	2014	9	30	12	34	16	40.8169	27.7222	4.7	1.7	0.052	0.045	0.07	0.025	72	139
10	2014	10	1	14	44	50	40.8325	27.8917	3.9	1.3	0.152	0.208	0.277	0.074	31	152
11	2014	10	3	11	19	24	40.8628	27.8552	10.1	1.3	0.265	0.531	0.841	0.124	38	155
12	2014	10	3	21	40	19	40.7219	27.7818	25.4	1.7	0.297	0.401	0.625	0.111	90	132
13	2014	10	4	11	58	35	40.8360	27.7524	3.0	2.2	0.063	0.122	0.192	0.028	84	136
14	2014	10	4	17	31	45	40.8395	27.7928	4.5	1.8	0.16	0.314	0.715	0.022	62	175
15	2014	10	5	14	48	4	40.8130	27.7243	3.6	1.6	0.167	0.225	0.042	0.009	68	114
16	2014	10	6	11	4	57	40.8121	27.7676	6.5	1.7	0.672	0.408	0.391	0.002	63	125
17	2014	10	8	3	11	44	40.7878	27.6762	10.4	1.5	0.423	0.182	0.464	0.032	46	119
18	2014	10	11	6	42	58	40.7227	27.7705	10.7	2.3	0.183	0.429	0.766	0.059	49	178
19	2014	10	11	12	7	0	40.7394	27.8128	0.0	1.6	0.328	0.104	0.116	0.185	47	146
20	2014	10	12	4	58	26	40.8390	27.7662	3.5	1.7	0.07	0.054	0.125	0.047	125	140
21	2014	10	12	22	8	19	40.8349	27.7715	13.9	1.5	0.7	0.151	0.553	0.009	43	138
22	2014	10	17	8	44	29	40.7140	27.7370	5.1	1.5	0.185	0.332	0.349	0.054	40	174
23	2014	10	18	5	25	50	40.8329	27.7483	17.2	1	0.715	0.594	0.395	0.009	24	116
24	2014	10	18	10	17	42	40.8093	27.8204	13.1	1.9	0.137	0.08	0.322	0.034	70	151
25	2014	10	19	23	49	33	40.8230	27.7435	11.5	1.7	0.569	0.465	0.6	0.003	35	169
26	2014	10	20	3	48	37	40.8145	27.7890	6.9	1.5	0.054	0.08	0.116	0.038	132	81
27	2014	10	22	6	7	16	40.8151	27.8222	12.4	1.4	0.319	0.739	0.555	0.028	15	180
28	2014	10	22	17	11	35	40.7576	27.8581	5.1	2.4	1.083	0.199	0.629	0.053	54	154
29	2014	10	23	0	9	42	40.7515	27.6776	12.4	2.2	0.352	0.635	0.603	0.044	39	134
30	2014	10	23	16	29	40	40.7483	27.8410	4.2	1.8	0.807	0.536	0.735	0.105	36	176
31	2014	10	25	1	46	52	40.8080	27.8032	10.8	1.5	0.094	0.128	0.246	0.032	83	92
32	2014	10	25	3	5	1	40.8036	27.7999	9.6	1.9	0.096	0.07	0.147	0.038	136	112
33	2014	10	25	4	21	39	40.8035	27.8039	10.5	1.5	0.08	0.061	0.165	0.015	92	126
34	2014	10	25	15	9	6	40.8165	27.6666	19.4	1.7	0.398	1.081	0.403	0.017	12	128
35	2014	10	26	3	21	34	40.8042	27.7308	7.3	1.6	0.07	0.059	0.192	0.051	93	120
36	2014	10	26	7	41	51	40.8046	27.7344	15.5	2	0.175	0.148	0.657	0.006	56	134
37	2014	10	26	19	24	37	40.8066	27.8076	10.5	1.9	0.131	0.054	0.137	0.01	83	152
38	2014	10	27	21	22	10	40.7717	27.7855	0.0	1.6	0.024	0.026	0.237	0.027	90	93
39	2014	11	2	22	1	31	40.8868	27.6170	5.2	1.7	0.693	0.19	0.559	0.001	17	168
40	2014	11	5	5	56	5	40.7965	27.8383	5.1	1.4	0.221	0.138	0.641	0.025	77	140
41	2014	11	5	23	31	48	40.7292	27.9154	6.5	1.4	0.833	0.594	0.714	0.001	20	119
42	2014	11	7	0	38	38	40.8883	27.7666	14.3	1	0.294	0.257	0.684	0.024	45	130
43	2014	11	10	6	17	38	40.7930	27.8438	0.2	1.8	0.118	0.079	0.113	0.089	47	135
44	2014	11	13	4	26	15	40.8136	27.7386	4.9	1.5	0.081	0.053	0.129	0.037	93	71
45	2014	11	13	15	51	32	40.7787	27.7423	19.7	1.7	0.564	0.233	0.609	0.014	70	115

Where: yy, mo, dd, hh, mm,ss, lat, lon stand for year, month, day, hour, minute, second, latitude, longitude
Exx, eyy, ezz, Nph for horizontal1, horizontal2, vertical location errors, respectively, and number of phases used

Table S4. Catalogue of relocated events (Step 5: see main text) with statistics obtained with the NLDiffLoc, using the 3D velocity model of this study after applying station corrections (2014 data set).

No	yy	mo	dd	hh	mm	ss	Lat (°)	Long (°)	Depth (km)	Ml	Exx (km)	Eyy (km)	Ezz (km)	RMS (s)	Nph	Gap (°)
1	2014	9	21	4	35	28	40.8462	27.8754	4.16	1.7	0.046	0.064	0.067	0.05	57	156
2	2014	9	23	4	15	40	40.8439	27.7854	6.33	1.8	0.218	0.085	0.113	0.059	116	101
3	2014	9	23	4	43	18	40.8469	27.8022	5.22	1.7	1.178	0.842	0.584	0.094	68	153
4	2014	9	23	5	34	36	40.8405	27.7905	4.89	2	0.055	0.032	0.138	0.035	113	87
5	2014	9	25	6	54	60	40.8376	27.7507	8.01	1.9	0.074	0.061	0.133	0.02	104	154
6	2014	9	26	6	2	55	40.8309	27.7308	5.25	1.7	0.076	0.041	0.132	0.04	159	76
7	2014	9	27	8	50	14	40.8361	27.8948	4.71	1.7	0.052	0.062	0.134	0.048	56	149
8	2014	9	30	12	34	16	40.8397	27.7345	5.42	1	0.226	0.076	0.319	0.021	143	84
9	2014	10	1	14	44	49	40.8509	27.8905	3.55	1.7	0.043	0.141	0.136	0.057	53	154
10	2014	10	3	11	19	25	40.8514	27.8779	3.88	1.3	0.046	0.077	0.086	0.024	48	163
11	2014	10	3	21	40	22	40.8340	27.8769	5.59	1.3	0.054	0.057	0.116	0.016	50	140
12	2014	10	4	11	58	35	40.8243	27.7265	7	1.7	0.39	0.42	0.446	0.006	111	130
13	2014	10	4	17	31	44	40.8558	27.7948	4.83	2.2	0.187	0.139	0.686	0.004	71	151
14	2014	10	5	14	48	4	40.8150	27.7076	5.21	1.8	0.057	0.026	0.081	0.002	77	173
15	2014	10	6	11	4	58	40.8277	27.7455	3.83	1.6	0.68	0.683	0.582	0.011	53	174
16	2014	10	8	3	11	44	40.8216	27.7532	0.92	1.7	0.05	0.02	0.104	0.021	83	102
17	2014	10	11	6	42	59	40.7594	27.7838	11.43	1.5	0.445	0.316	0.809	0.083	28	161
18	2014	10	11	12	7	1	40.7538	27.7917	2.44	2.3	0.578	0.535	0.691	0.088	21	123
19	2014	10	12	4	45	29	40.8109	27.7050	13.52	1.6	0.241	0.075	0.439	0.046	93	169
20	2014	10	12	22	8	19	40.8669	27.7496	3.47	1.7	0.167	0.063	0.48	0.002	72	132
21	2014	10	17	8	44	30	40.7406	27.7486	7.91	1.5	0.222	0.236	0.464	0.028	25	143
22	2014	10	17	19	52	53	40.8295	27.8642	4.9	1.5	0.052	0.057	0.125	0.056	72	121
23	2014	10	18	5	25	52	40.8932	27.7166	2.87	1	0.626	0.4	0.548	0.005	57	146
24	2014	10	18	10	17	43	40.8471	27.8087	6.61	1.9	0.102	0.094	0.247	0.042	72	101
25	2014	10	19	23	49	32	40.8230	27.8027	2.27	1.7	0.176	0.435	0.564	0.005	63	163
26	2014	10	20	3	48	37	40.8462	27.7916	4.91	1.5	0.063	0.051	0.062	0.064	108	103
27	2014	10	22	6	7	16	40.8717	27.8299	3.61	1.4	0.432	0.124	1.165	0.047	31	168
28	2014	10	22	17	11	36	40.8101	27.8667	5.14	2.4	0.79	0.817	0.31	0.024	17	98
29	2014	10	23	0	9	43	40.8012	27.6865	15.73	2.2	0.565	0.928	1.305	0.048	9	180
30	2014	10	23	16	29	41	40.8430	27.6378	10.08	1.8	0.678	0.095	0.175	0.004	106	114
31	2014	10	25	1	46	53	40.8452	27.8120	6.21	1.5	0.154	0.044	0.131	0.02	73	166
32	2014	10	25	3	5	1	40.8484	27.8104	6.29	1.9	0.132	0.094	0.107	0.027	88	168
33	2014	10	25	4	21	39	40.8421	27.8096	6.59	1.5	0.136	0.045	0.095	0.02	75	175
34	2014	10	25	15	9	8	40.7394	27.6703	5.68	1.7	0.46	1.457	1.625	0.12	10	125
35	2014	10	26	3	21	34	40.8303	27.7331	5.19	1.6	0.034	0.021	0.034	0.02	125	113
36	2014	10	26	7	41	52	40.8463	27.7379	6.68	2	0.229	0.656	0.248	0.034	91	108
37	2014	10	26	19	24	37	40.8446	27.7972	6.7	1.9	0.069	0.054	0.173	0.013	105	149
38	2014	10	27	21	20	29	40.8263	27.7068	18.68	1.6	0.537	0.362	1.326	0.002	92	162
39	2014	11	2	22	1	31	40.8702	27.6634	14.65	1.7	1.539	0.716	0.702	0.001	53	156
40	2014	11	5	5	56	4	40.8378	27.8186	0.53	1.4	0.076	0.065	0.176	0.027	84	163
41	2014	11	5	23	31	50	40.7643	27.8128	11.69	1.4	0.885	0.578	0.981	0.004	9	112
42	2014	11	7	0	38	39	40.8938	27.7604	6.31	1	0.312	0.212	0.514	0.003	15	123
43	2014	11	10	6	17	38	40.7877	27.8170	1.31	1.8	0.632	0.623	0.31	0.014	14	130
44	2014	11	13	4	26	15	40.8366	27.7449	4.68	1.5	0.079	0.026	0.086	0.027	109	98
45	2014	11	13	15	51	33	40.8343	27.7871	5.23	1.7	0.188	0.101	0.89	0.015	78	134

Where: yy, mo, dd, hh, mm,ss, lat, lon stand for year, month, day, hour, minute, second, latitude, longitude
Exx, eyy, ezz, Nph for horizontal1, horizontal2, vertical location errors, respectively, and number of phases used

Table S5: Station correction values for P and S phases for the 1D-velocity model of this study for the 2011 data-set 1.

ID	Phase	Nres	AveRes	StdDev	ResMin	ResMax
OBS1	P	40	0.02	0.16	-0.21	0.60
OBS1	S	10	4.59	8.95	-0.09	22.89
OBS2	P	37	-0.03	0.17	-0.31	0.54
OBS2	S	6	0.28	0.31	-0.19	0.68
OBS3	P	36	0.10	0.09	-0.07	0.29
OBS3	S	17	1.04	4.63	-0.40	19.57
OBS4	P	29	0.54	3.38	-6.08	3.67
OBS4	S	9	-2.29	1.88	-5.55	-0.68
OBS5	P	59	0.05	0.11	-0.16	0.45
OBS5	S	31	0.16	0.27	-0.38	0.95
OBS6	P	53	-0.16	0.61	-1.11	1.54
OBS6	S	14	1.66	5.56	-1.59	21.57
OBS7	P	60	-0.08	0.15	-0.39	0.56
OBS7	S	33	0.40	0.32	-0.21	1.37
OBS8	P	59	-0.09	0.15	-0.42	0.58
OBS8	S	21	-0.01	0.20	-0.40	0.42
OBS9	P	58	-0.22	2.03	-15.51	0.59
OBS9	S	38	-0.19	0.21	-0.85	0.30
OBS10	P	48	0.32	0.27	-0.02	0.81
OBS10	S	/	/	/	/	/

Where: Nres, AveRes, StdDev, ResMin, ResMax stand for: Number of Residuals, Average Residual, Standard Deviation, Minimum Residual and Maximum Residual respectively.

Table S6: Station correction values for P and S phases for the 3D-velocity model of this study for the 2011 data-set 1.

ID	Phase	Nres	AveRes	StdDev	ResMin	ResMax
OBS1	P	31	-0.06	0.18	-0.38	0.57
OBS1	S	6	0.90	0.49	0.42	1.95
OBS2	P	27	-0.04	0.23	-0.36	0.73
OBS2	S	4	-0.27	0.23	-0.46	0.12
OBS3	P	27	0.09	0.10	-0.25	0.33
OBS3	S	14	0.18	0.13	-0.05	0.46
OBS5	P	41	0.01	0.26	-0.50	1.23
OBS5	S	24	0.20	0.24	-0.32	0.64
OBS6	P	40	-0.05	0.69	-1.24	1.76
OBS6	S	10	0.30	1.04	-0.49	3.35
OBS7	P	42	-0.02	0.18	-0.62	0.71
OBS7	S	21	0.04	0.25	-0.72	0.38
OBS8	P	41	0.00	0.23	-0.60	1.00
OBS8	S	13	0.88	2.14	0.00	8.28
OBS9	P	40	-0.34	2.32	-14.78	0.49
OBS9	S	27	0.30	0.33	-0.47	1.32
OBS10	P	31	0.03	0.05	-0.14	0.16
OBS10	S	/	/	/	/	/

Where: Nres, AveRes, StdDev, ResMin, ResMax stand for: Number of Residuals, Average Residual, Standard Deviation, Minimum Residual and Maximum Residual respectively.

Table S7: Station correction values for P and S phases for the 1D-velocity model of this study for the 2014 data-set 2.

ID	Phase	Nres	AveRes	StdDev	ResMin	ResMax
OBS1	P	39	-0.44	2.45	-14.03	1.86
OBS1	S	26	-1.66	1.30	-5.63	0.03
OBS3	P	34	-0.51	3.53	-20.47	2.57
OBS3	S	29	1.81	6.66	-4.53	26.96
OBS4	P	41	-0.24	0.59	-2.90	0.24
OBS4	S	37	0.90	1.12	-2.53	3.06
OBS5	P	39	-0.03	0.66	-1.26	3.55
OBS5	S	33	4.23	13.14	-1.30	64.11
OBS6	P	18	-0.36	0.87	-2.46	1.16
OBS6	S	14	4.61	7.39	0.06	22.20
OBS7	P	37	-0.69	2.81	-17.15	0.17
OBS7	S	33	1.60	4.60	-1.21	25.20
OBS8	P	46	0.06	0.58	-2.52	2.09
OBS8	S	40	0.88	3.89	-0.22	24.91
OBS9	P	4	1.69	1.20	0.24	3.32
OBS9	S	2	0.86	0.94	-0.07	1.80
OBS10	P	29	-0.27	0.77	-4.11	0.16
OBS10	S	19	1.87	3.55	-0.14	12.47

Where: Nres, AveRes, StdDev, ResMin, ResMax stand for: Number of Residuals, Average Residual, Standard Deviation, Minimum Residual and Maximum Residual respectively.

Table S8: Station correction values for P and S phases for the 3D-velocity model of this study for the 2014 data-set 2.

ID	Phase	Nres	AveRes	StdDev	ResMin	ResMax
OBS1	P	41	-1.29	5.35	-30.96	0.65
OBS1	S	29	0.11	0.61	-1.09	2.77
OBS3	P	36	-0.73	4.49	-19.79	5.05
OBS3	S	31	2.77	9.78	-9.96	43.92
OBS4	P	46	-0.61	2.12	-14.33	0.07
OBS4	S	40	0.80	1.04	-0.16	5.08
OBS5	P	34	-2.66	15.16	-89.64	2.84
OBS5	S	31	4.09	13.50	-2.30	63.67
OBS6	P	24	-1.71	5.92	-29.61	0.36
OBS6	S	19	3.10	6.13	-1.36	22.09
OBS7	P	43	-0.27	2.60	-16.68	1.85
OBS7	S	39	0.90	4.38	-6.60	25.08
OBS8	P	48	-0.23	0.60	-3.61	0.35
OBS8	S	38	1.34	4.59	-4.80	27.87
OBS9	P	4	0.65	0.72	-0.07	1.56
OBS9	S	3	2.51	1.99	-0.09	4.75
OBS10	P	29	-0.40	1.02	-5.20	0.20
OBS10	S	21	2.68	3.95	-0.36	14.55

Table S9: List of selected events detected by all 10 OBSs (2011 dataset), displayed in FigureS1.

N°	year	month	day	hh	mm	ss	Lat (°) (3D absolute location)	Long (°) (3D absolute location)	Depth (km) (3D absolute location)	Average RMS-1D (s)	Average RMS-3D (s)
1	2011	5	7	4	14	26	40.8291	27.9908	12.9	0.18	0.08
2	2011	5	7	17	27	50	40.8332	27.9835	12.3	0.22	0.10
3	2011	5	9	23	8	8	40.8187	27.9872	11.2	0.26	0.08
4	2011	5	12	14	32	44	40.8263	27.9889	12.3	0.23	0.11
5	2011	5	13	10	40	3	40.8256	27.992	10.9	0.19	0.09
6	2011	5	18	3	17	1	40.8338	27.9905	12.3	0.22	0.10
7	2011	5	19	4	38	36	40.834	28.136	2.2	0.24	0.18
8	2011	5	19	20	0	34	40.8198	28.1902	13.5	0.27	0.14
9	2011	6	9	20	43	27	40.8296	28.1321	2.4	0.20	0.20
10	2011	6	12	6	9	29	40.8371	27.9656	20.7	0.20	0.21

Where hh, mm,ss stand for hour, minute, second

Table S10: Table of the 10 events triggered by the M 5.1 earthquake of the 25th of July, 2011 used for calculating the composite focal mechanism of Figure S5.

No	yy	mo	dd	mm	ss	Lat	Long	Depth
						(°)	(°)	(km)
1	2011	7	25	18	37	40.818558	27.768202	2.13
2	2011	7	25	20	27	40.816772	27.763325	0.98
3	2011	7	26	5	36	40.818748	27.738325	5.77
4	2011	7	26	10	47	40.817307	27.752171	0.4
5	2011	7	26	16	18	40.815395	27.746065	0.93
6	2011	7	27	8	20	40.819805	27.774345	0.2
7	2011	7	27	10	21	40.819927	27.747383	5
8	2011	7	28	11	34	40.819996	27.764313	1
9	2011	7	30	3	41	40.822121	27.758406	1.46
10	2011	7	30	10	31	40.815159	27.748770	2.25

Where: yy, mo, dd, hh, mm,ss, lat, lon stand for year, month, day, hour, minute, second, latitude, longitude

Figure S1

Click here to download Supplemental Material (Main Page, Tables, Figures) FigureS1.jpeg

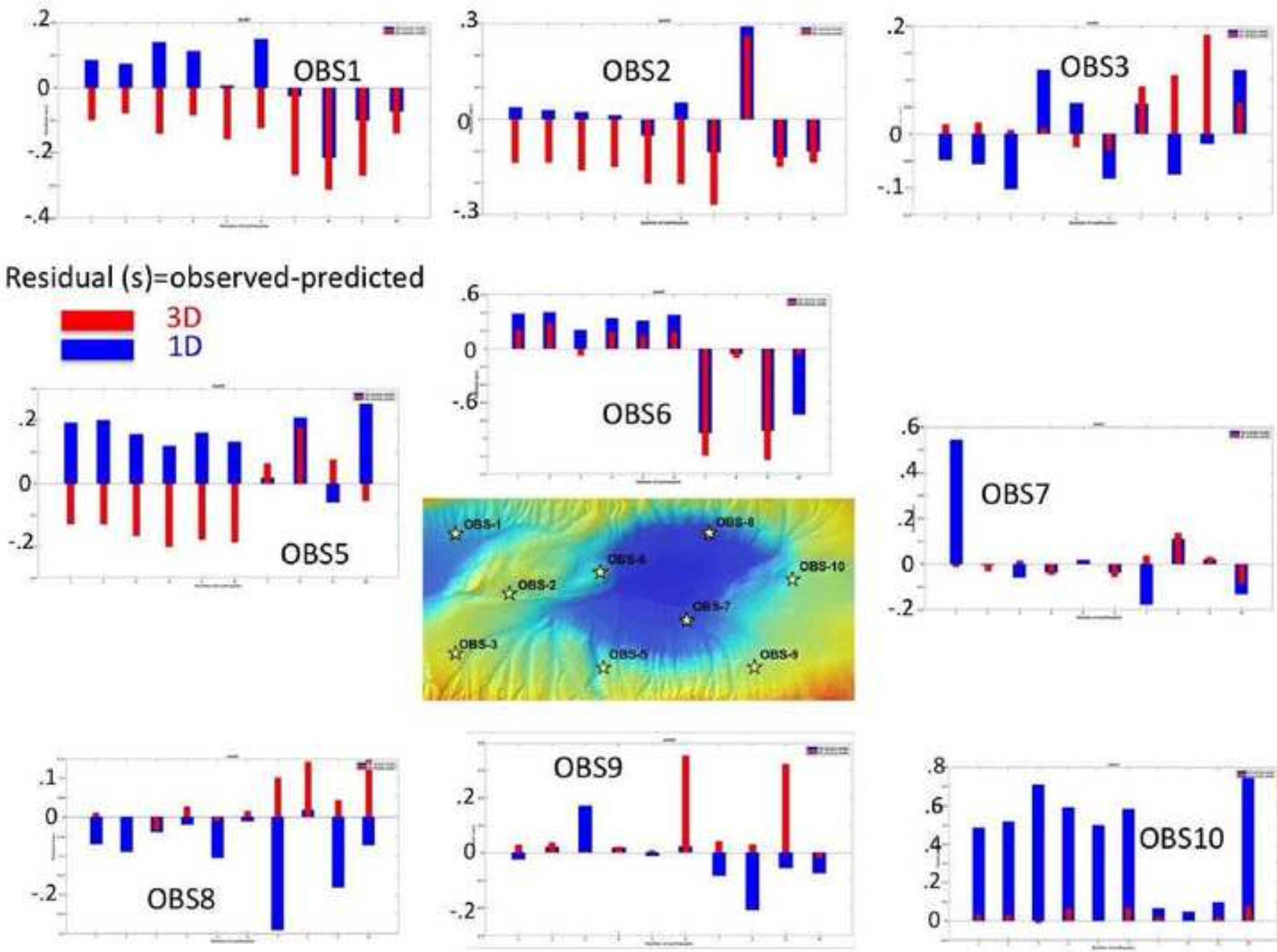

Figure S2

Click here to download Supplemental Material (Main Page, Tables, Figures) FigureS2.jpeg

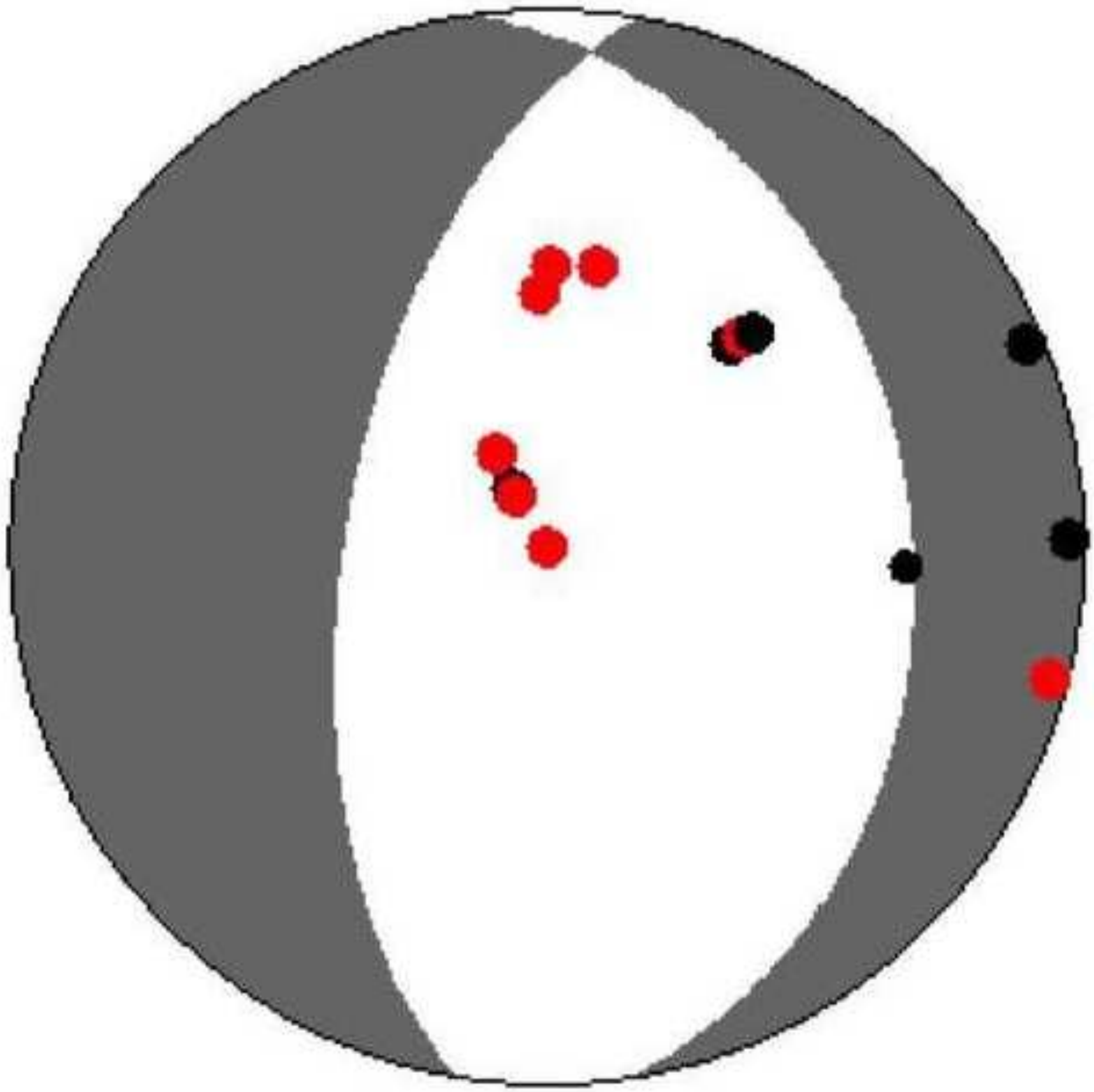

Figure S3

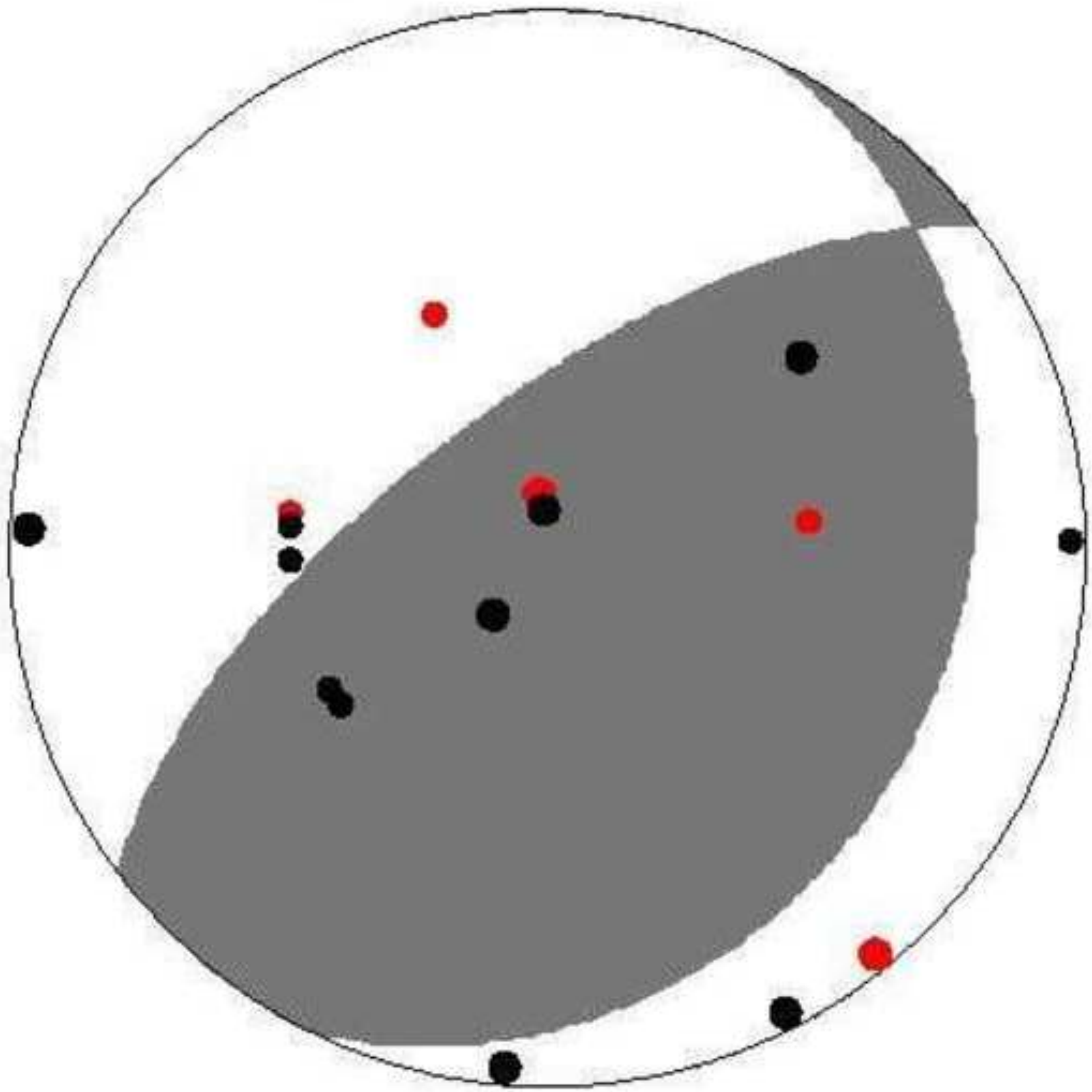

Figure S4

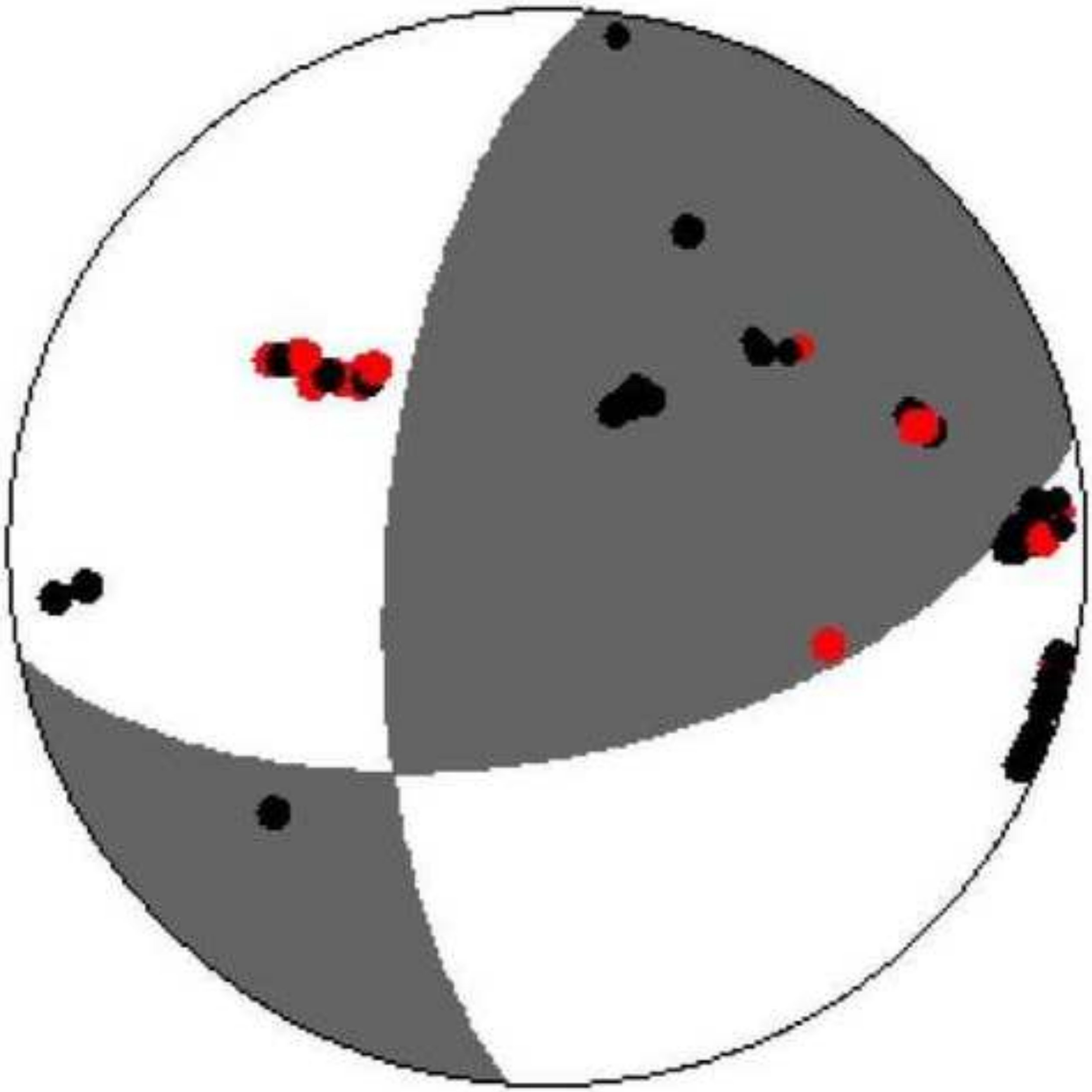

Fiigure S5

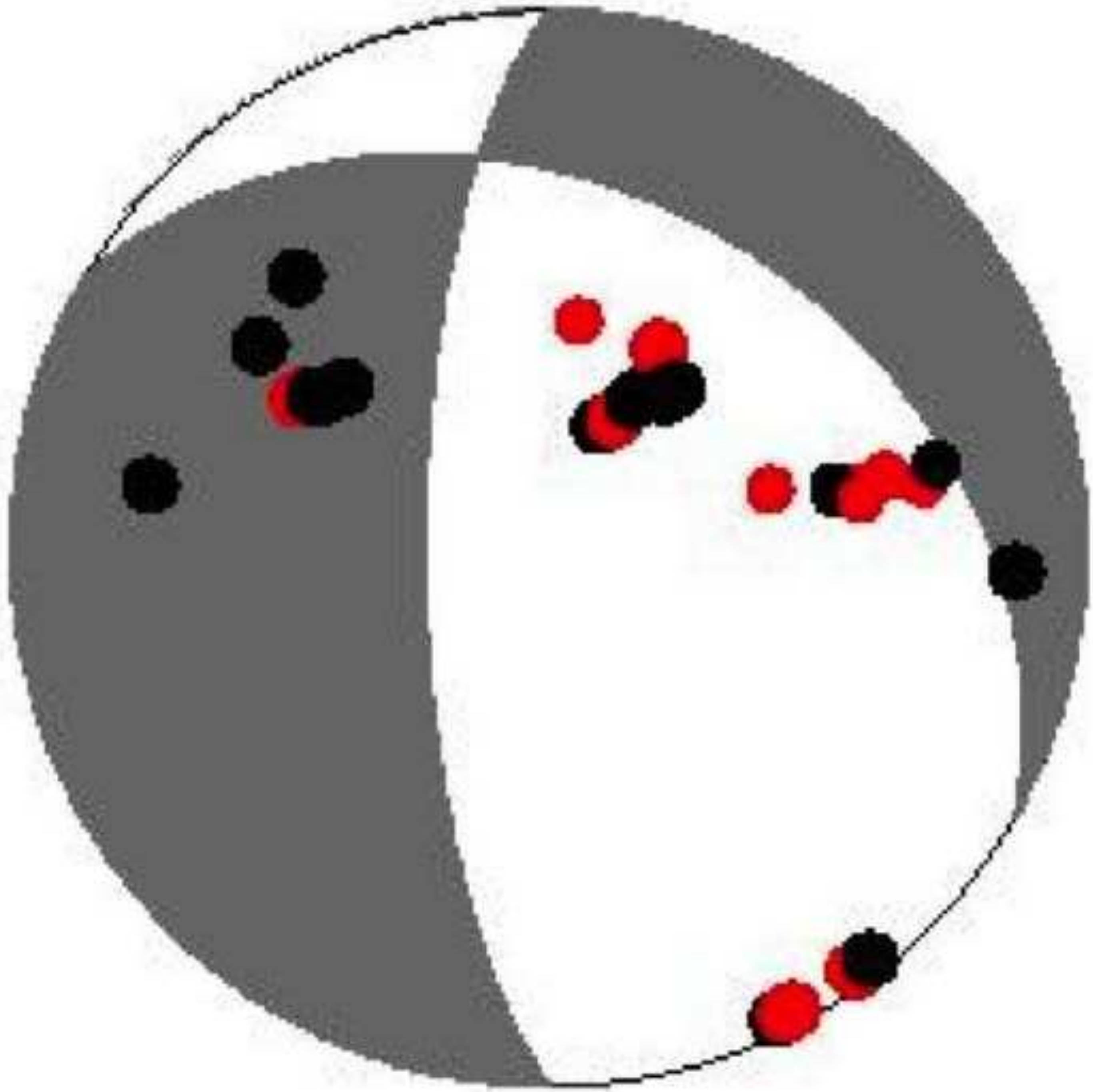

Figure S6

Click here to download Supplemental Material (Main Page, Tables, Figures) FigureS6.jpeg

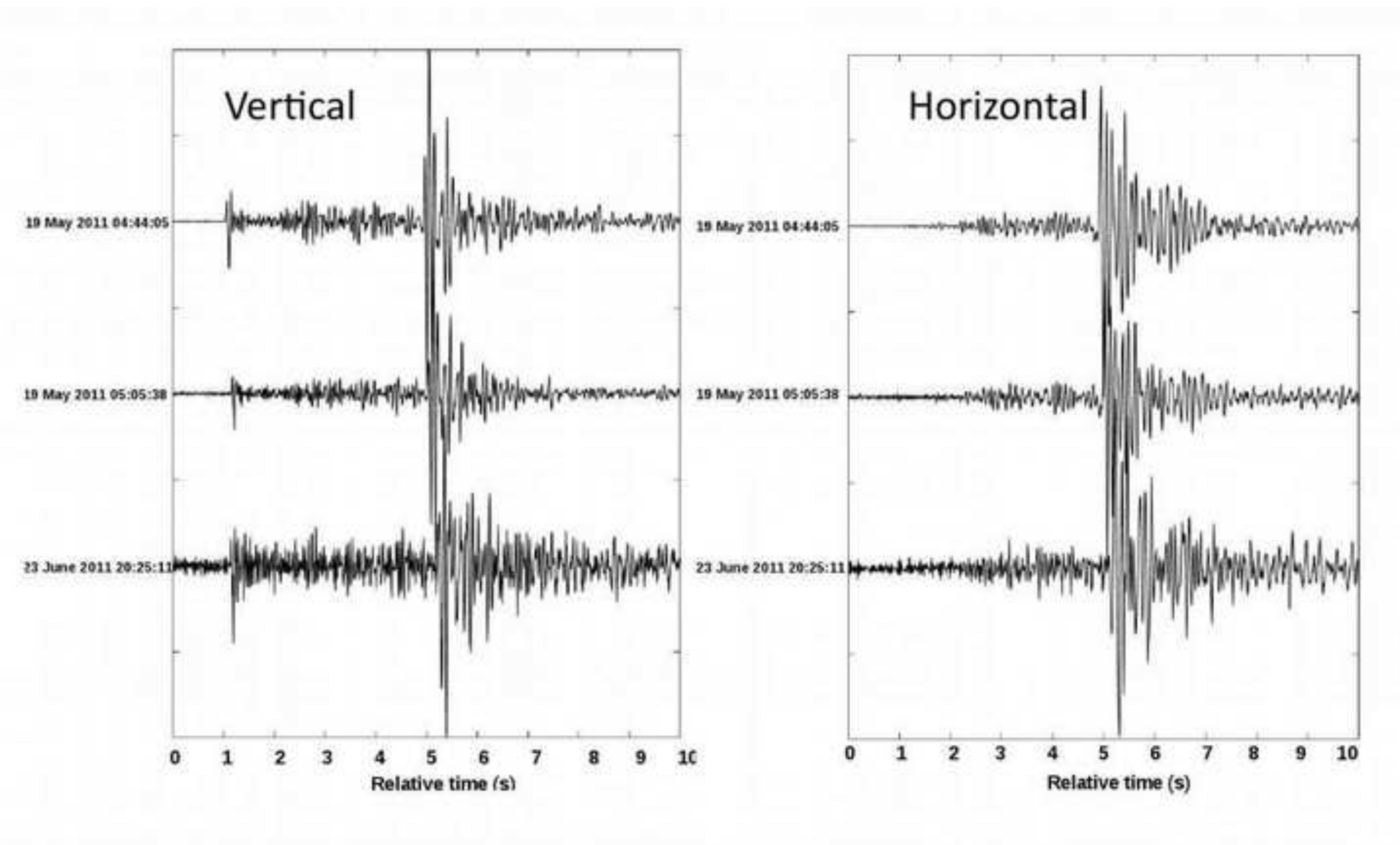

Figure S7

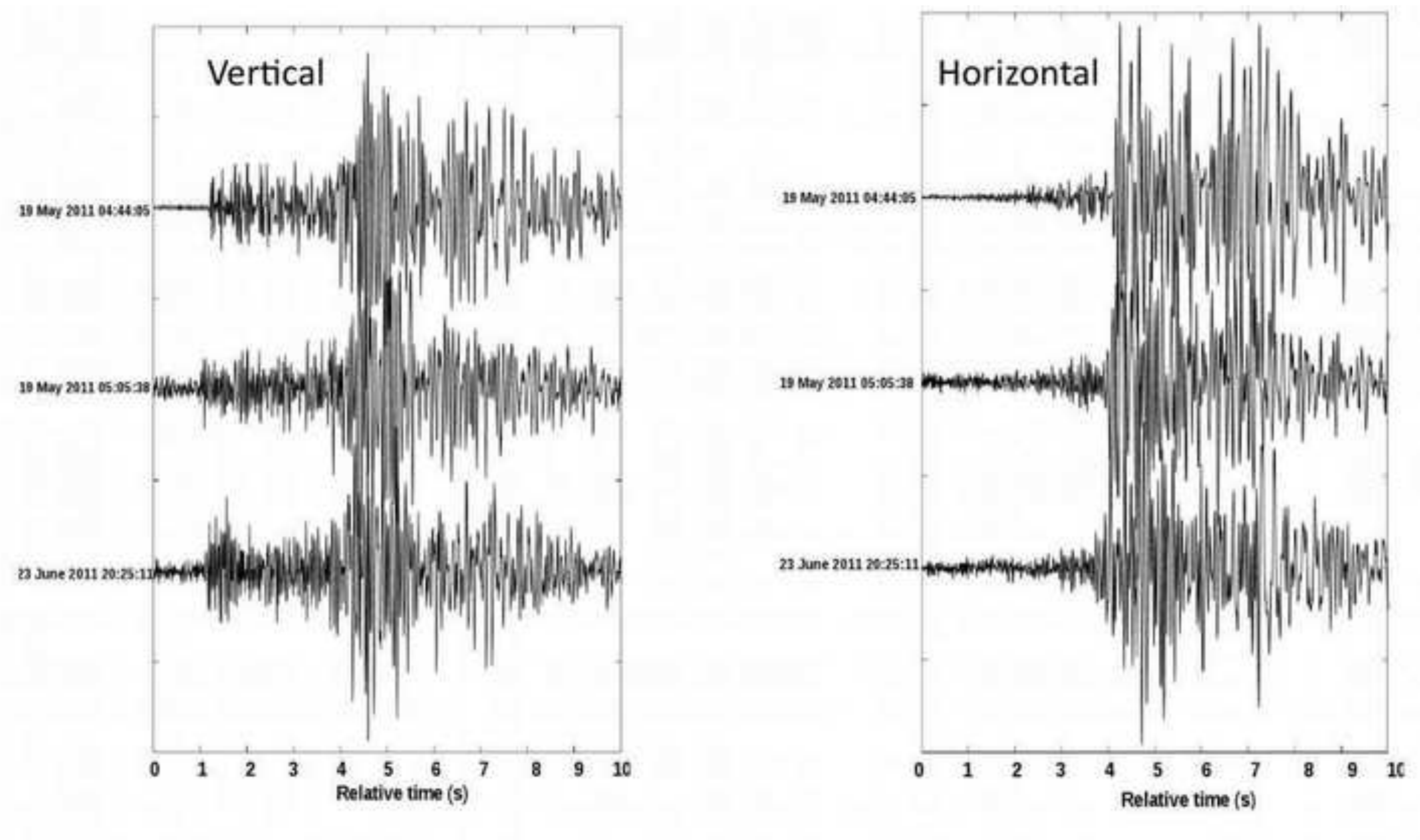
Vertical
19 May 2011 04:44:05
19 May 2011 05:05:38
23 June 2011 20:25:11
0
1
2
3
4
5
6
7
8
9
10
Relative time (s)
Horizontal
19 May 2011 04:44:05
19 May 2011 05:05:38
23 June 2011 20:25:11
0
1
2
3
4
5
6
7
8
9
10
Relative time (s)

Figure S8

Click here to download Supplemental Material (Main Page, Tables, Figures) FigureS8.jpeg

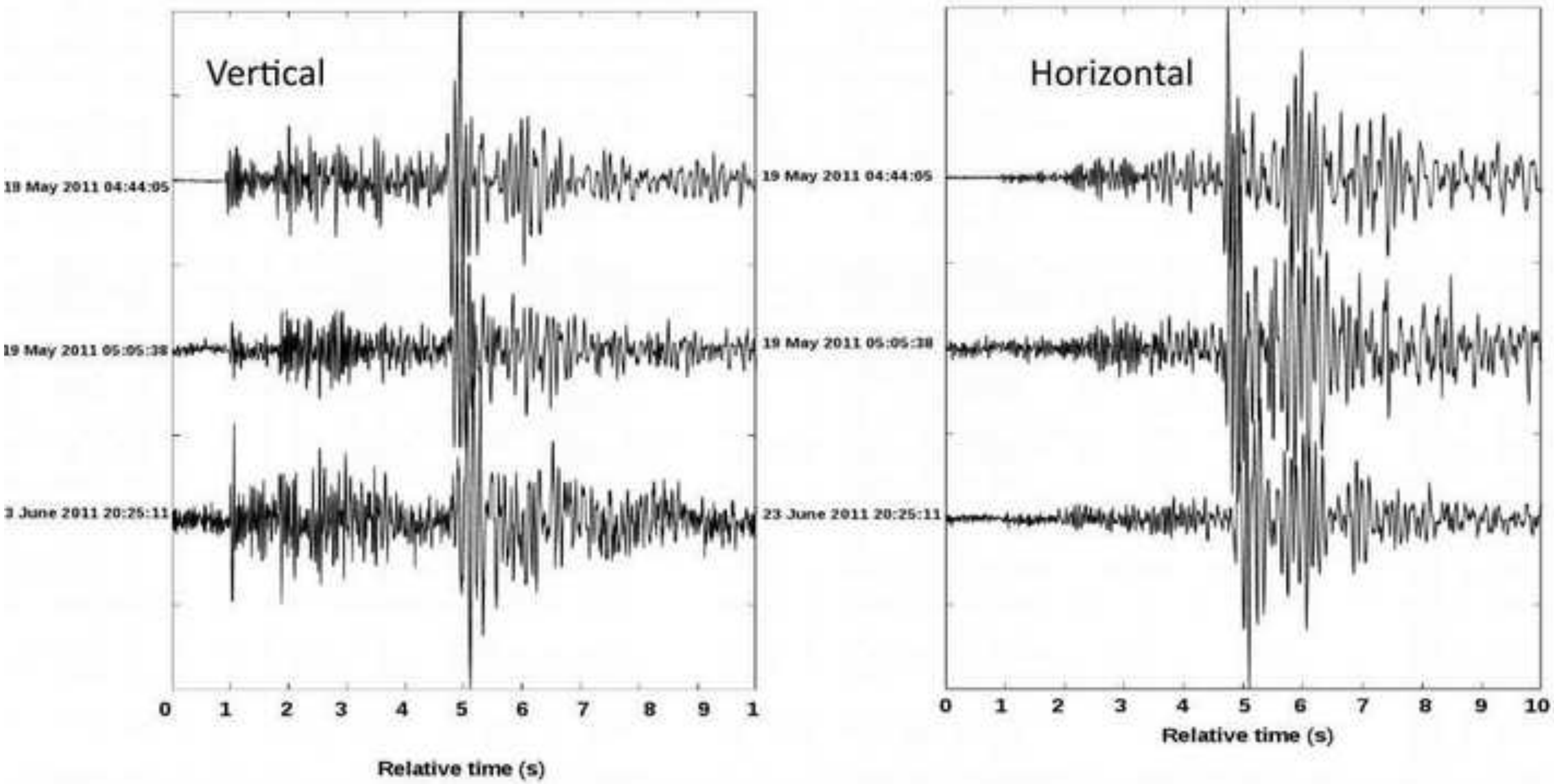

Figure S9

Click here to download Supplemental Material (Main Page, Tables, Figures) FigureS9.jpeg